General Disclaimer

One or more of the Following Statements may affect this Document

- This document has been reproduced from the best copy furnished by the organizational source. It is being released in the interest of making available as much information as possible.

- This document may contain data, which exceeds the sheet parameters. It was furnished in this condition by the organizational source and is the best copy available.

- This document may contain tone-on-tone or color graphs, charts and/or pictures, which have been reproduced in black and white.

- This document is paginated as submitted by the original source.

- Portions of this document are not fully legible due to the historical nature of some of the material. However, it is the best reproduction available from the original submission.

NASA CONTRACTOR REPORT

NASA CR-141428

INVESTIGATION OF THE APPLICATIONS OF GEOS-3 RADAR ALTIMETER DATA IN REMOTE SENSING OF LAND AND SEA FEATURES

Lee S. Miller

Prepared Under Contract No. NAS6-2520 by

Applied Science Associates, Inc.
105 East Chatham Street
Apex, North Carolina 27502

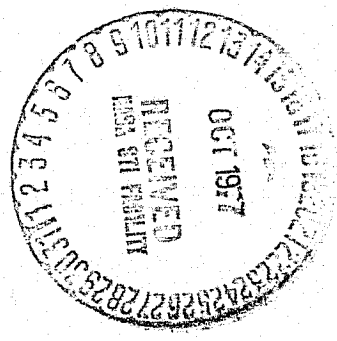

National Aeronautics and Space Administration

Wallops Flight Center
Wallops Island, Virginia 23337
AC 804 824-3411

August 1977

1. Report No.	2. Government Accession No.	3. Recipient's Catalog No.
NASA CR-141428		

4. Title and Subtitle	5. Report Date
Investigation of the Applications of GEOS-3 Radar Altimeter Data in Remote Sensing of Land and Sea Features	August 1977
	6. Performing Organization Code

7. Author(s)	8. Performing Organization Report No.
Lee S. Miller	
	10. Work Unit No.

9. Performing Organization Name and Address	11. Contract or Grant No.
Applied Science Associates, Inc. 105 E. Chatham Street Apex, North Carolina 27502	NAS6-2520
	13. Type of Report and Period Covered
12. Sponsoring Agency Name and Address	Contractor Report
National Aeronautics and Space Administration Wallops Flight Center Wallops Island, Virginia 23337	14. Sponsoring Agency Code

15. Supplementary Notes

16. Abstract

A number of GEOS-3 passes over the Atlantic Ocean and Southeastern U.S. are examined. Surface-truth and radar altimeter data comparisons are given in terms of surface correlation length, signal fluctuation characteristics, and altitude tracker dynamic response. Detailed analyses are given regarding spatial resolution and its dependency on angular backscatter behavior. These analyses include data from passes over ocean (diffuse scatter), land (large body scatter), and mirror-like inland water areas (pseudo-specular scatter). Altimeter data are examined for a pass over a large reservoir and marsh area of differing water levels; this geometry represents a stepchange in altitude which is usable in determination of the transient response of the tracker. The extent to which pulse-length limited operation pertains over-land is examined. A Wiener Filter altitude algorithm is discussed which permits specification of tracker variance and geoidal spectral characteristics during operation.

17. Key Words (Suggested by Author(s))	18. Distribution Statement
GEOS-3; radar altimeter; surface-truth; scatter	Unclassified - unlimited STAR category 43

19. Security Classif. (of this report)	20. Security Classif. (of this page)	21. No. of Pages	22. Price*
Unclassified	Unclassified	93	

*For sale by the National Technical Information Service, Springfield, Virginia 22151

TABLE OF CONTENTS

1.0 INTRODUCTION AND SUMMARY OF RESULTS

This report addresses the potential of remote sensing radar altimeter techniques to profile land and ocean areas of the earth with emphasis on the former category. These sensor capabilities relate to (1) the measurement of time variations in the land regions due to natural forces such as earthquake zones and surface dilatancy and those due to man's intervention in coal and other mineral mining regions, (2) seasonal and longterm variations in ocean circulation patterns such as the Gulf Stream, (3) snyoptic surveys of land topography of developed regions as a means of acquiring accurate statistical extractors such as terrain clearance in air traffic control terminal areas and surveys of less developed regions to define drainage areas, errors in existing surveys, promontory data, and potential mineral deposition, (4) automated recognition of high erosion areas and detection of the potential impacts of covert acts of commercial or military nature and (5) an independent method for the identification of over-land gravity anomalies.

The data analysis and quality assessment techniques to be discussed herein represent results of the first operational sensor discussed in the open literature and the critical examination of error sources is intended to provide a basis for the definition of the capabilities and technical benefits of future sensor systems. The GEOS-3 satellite program to be discussed represents an outgrowth of a sensor concept formulated in 1966 by the ad hoc Scientific Advisory Group to the NASA Geodetic Satellite Office* [1]; as such the solid earth measurement capability discussed here represents spin-off rather than state-of-the-art capability. As a result of these findings it

---

*This office was headed by J. D. Rosenberg of NASA/HQ. The present GEOS-3 Program is under the guidance of H. R. Stanley of NASA/WFC.

is now possible to define an electromagnetic sensor which is capable of profiling solid earth features to a selectable spatial and altimetric resolution, with due recognition of the cost trade offs of resolution versus sensor data rate, and processing/archival costs of the projected program. Especially noteworthy is the power of mean-sea-level regression techniques to provide precise topographic signatures without the need for centimeter-level absolute orbit determination. As SEA SAT-A will demonstrate, for the foreseeable future this level of orbital accuracy is a goal rather than an existing capability.

The specific capabilities and objectives examined in this report are as follows:

- GEOS-3 is shown to be capable of densely and economically profiling salient terrain features to an rms height error of less than 3 meters (relative to mean sea level). The presently available data-base is usable in the detection of map errors, survey of drainage areas, development of wide area survey information of remote and underdeveloped areas, and verification of the underlying theory and usefulness of satellite and aircraft radar sensors designed specifically for these purposes. In this report, GEOS-3 data is examined relative to the specification of system parameters needed to provide optimal height and spatial resolution. Figure 1 provides an example of the synoptic profilometry available in the present data-base.
- The radar cross-section (RCS) data is shown to be usable in assessing soil moisture content on a global seasonal basis.

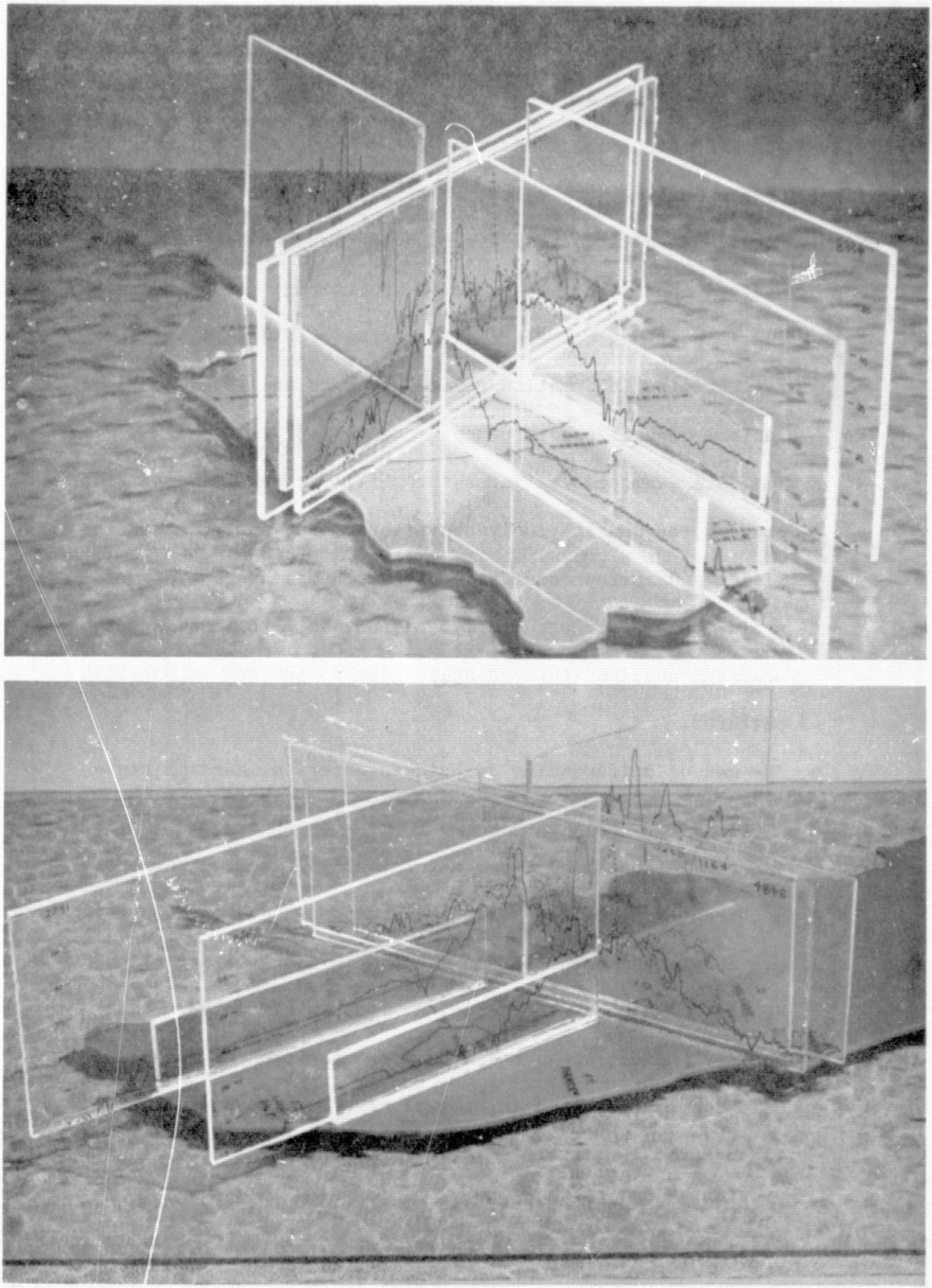

Figure 1. Overview of Florida data.

The only ingredient lacking is the extraction of baseline RCS information and the cataloging of regional data.

- The RCS values obtained from GEOS-3 have shown existing reference and textbook values to be seriously in error, both in magnitude and angular behavior. The angular dependency uncovered appears to be usable as an attitude sensor technique and is a strong correlate with surface reflectivity. This reflectivity information relates both to soil moisture and surface mineral constituency.
- The data examined validates the ability of the radar altimetry concept to quantitatively characterize regions, such as ice fields and current boundaries, through measurement of mesoscale and smaller structure, and to enable the assessment of seasonal and long-term changes in polar ice and circulation patterns.
- The use of differencing techniques offers a means of highlighting time-varying structure such as subsidence activity of earthquake zones and other natural or man-made intrusions.
- A threshold algorithm has been developed and evaluated which provides enhancement in the achievable spatial resolution. Results given show the technique is also useful as a data quality indicator, such as the identification of momentary unlock conditions and in removal of tracker dynamical errors (i.e. servo lag errors).
- A computer algorithm has been generated which produces the equivalent of per-pulse signal level data. These data appear to provide highly accurate spatial location for the altitude data.

2.0 LAND TOPOGRAPHIC RESULTS

Figure 1 is a montage of the Florida data examined to date; details of these and other passes are given in a later section of this report. The Figure 1 projection contains the satellite measured elevation data arrayed over the respective ground tracks. This overview contains a number of interesting features: The Everglades regions is discernible in the foreground of the upper figure, and is characterized by an almost constant elevation of ~ 5 meters. The river which drains Lake Okeechobee is clearly visible; as later data presentations will show, the sensor consistently displays rivers and creeks due to their strong reflectivity. The other Everglades pass contains elevation data for the region west of Ft. Lauderdale, Lake Oceechobee, and the highland region. The three closely spaced (~ 5 km separation) passes cover the region from Cape Kennedy to Ft. Meyers, Florida. The fine structure contained in these passes will be shown to accurately profile local features. (The sustained breaks or dotted-in regions represent data discontinuities.) The northern-most data is very close to the highest point in the state (near Lake Wales, Florida) and the intersection agreement between these 5 passes is excellent.

Figures 2 and 3 contain plots of the altimeter and map data for two randomly selected terrain categories along with a pictorial representation of the incident wavefront and range expanse for a 12 ns pulse. This format allows the reader to gauge the relationship between beamwidth and pulse-length limited geometry. Figure 2 shows the Florida topography to contain gentle, rolling structure which should correspond to pulse-length limited operation. The South Carolina data (Figure 3) is for moderate-roughness terrain and regions are seen for which the surface curvature exceeds the wavefront curvature; however, the tracker data shown indicates that the nadir return

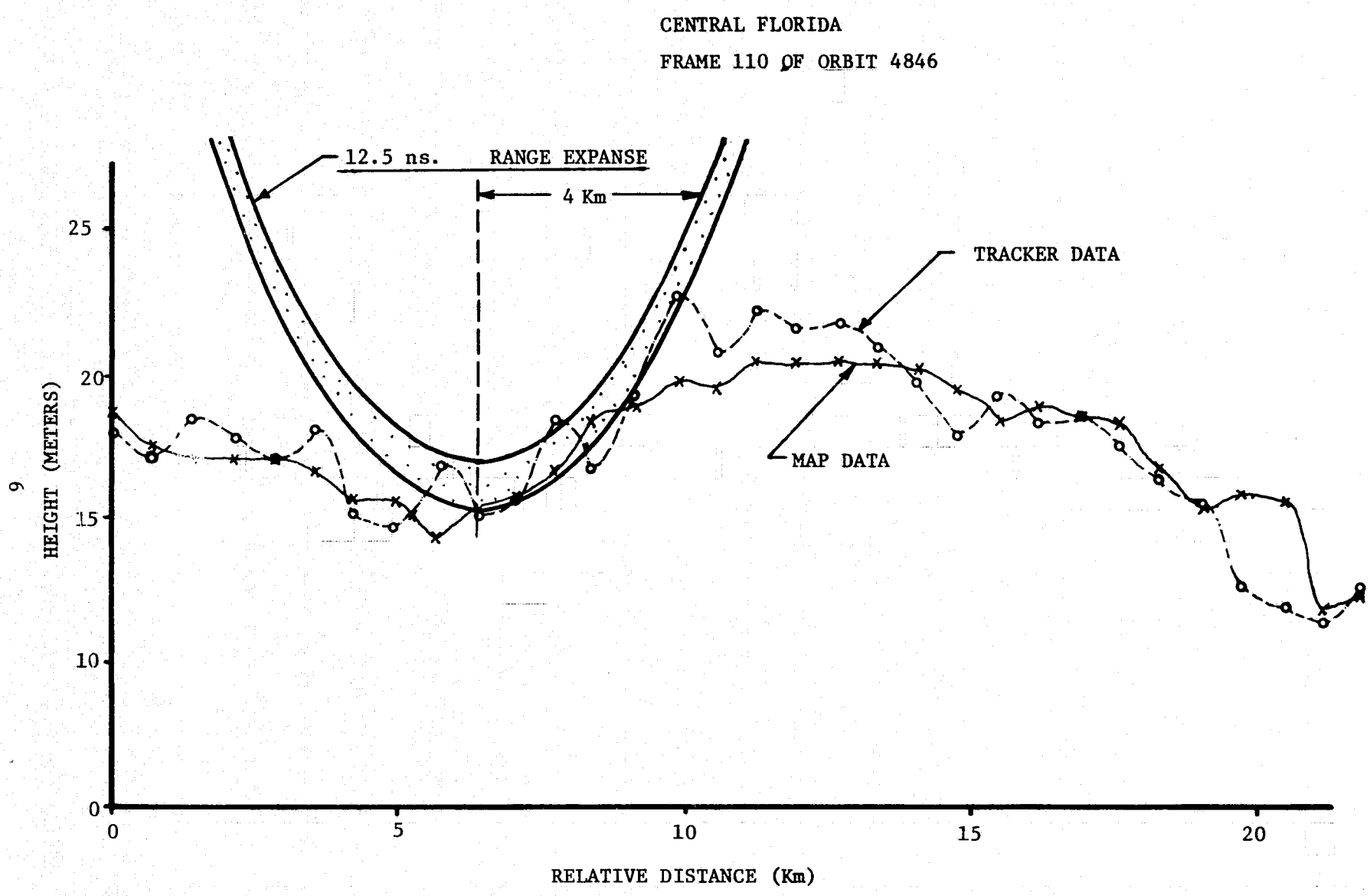

Figure 2. Comparison of altitude and map data relative to geometry of incident pulse-packet.

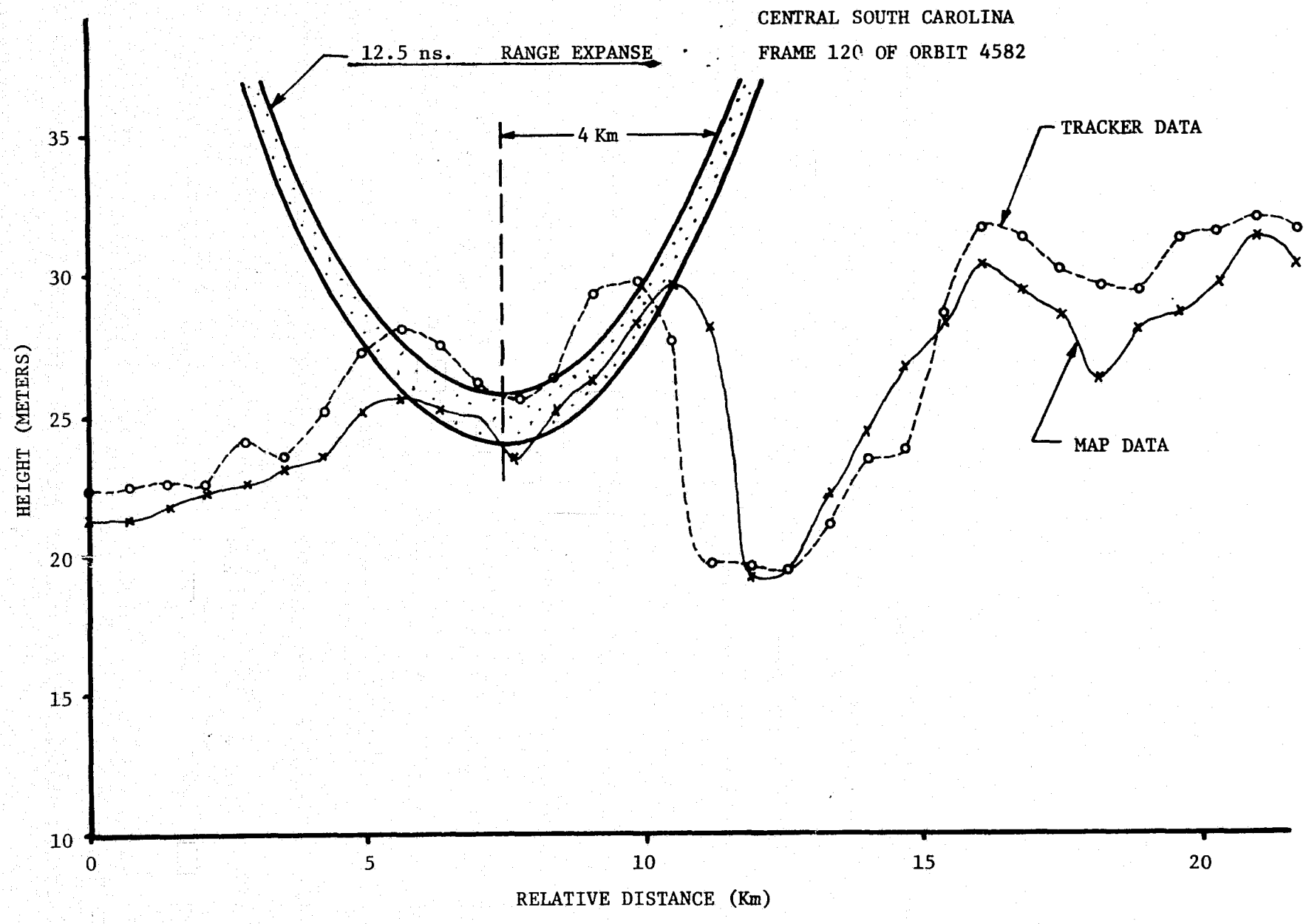

Figure 3. Comparison of altitude and map data relative to geometry of incident pulse-packet.

dominates to the extent that the sensor is able to profile inside the pulse-length constraint. Later discussions will re-examine this behavior from the standpoint of backscatter angular dependency and surface correlation length.

Figure 4 shows the satellite (tracker) data with annotations to show local features such as cities, highways, and waterways.

Figure 5 shows a comparison of satellite (threshold) data and nadir-point map data. Later discussions will examine the relative agreement between the threshold, tracker, and map data. The cluster of man-made structures is clearly evident in Figure 5 during the data-period over the city of Fort Meyers. Referring back to Figure 4, the automated threshold technique was used to delete data for periods in which the system was unlocked. The triangle symbols appearing in Figure 5 indicate these loss-of-lock periods.

Figure 6 also gives a comparison of on-board tracker and threshold data. This pass (orbit 2236) began off Wallops Island, Virginia, and the segment shown terminates midway between the ocean and Chesapeake Bay. Again the threshold results display a data unlock which occurred between time periods in which the track status is displayed in the telemetry data. These tracker unlock periods are primarily due to the tracker bandwidth and tracking gate spacings used in the Intensive Mode (I-Mode) on GEOS-3. These parameters were chosen to provide bias-immune operation under a wide range of sea state conditions. The 16 waveform samplers, however, in conjunction with software techniques, such as the threshold tracker, permit the split-gate tracking errors to be removed.

Figure 7 contains a somewhat different altitude presentation. The previous altitude related figures contained data which had been processed using a linear-regression technique to equate the mean-sea-level values for the

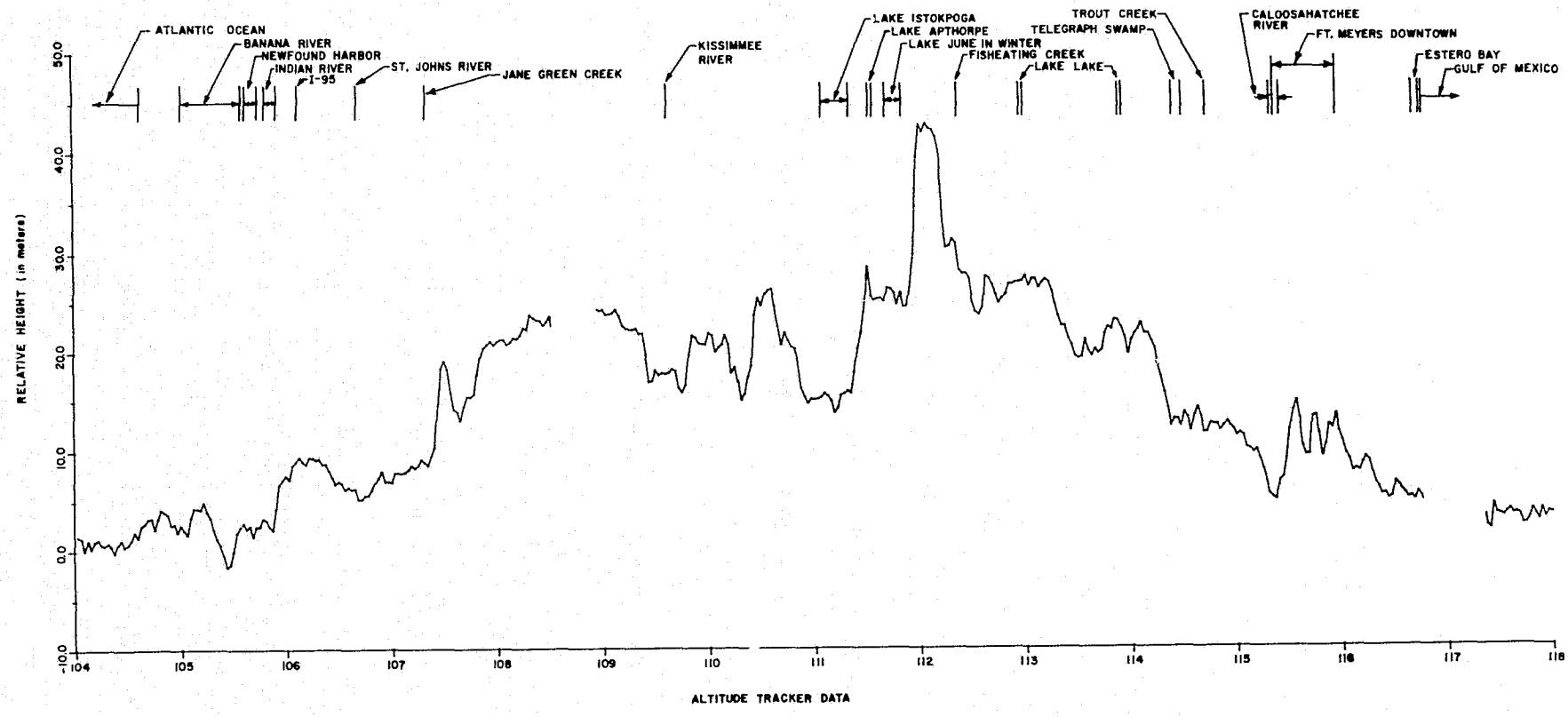

Figure 4. Central Florida Altimeter Data (Orbit 4846).

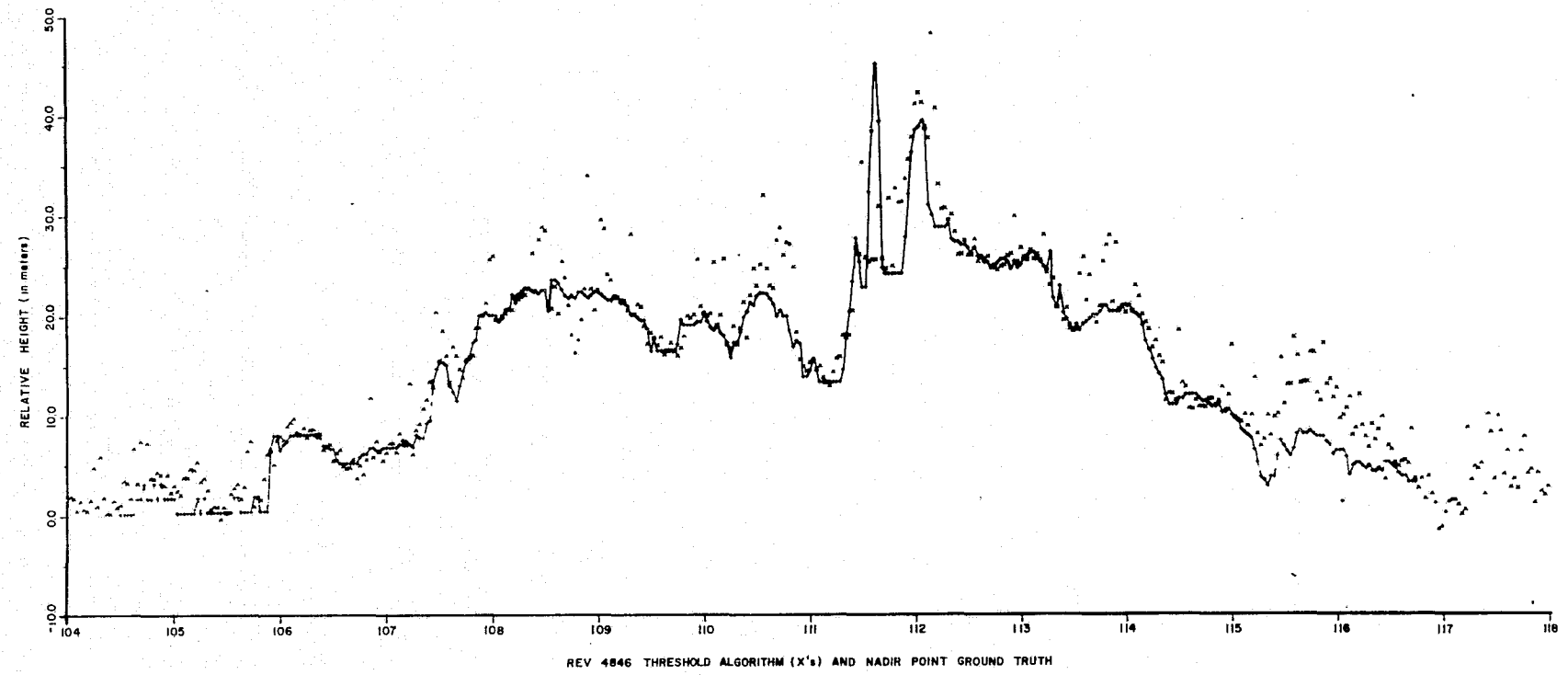

Figure 5. Orbit 4846 threshold algorithm and map data.

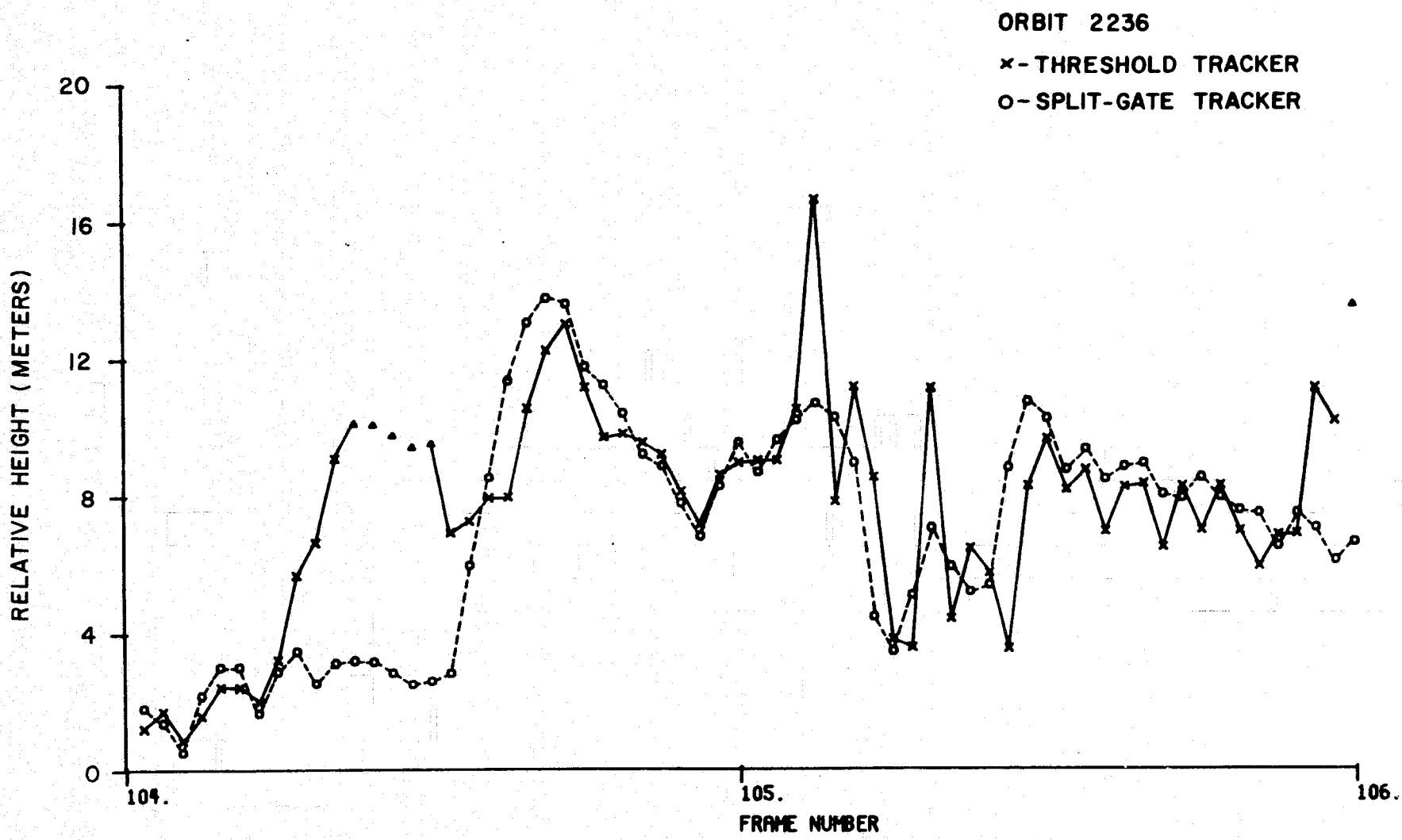

Figure 6. Comparison of split-gate tracker and threshold data, over the eastern shore of Virginia.

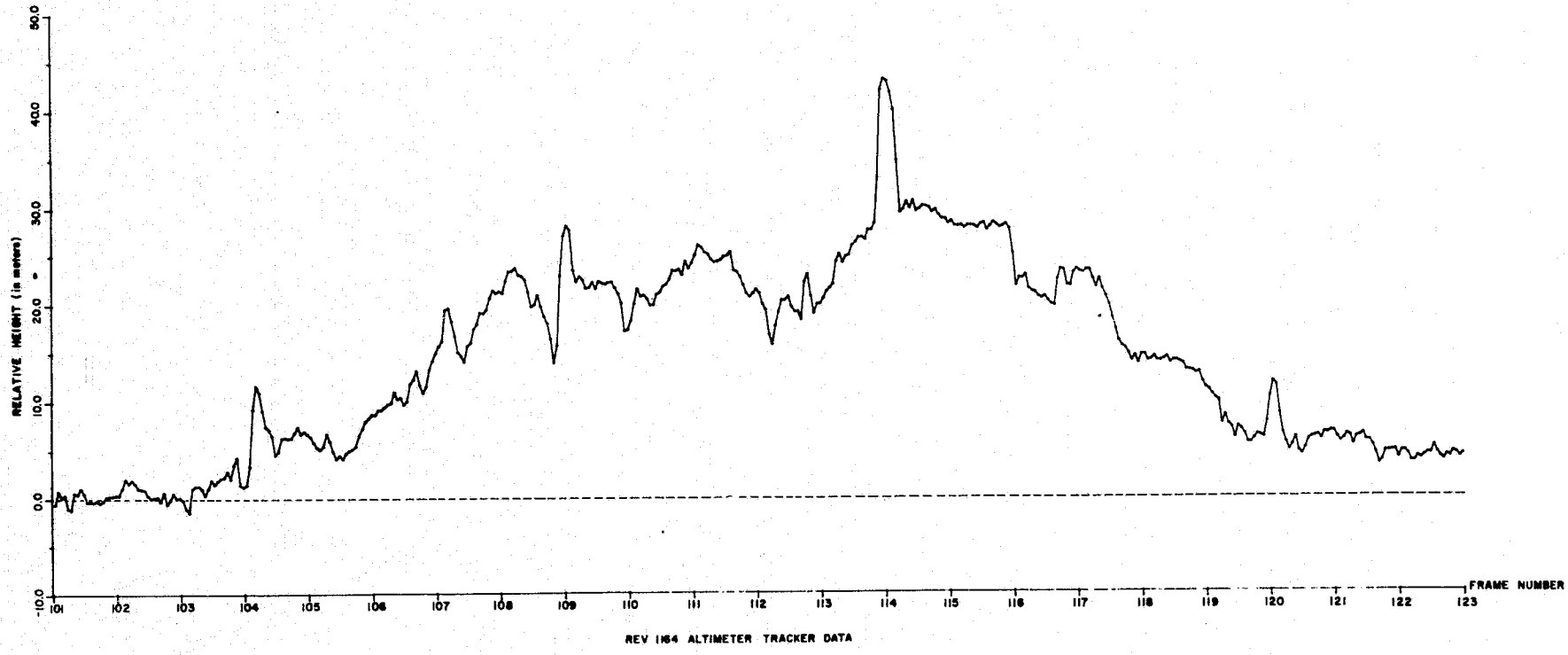

Figure 7. Altimetric data showing geoidal changes between Atlantic Ocean and Gulf of Mexico.

Atlantic ocean and the Gulf of Mexico. This was done to place the altitude and map data on a comparable basis. In effect, this linear-regression removes the first-order geoidal effects from the over-land data. Figure 7 shows the unaltered GEOS-3 data-base; note that a difference of ~ 5 meters exists in the two sea-level values. This difference is in very close agreement with recent geoidal charts [2]. The Figure 7 presentation suggests the possibility of recovering the over-land gravity anomalies from the GEOS-3 data. For cases in which accurate tracks exist for over-land segments, such as over inland lakes, it should be possible to characterize the geoid if accurate orthometric height data is also available in map form. Calculations given in Appendix A show the gravity anomaly across Florida to be ~ 1.5 milligals.

2.1 Spatial Resolution

Figure 8 exemplifies the analytical results relating to spatial resolution for altimeter operation over natural terrain. As discussed in section 1.6, the spatial resolution for rivers, highways and man-made objects appears to be much greater, perhaps 0.1 km. The vertical scale in Figure 8 shows degree of correlation between the satellite and map data and the horizontal axis corresponds to spot-size or spatial resolution. This figure indicates the spatial resolution for GEOS-3 over open terrain to be in the neighborhood of 1-3 km. This result is surprising for two reasons; theoretical and experimental analyses based on the system response-time (~ 12 ns) indicated the over-water resolution to be ~ 3.4 km and the over-land response was assumed, by some, to be the area illuminated by the antenna beamwidth (~ 20 km). Later discussions will show the latter view to be unappropriate for the majority of the land areas in the continental U. S. Only rough

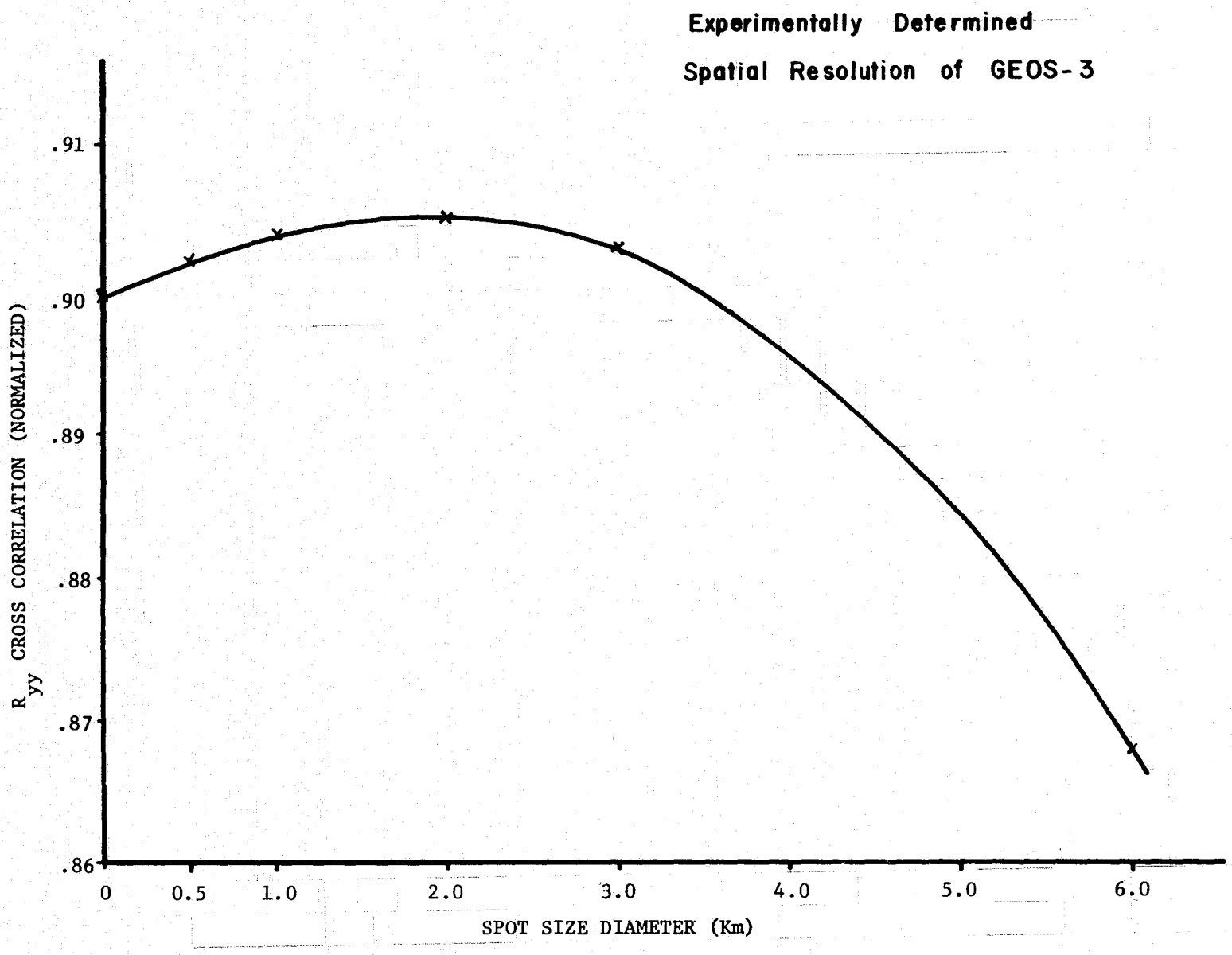

Figure 8. Degree of correlation between threshold altitude data versus diameter of spatial averaged map data. (Frame 107 of orbit 4846).

terrain regions pertain to beamwidth limited operation of GEOS-3. Secondly, the unexpected rapid decay in reflectivity with off-nadir angle observed over-land appears to further reduce the effective spot-size below the 3.4 km value. Other factors to be discussed also reduce the effective illuminated area.

2.2 Land Reflectivity

Figure 9 is a graph of the above mentioned reflectivity versus angle behavior. This figure shows both over-land and over-ocean reflectivity. Only extremely calm or "glassy" sea behavior is shown since normal seas do not show perceptible decay versus angle. The three terrain regions shown represent those initially examined and, compared to previously published angular decay, the dependency was so strong that an error in data reduction was initially suspected. Subsequent data studies have corroborated this result and established this behavior for these terrain categories. The attitude/specular gate sensed decay of the plateau region has been found to be an extremely reliable indicator of ice and land regions. Figure 10 displays waveform data used to derive this angular sensitivity. The GEOS-3 mean-waveforms over-land show a marked absence of the constant or plateau characteristic of over-ocean waveforms. The data regions given in Figure 8 correspond to waveform samplers 6-16, the AGC gate value at 25 ns following gate 16, and the attitude/specular gate (ASG) following gate 16 by ~800 ns. Translation of these timing events into angular variables reproduces the graph shown in Figure 9.

Radar cross-section results typical of those obtained with GEOS-3 are shown in Figure 11. This figure shows σ° values for ocean, land, and ice regions. These values and the related data processing considerations are

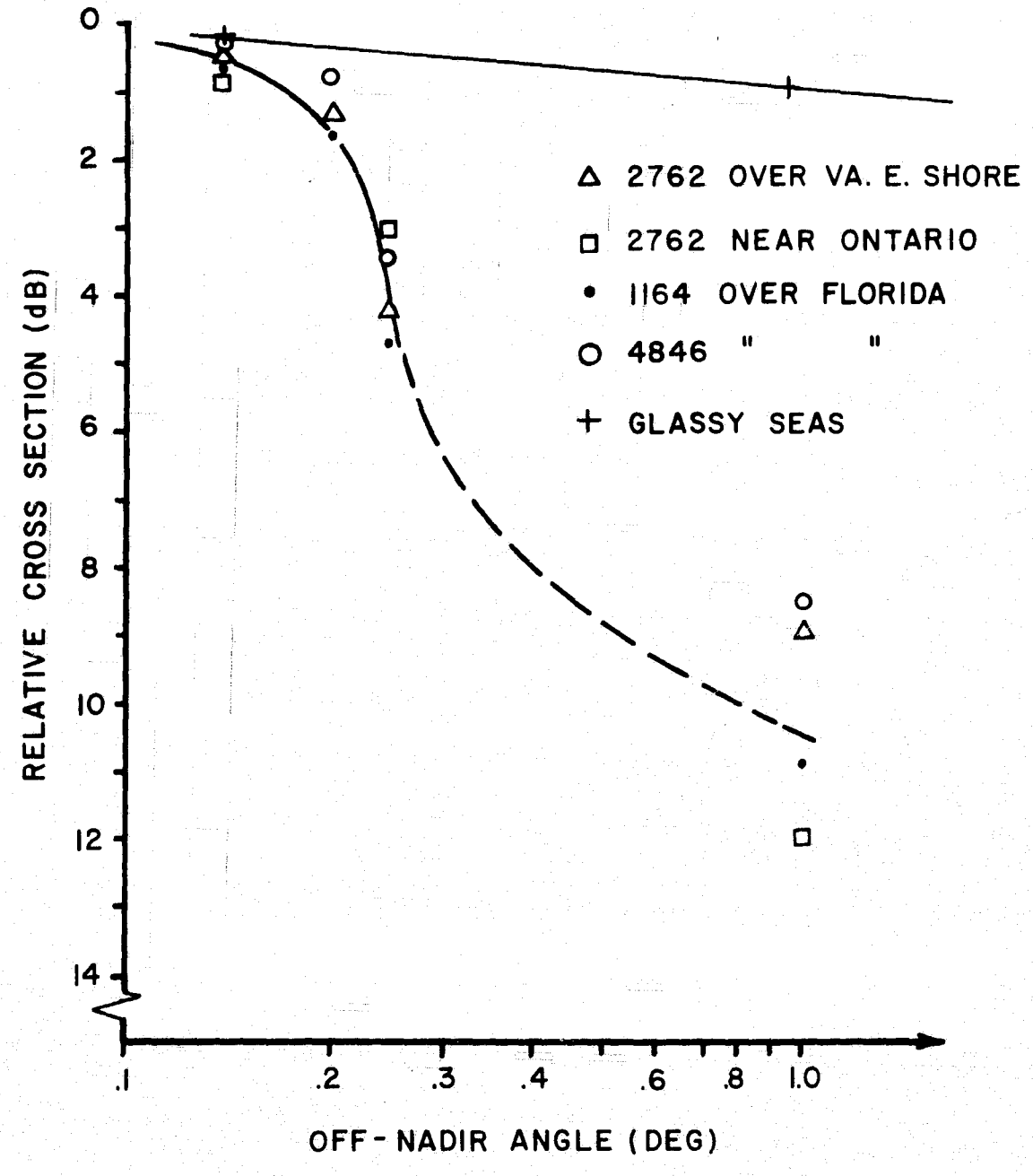

Figure 9. Backscatter angular dependency for ocean, land and ice region.

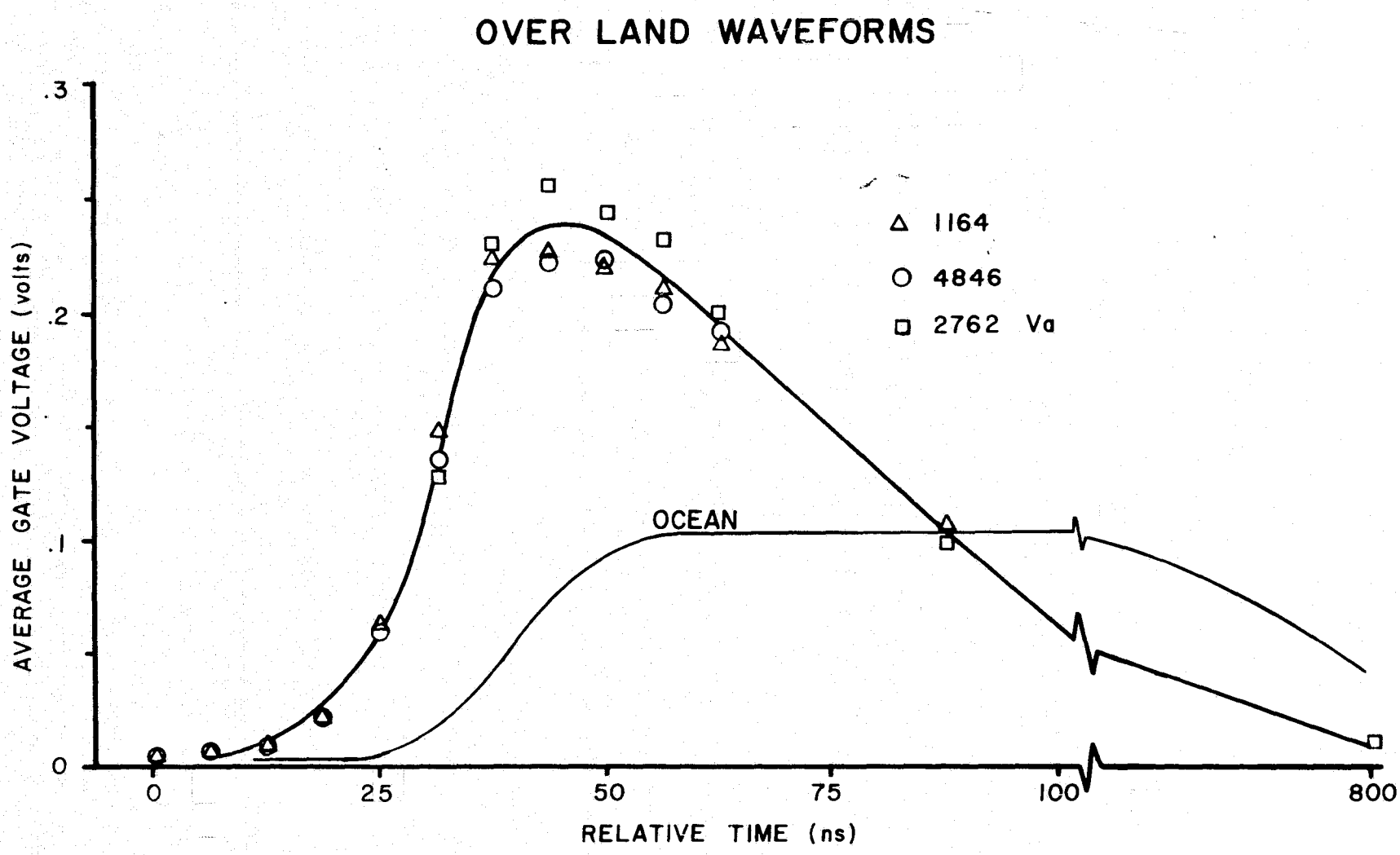

Figure 10. Typical over-land waveforms.

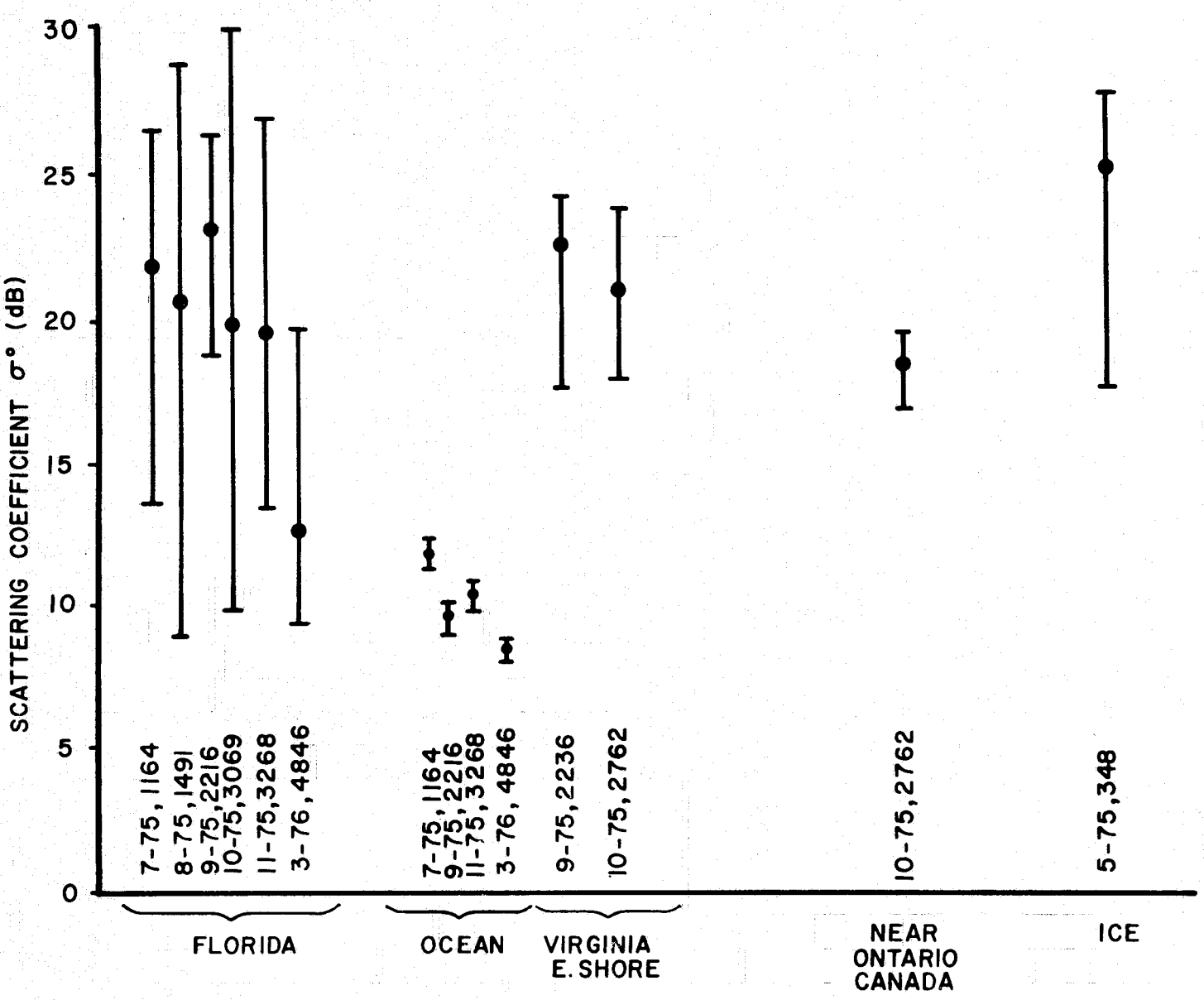

Figure 11. Radar Cross Section Results for several target categories; Upper and Lower limits correspond to per-frame averages.

given in section 3.0. The salient result to be discussed here is the approximate order-or-magnitude larger backscatter for these terrain categories than for typical over-ocean regions. Also notable in these results is the striking seasonal dependency present in the Florida data; this dependency is thought to be the result of seasonal rainfall and not of the effects of vegetative canopy. Other, recent analyses of terrain backscatter have shown even greater scatter in over-land σ° values; per-frame and geographic variations of four orders-of-magnitude have been observed.

In this and later discussions the term σ° has been used without qualification. For σ° values > 30 dB the definition of cross-section per unit area may be inappropriate since the backscatter may not be simply area dependent. The σ° terminology will be used throughout, subject to this caveat.

2.3 Waveform Related Results

Figure 12 contains data from an interesting ground track; this pass encompasses virtually the entire spectrum of radar target categories. Figure 12 shows the following symbols and information:

(a) the on-board altitude-tracker data consists of the solid line,

(b) the "two-consecutive" threshold tracker data is shown as the "x" symbol with the lower-limit values shown as triangles,

(c) per-frame waveforms are shown for the annotated geographic regions; these waveforms represent on-board averages for which saturation and other corrections have not been applied,

(d) radar cross-section ($\tilde{\sigma}^\circ$) values are shown in which the tilde is used to indicate values corresponding to the (~ 3dB lower) AGC gate values not the peak-waveform (or nadir) value (AGC

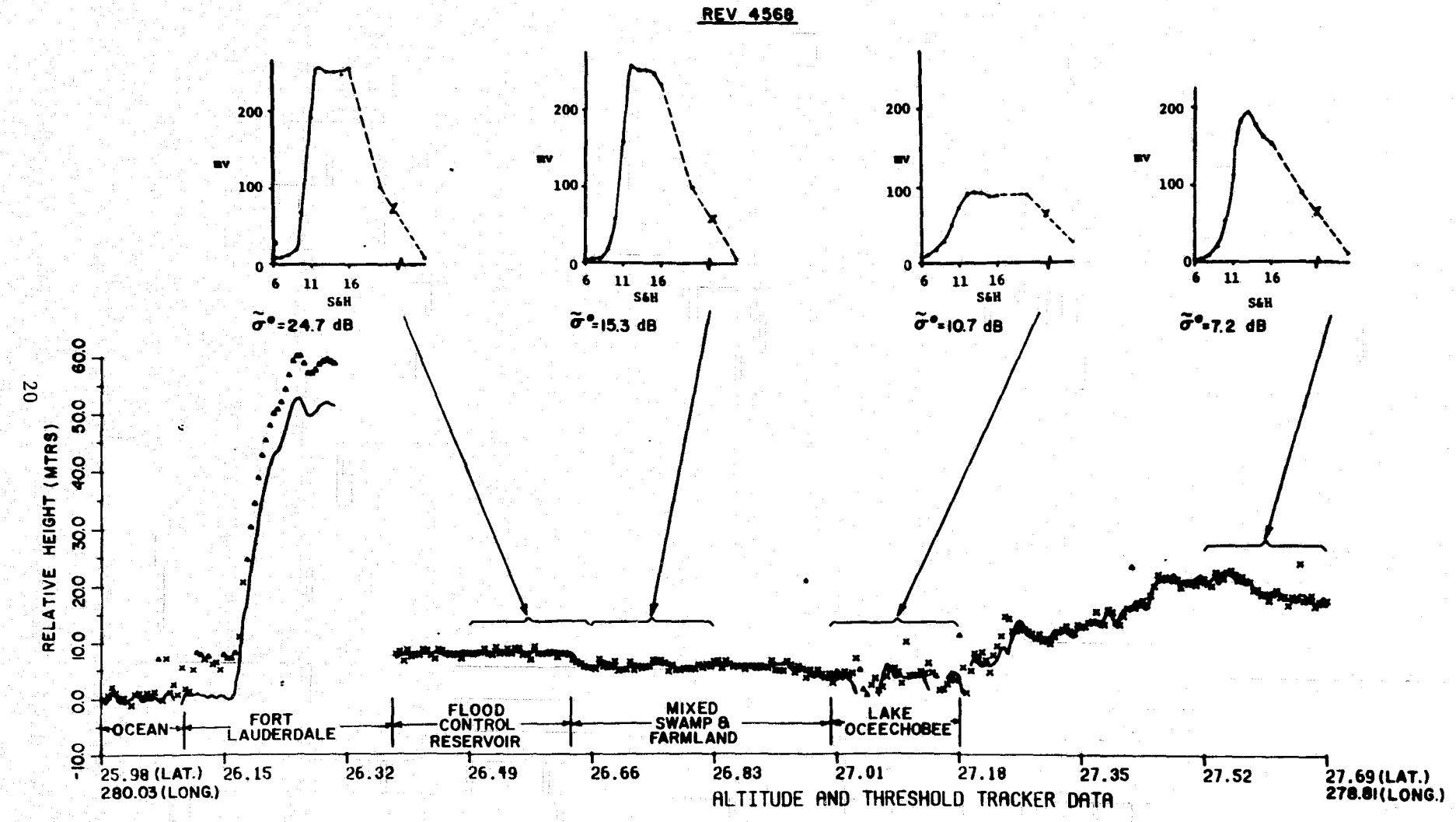

Figure 12. Altimeter and waveform data for a variety of topographic conditions, Orbit 4568.

"clean-signal" calibrations were used),

(3) the abscissa shows the terrain category, the latitude and the beginning and ending longitudes.

Data from this pass were initially scrutinized because of the 3 meter change which apparently occurred over a uniform marsh area; this change indicated a possible sensor malfunction. Referring to Figure 12, data shown for this pass begins during an over-ocean region which is followed by a step-change in altitude of ~ 60 meters, an unlock period, and continuous altimetric data until pass termination at 27.7° Latitude. Examination of map data showed that the 60 meter change occurred over the commercialized area of Fort Lauderdale and re-acquisition was achieved over the Everglades swamp region. Subsequent analyses indicated that the 60 meter change was due to high-rise buildings in the neighborhood of the beach and the ~ 3 meter discontinuity over the marsh area was due to a diked region used as a flood control reservoir. The South Florida Flood Control Authority was contacted; they confirmed this level (for this data) and indicated that active pumping was used to maintain the indicated level. The on-board tracker data (Figure 12) also shows the Okeechobee Lake region (with data discontinuities triggered by the water-land boundaries) and entrance into the Central Florida highland region.

The threshold data contains several noteworthy features. These data show the beach occurrence to be ~ .07 degrees (Latitude) prior to the on-board tracker response, the tracker to continually lag the topographic characteristics over the populated beach region, and the unlock conditions over Lake Okeechobee. Aside from these features, the threshold and on-board tracker are in very good agreement.

The waveform data shown in Figure 12 comprises the 6-16 Sample and Hold (S&H) gate values, the AGC gate value (located ~26 ns from gate 16), followed by the attitude/specular gate value (~800 ns from the leading edge). The "over-swamp" regions shown comprise the first known, point target responses recorded for GEOS-3; these are similar to the waveshapes obtained from Skylab over the Utah Salt Flats [3]. Note that the sampling gates saturate at a value of ~250 m.v., the 100 m.v. pulse width is ~50 n.s., and that the extrapolated half-power pulse width of 12.5 n.s. corresponds to an amplitude ~10 dB higher than the AGC value, and that the $\tilde{\sigma}^\circ$ values shown are downward biased by ~13 dB. These corrections infer a nadir σ° of approximately 38 dB. The Lake Okeechobee waveform can be seen to correspond to the familiar over-ocean waveshapes, which, to the writer's knowledge, represents the first instance that ocean-like waveforms have been observed for a land-locked water region. The final waveform shown in Figure 12 is the familiar over-land configuration reported herein (c.f. Figure 10). Before leaving Figure 12, it should be noted that the along-track spatial resolution could be obtained from these data, if detailed surface-truth were available for the near-step change in altitude that occurs at the reservoir terminus. Assuming the feature to be a true step-change, the scaled spatial response is in the neighborhood of 1.5 km.

The σ° values inferred by these data are 28 - 40 dB for marsh areas and ~ 13 dB for inland lakes. Of primary interest are the saturated or over-marsh values; note that σ° = 28 - 40 dB corresponds to near-specular conditions for which capillary wave or wind effects are not significant. For this value of σ° to pertain, the backscattered signal must be essentially coherent [3]; as such the variance of the fluctuation statistics should be

very small. Figures 13 and 14 show fluctuation histograms and autocovariance functions for the marshland and highlands areas. The calculated standard deviation of the altitude jitter for the marsh area is 0.3 m, and 2.0 m for the over land region. The histogram for the land segment is similar to other over-land histograms to be discussed. The marsh-area histogram is difficult to interpret - it suggests Ricean statistics [4] but the strong saturation effects in other regions of the waveform make it difficult to assess tracking jitter effects. The covariance functions indicate substantial pulse-to-pulse correlation in both cases. This result indicates that higher pulse repetition rates would produce only modest improvements in over-land tracking quality.

3.0 GULF STREAM RESULTS

Work in this area has concentrated on development of digital processing techniques to enhance the Gulf Stream signature.* Figure 15 typifies the general problem; the upper plot shows the filtered sea-surface height data and the lower plot shows the same data except that a straight line has been subtracted-out to permit magnification of the vertical axis. The data for each graph was filtered using;

- an 81 point equal weight (or arithmetic) averager which yields an 8 second time constant, and
- a Wiener convolution filter which has an effective time constant of ~2.5 sec.

Addressing first the Gulf Stream recognition problem; Figure 15 displays a fairly complex topographic signature which contains fine-structure not present in the existing geoid or dynamic topography references. This particular

*To the best of the writer's knowledge, Von Arx was the first to suggest use of height changes in the study of correct features.

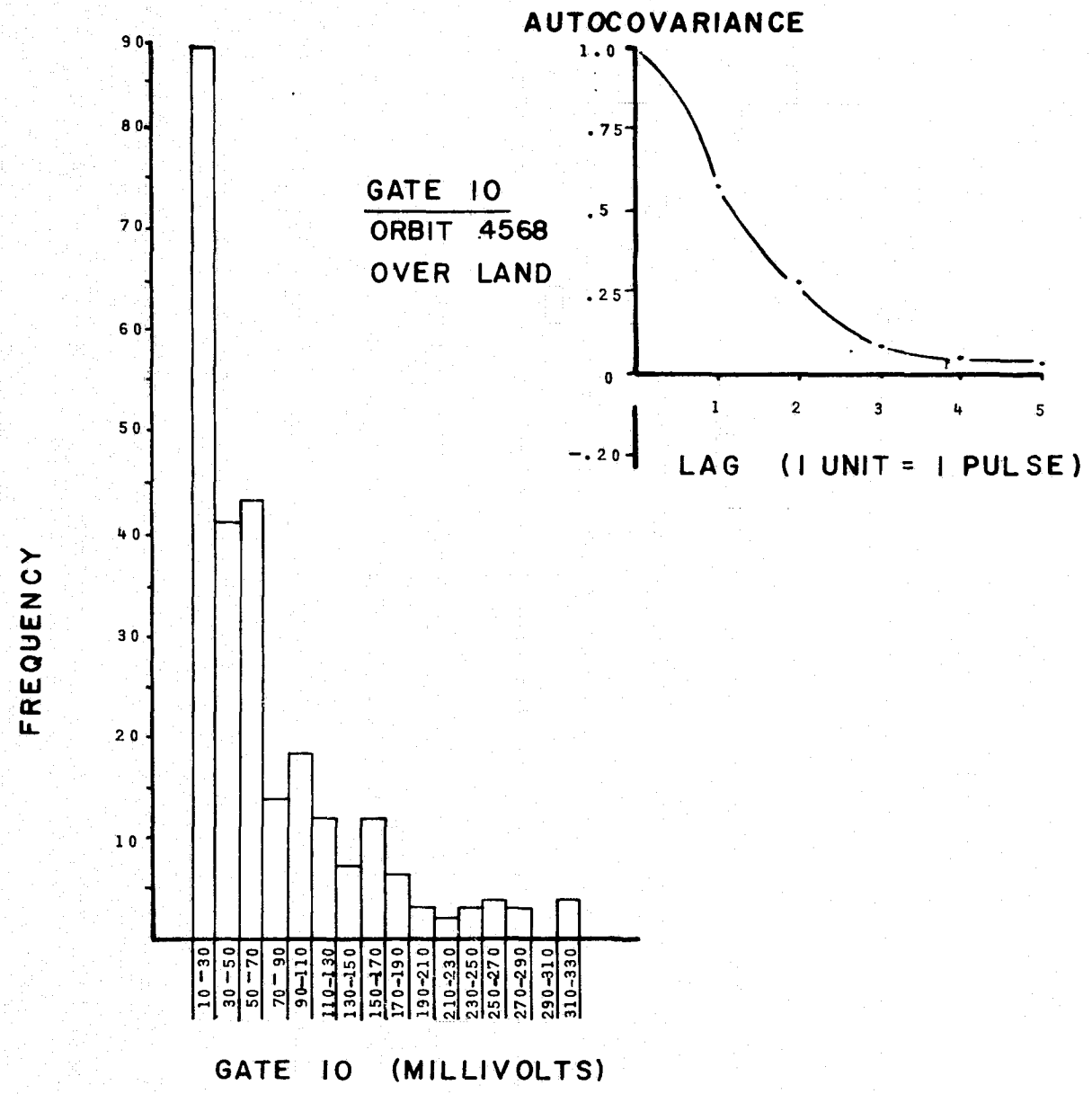

Figure 13. Signal fluctuation histogram and autocovariance for highland area; orbit 4568.

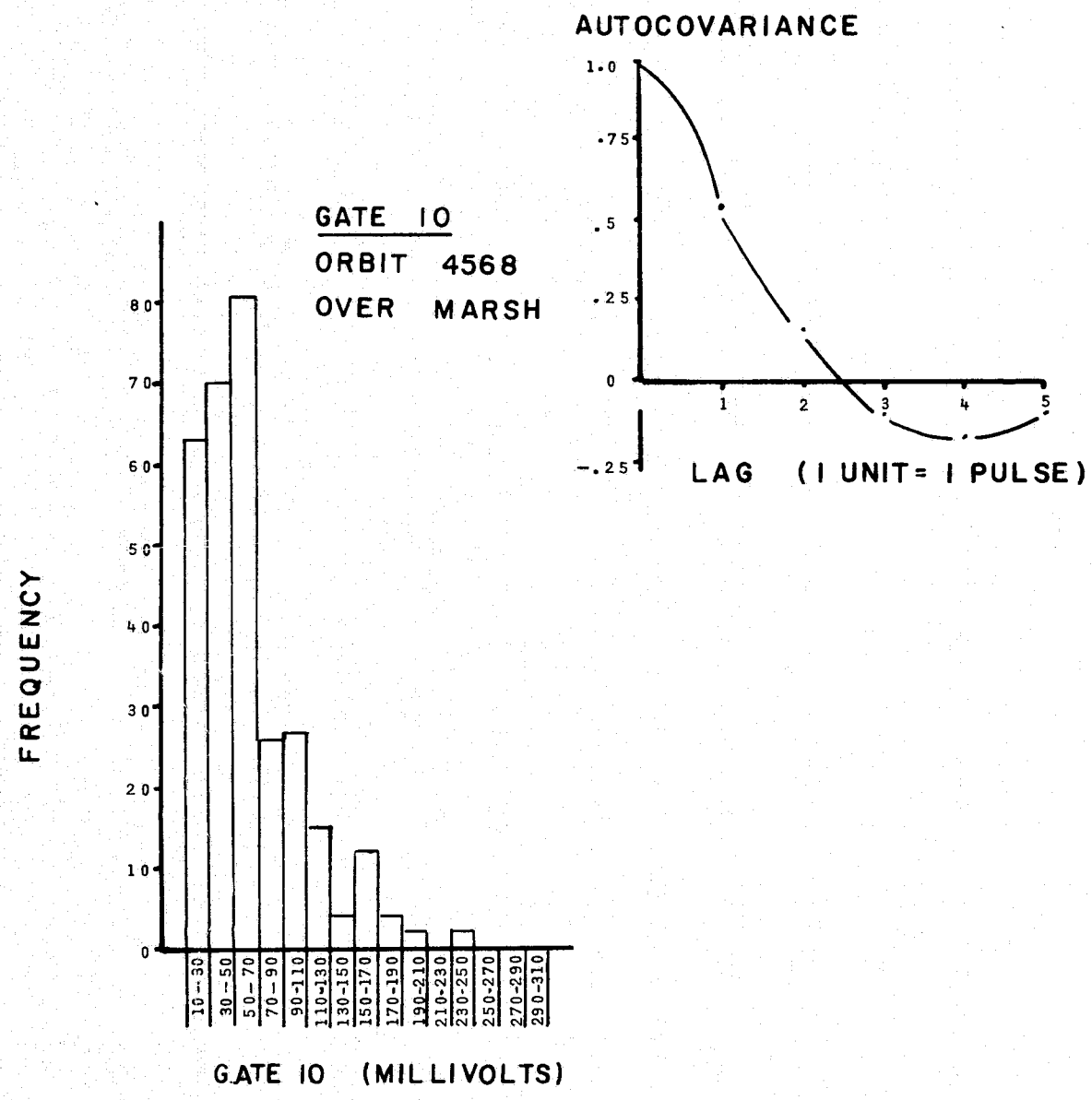

Figure 14. Signal fluctuation histogram and autocovariance for marsh area; orbit 4568.

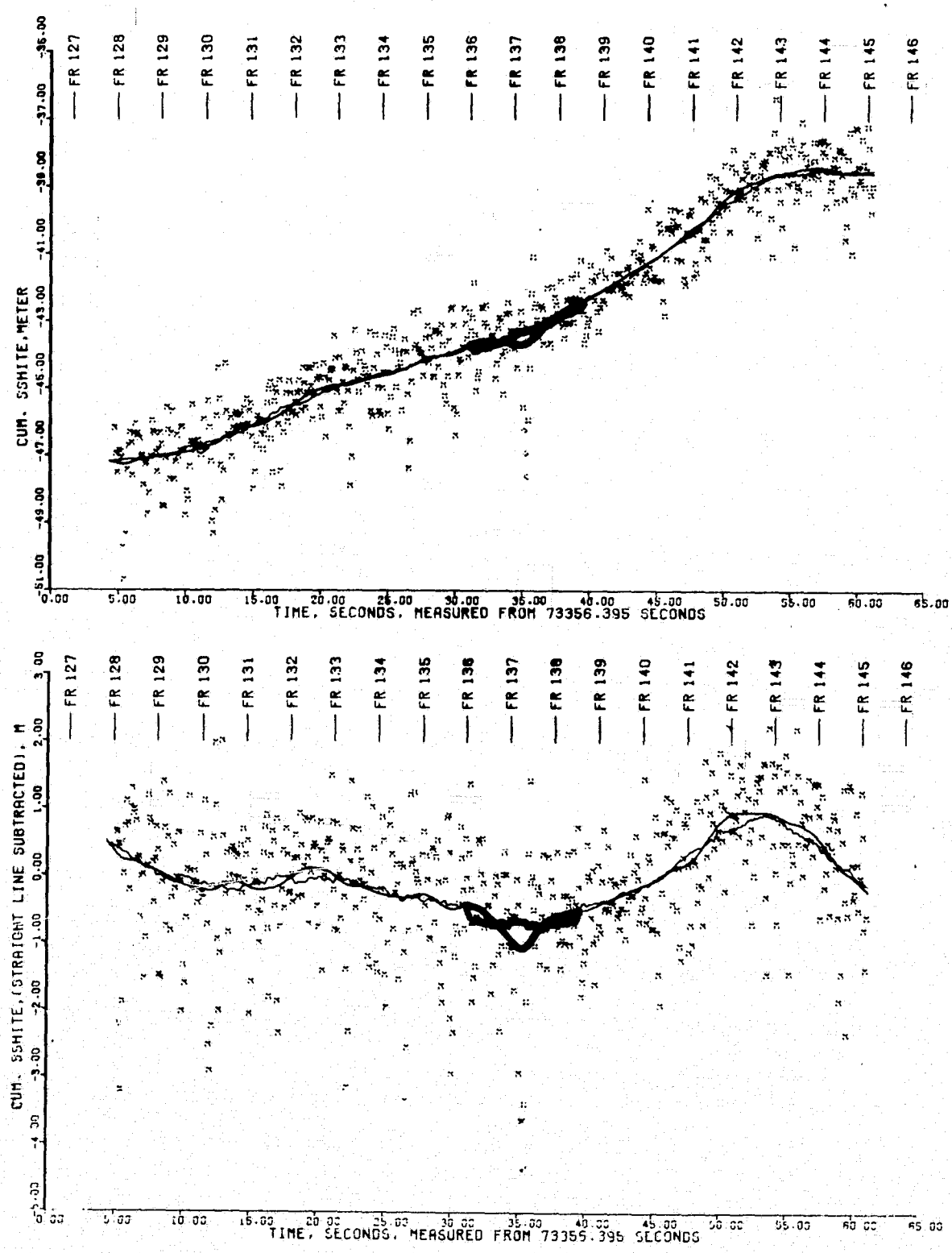

Figure 15. Raw and filtered altitude data in the vicinity of the Gulf Stream; orbit 1710.

geographic area (Figure 16) was initially selected because comparisons with other (farther south) passes showed it to be comparatively well behaved; continental margin geoidal effects for passes off the coasts of Georgia and the Carolinas are much larger than the expected Gulf Stream effect. Also, north of Norfolk, Va., the stream tends to break-up into smaller streams which are more difficult to detect. As a means of providing positive stream identification, a series of near-overlapping passes were assembled. Three such passes have been received to date; these are shown in Figure 17. This figure indicates a significant change in current features between pass 1710 and the other two passes. Use of existing theoretical estimates of the Gulf Stream signature suggests the following model: assuming that stream integrity does not exist during pass 1710, the near-land features can be matched in all three passes. Therefore, use of 1710 as the permanent topographic estimate yields the stream signatures shown as the difference between the pass data and the dashed line. This model shows a substantial western countercurrent with a main-stream deflection of ~0.6 m. These features are in good agreement with calculated stream characteristics [5]. Several other near-overlapping passes will be available in this area; this technique should be continued and detection of eddy structure attempted as the data-base increases. (Cloud cover prevented acquisition of surface truth data for passes 1710 and 2236.)

Turning next to a comparison of filtering techniques, Figure 15 shows two interesting characteristics. The rectangular window or arithmetic-average filter, which spans 81 points or ~8.1 sec., is seen to contain much more residual noise than does the ~2.5 sec Wiener Filter. Also, note in the lower graph near t = 35 sec a number of wild data-points occur. The Wiener filter is seen to directly respond to these wild points. The arithmetic average, however, produces a valley or notch of time-span equal to its window,

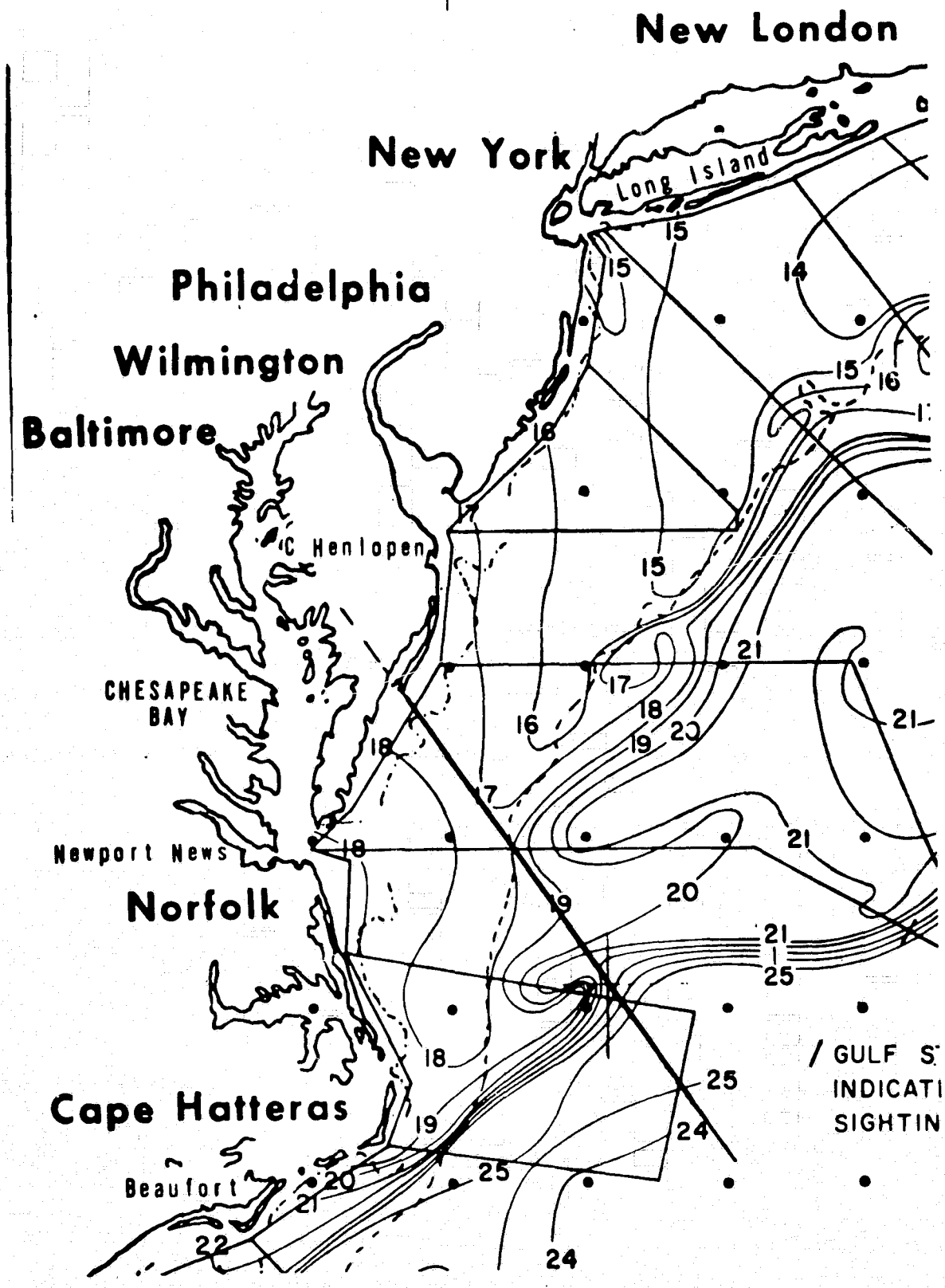

Figure 16. Surface truth map for orbit 2762.

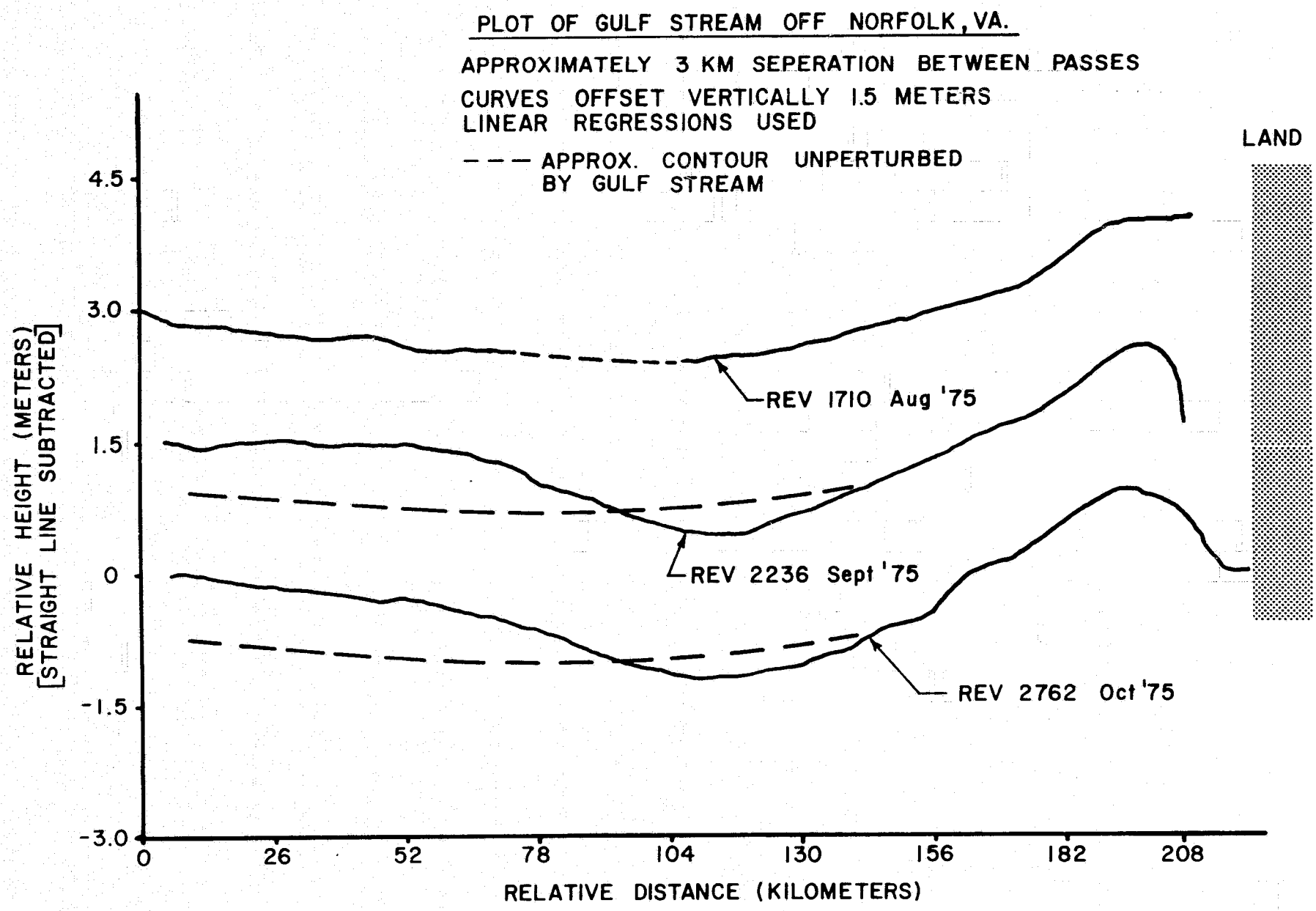

Figure 17. A comparison of altitude data over the Gulf Stream.

because of these near-unlock values. A moment's reflection shows this to be reasonable behavior for this type of filter, albeit a misleading response. The reason for this behavior is that an equally weighted filter responds to wild points to the maximum extent as soon as these points enter the computation, and the effect or offset persists until the lead-data points exit the computation. In the writers view, this is a very undesirable feature of rectangular window filters. Figure 18 compares filter characteristics from the standpoint of their response to a step change in input data. Note that the (two-sided) Wiener filter follows the step input with zero-lag and finite rise time. The rectangular window filter again displays its high-frequency-pass characteristics through the corner or knee at each extremity. Since the high-frequency response of a rectangular filter decays slowly (sinx/x), the response would be expected to be rich in high frequency content. The Wiener filter equations used here are given in Appendix B.

Figure 19 displays a plot of the Gulf Stream in the region of maximum current velocity. This pass (2791) represents the western-most pass of the south-north passes shown in Figure 1; it spans the region of the Florida Straits between Cuba and Key Largo. Note that the sea-surface height change is in excess of 5 meters. The available geoid data for this region shows essentially a constant geoid value and the change observed is attributed to the relatively high stream velocity. This rectangular average also shows the "notching" characteristic discussed above; this feature is discernible in the region centered on 22.88 degrees latitude.

One other feature present in Figure 15 deserves comment. The raw data points (shown as x symbols) show marked asymmetry. Stated another way, the residuals are significantly non-Gaussian. This effect has been noted

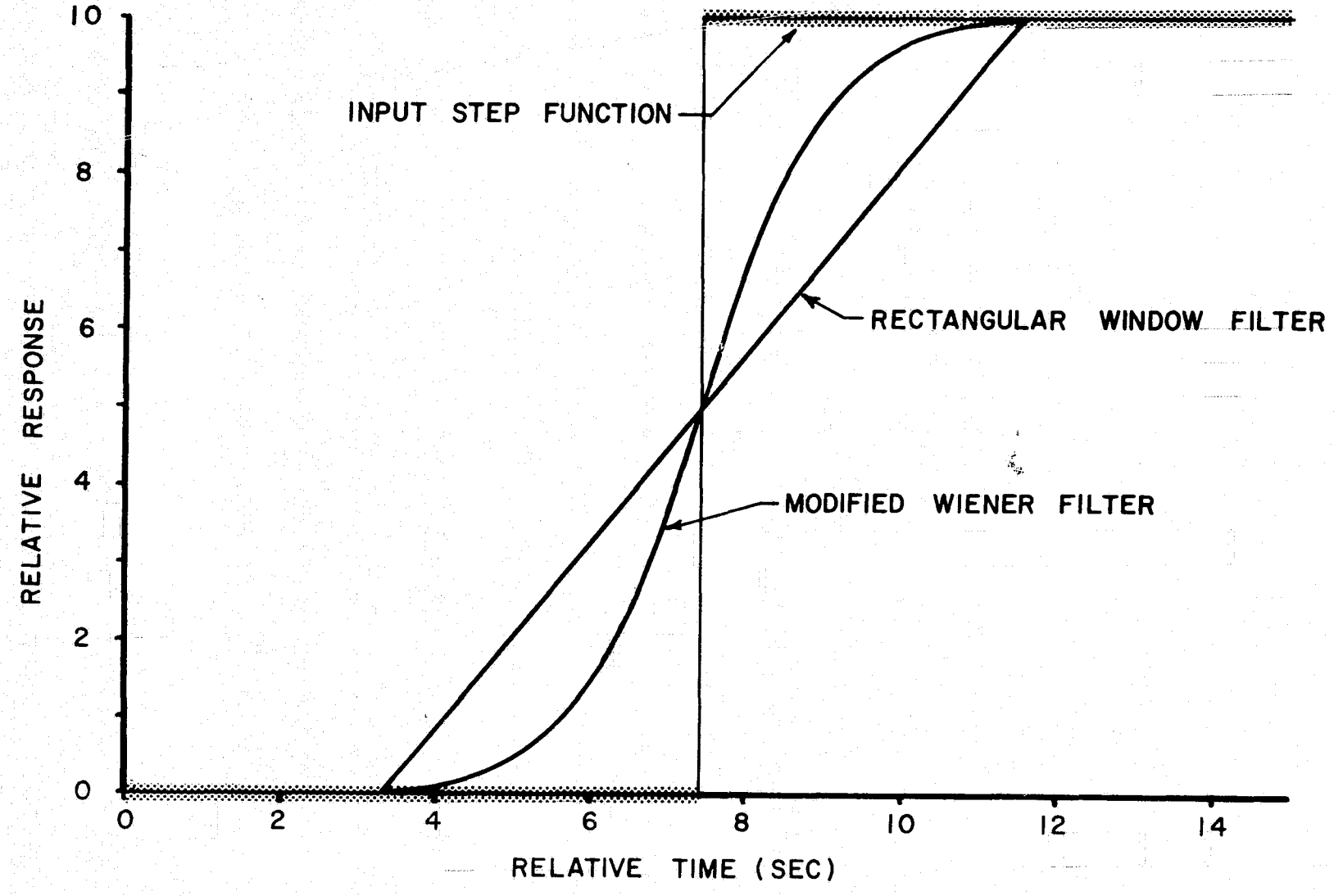

Figure 18. Step-response of rectangular and Wiener Filters.

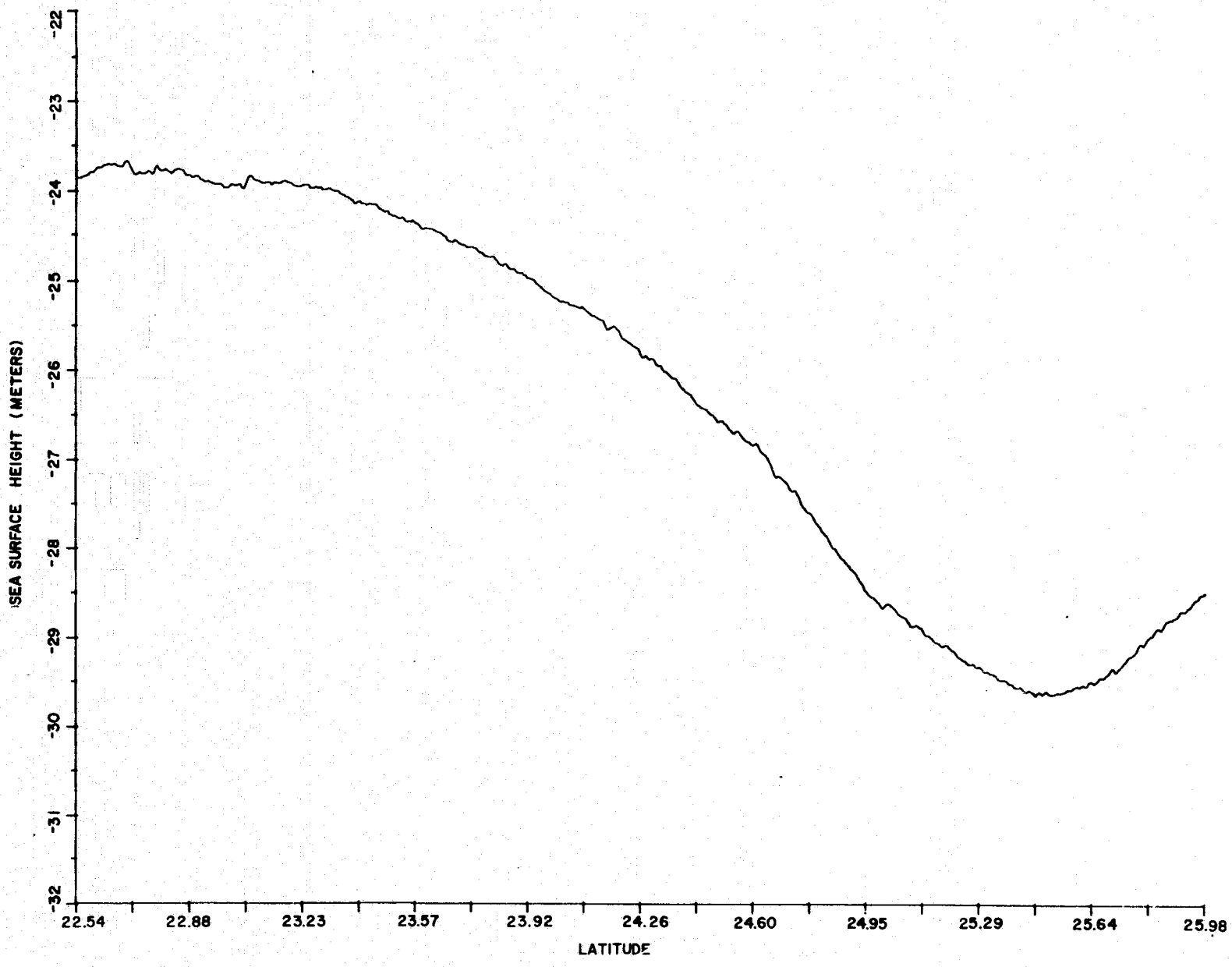

Figure 19. Gulf Stream deflection across the Florida Straits.

previously [6 and 7]; the design of future filter algorithms should take due cognizance of this (temperature dependent) non-Gaussian behavior of the tracking loop.

Figures 20 and 21 show geoidal and topographic power spectral densities for two separate geographic regions. These plots contain horizontal scales in units of Hz. relative to the altitude tracker signal for the GEOS-3 orbit, and in units of Km relative to actual surface wavelength. Figure 20 represents data calculated from Skylab observations over the Puerto Rican trench: Figure 21 contains calculated densities for two closely spaced GEOS-3 passes over the Hatteras Abyssal Plain, continental margin, and the Gulf Stream. Both the Skylab and GEOS-3 densities show strong similarities. The two GEOS-3 passes were for differing tracker noise levels, rms values were 1.5 for rev 2602 and .07 m. for rev 2620. These results suggest that the statistical a prioris used in design of altitude filters can be taken to be locally homogeneous. However, such algorithms should be based on density characteristics, especially magnitudes, appropriate to the area under investigation.

4.0 ANALYSIS OF AGC AND VIDEO SIGNAL CHARACTERISTICS

Radar cross section values showing per-frame maximum and minimum values were discussed in connection with Figure 12. At the other extreme, per pulse fluctuation histograms were given in Figures 13 and 14 which, among other things, showed the presence of total signal fades. This section considers the information available from this combination of effects.

Studies were initially carried out using AGC records from several geographic locations. Figure 22 contains one such record; in general the AGC records, because of the ~1 sec response time, were found to be amorphous with little correlation with ground characteristics. Studies were then

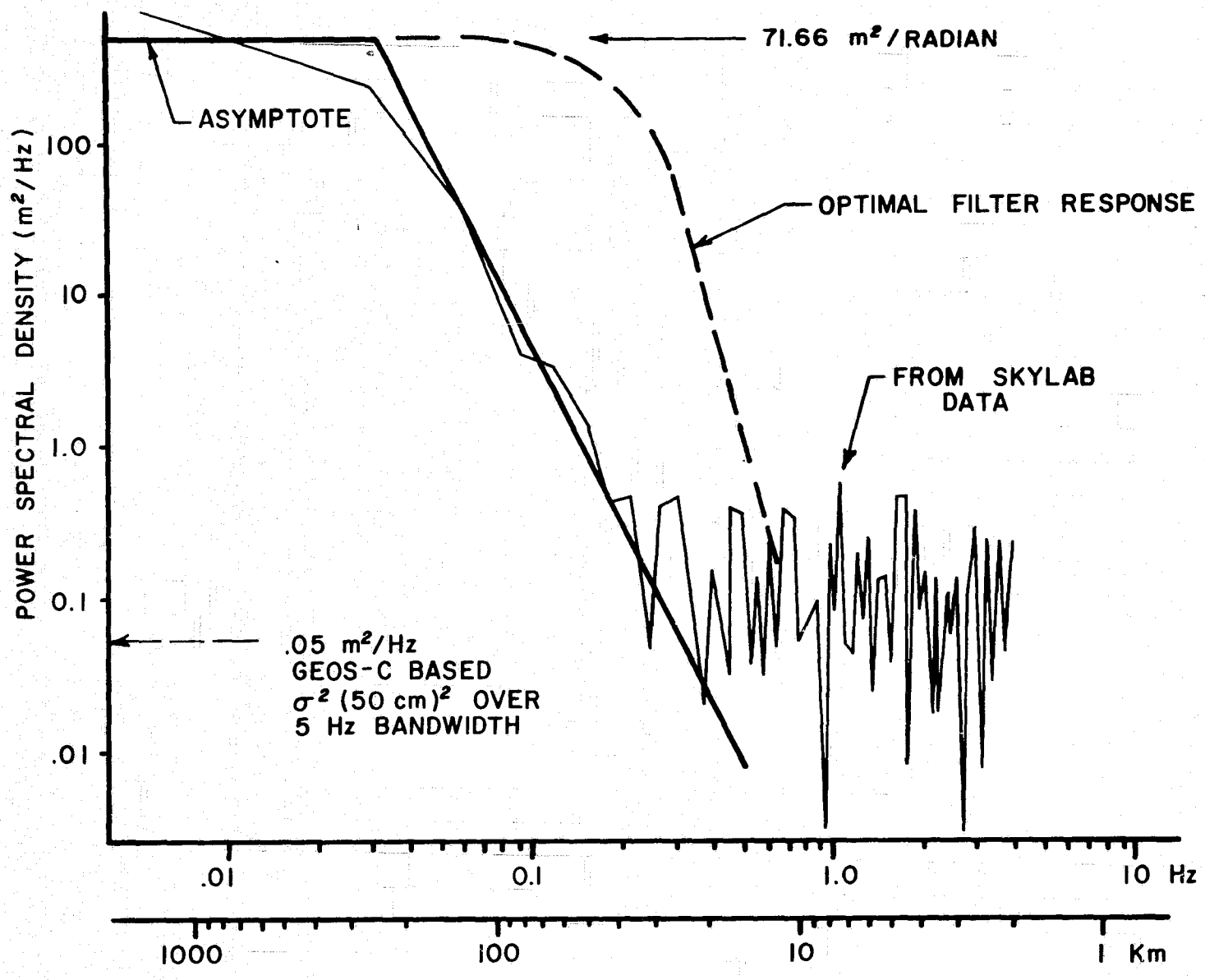

Figure 20. Geoid undulation spectrum of Puerto Rican Trench Area and Wiener Filter transfer function [Miller & Brown, 1974].

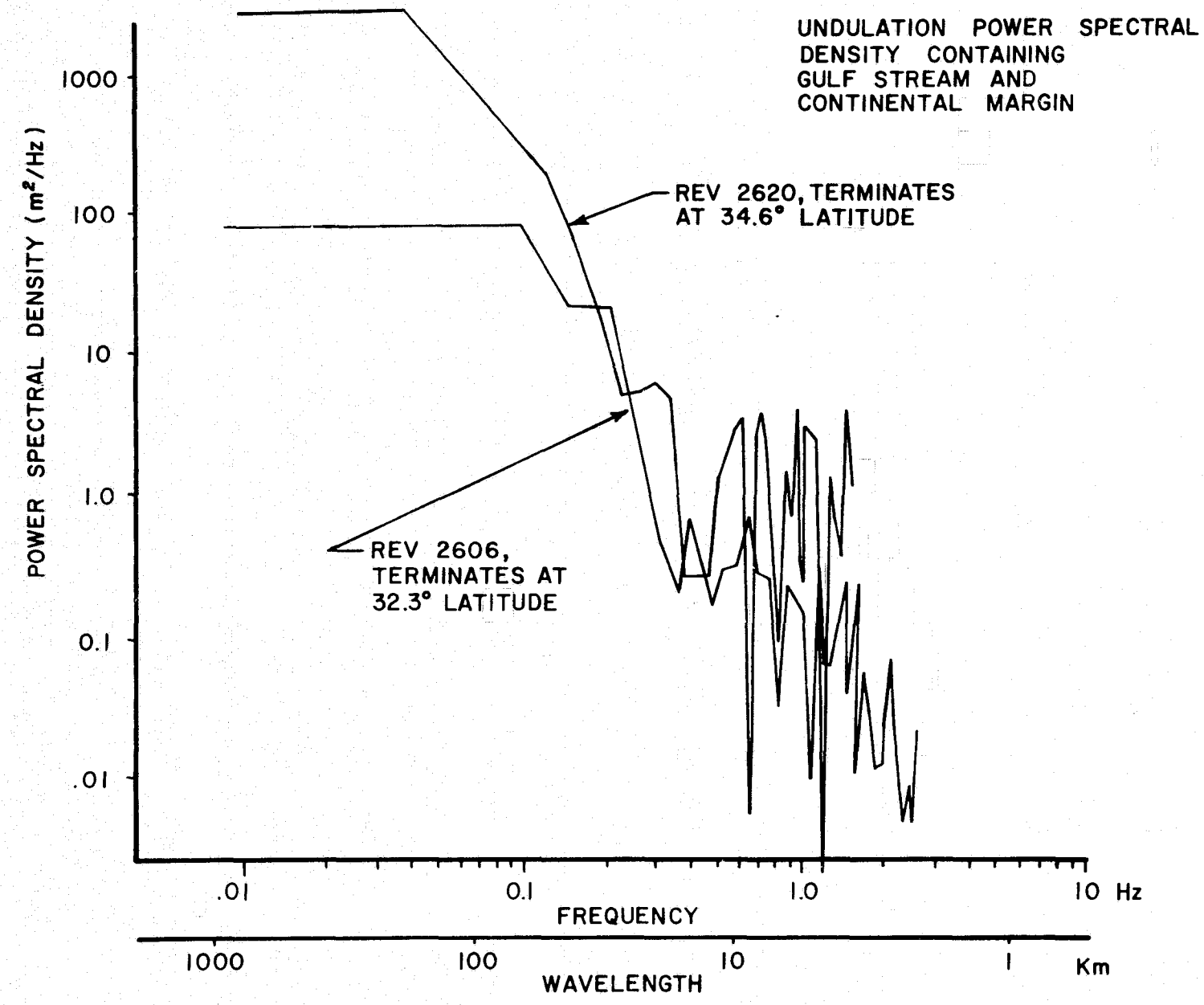

Figure 21. Geoid undulation spectrum off the coast of South Carolina (~100 km separation in ground track).

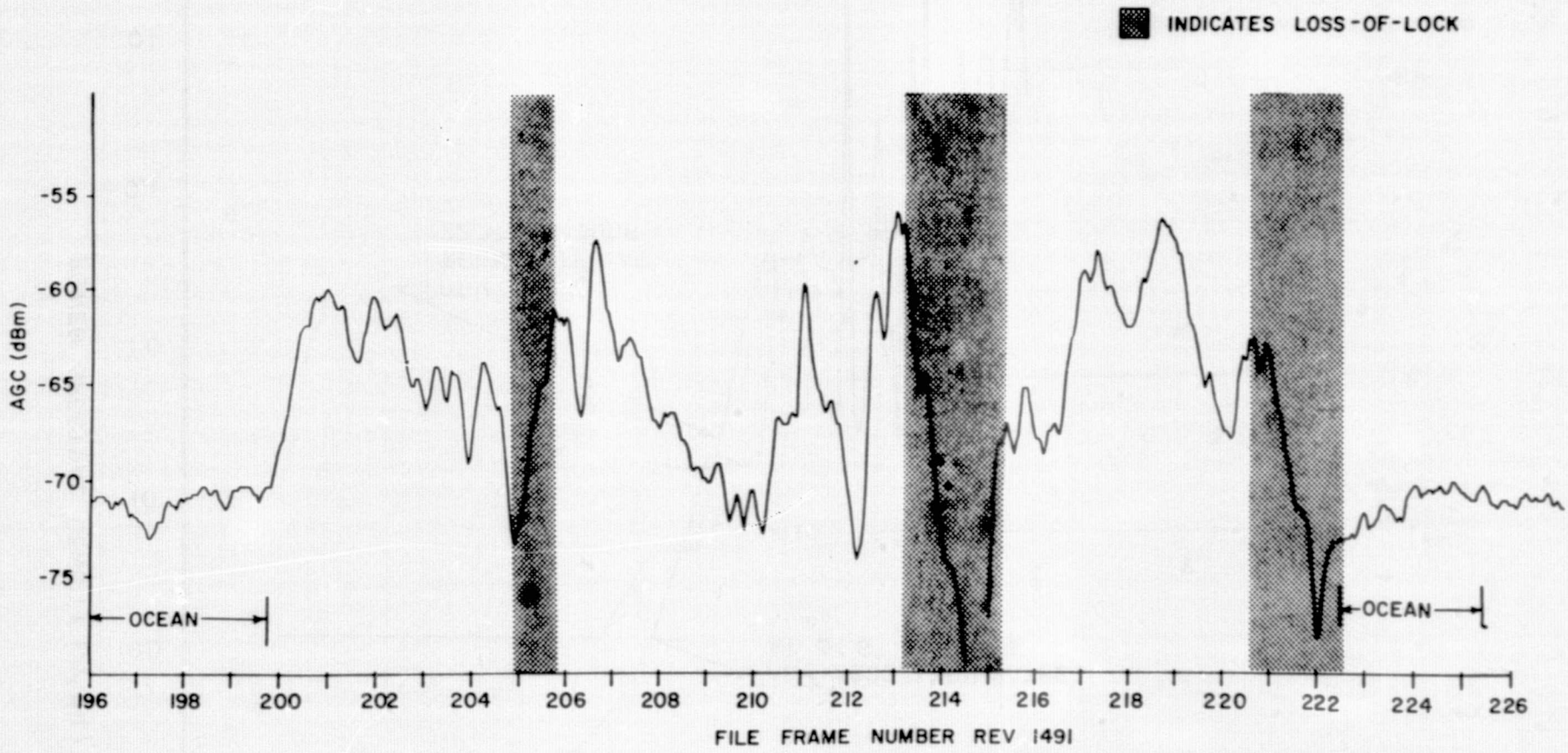

Figure 22. AGC data for Central Florida (Orbit 1491).

initiated to investigate the information content of digitally constructed pulse-by-pulse AGC or, more precisely, video data. Such records were produced by digitally superimposing the waveform data from gate 16 on the AGC data. Use of instantaneous plateau gate (the AGC gate) values would have been preferable, however, Mode 3 data was not available for use.

The reconstructed per-pulse signal level data was obtained by assuming the GEOS-3 receiver to consist of linear operations with square-law detection. To first order, the video signal (voltage) was taken to be proportional to received power. Gate 16 data was used because of the less frequent saturation compared to gates 12 - 15; and because of the lower level of tracking jitter modulation compared to the ramp-region gates.

Figure 23 shows typical results obtained using this procedure. This figure shows (a) the satellite ground track, and (b) the per-pulse signal level in the format of dBm value versus frame location. These results are rather striking; the shoreline, highways, and other surface features can, in some cases, be identified with individual pulses. These data provide extremely precise orbital and timing connotations. Also, the large pulse-to-pulse variations suggest backscatter from one-dominant, or isolated targets in many cases.

This behavior suggests that normal incidence active radar may provide surface resolution much in excess of that initially suspected. The per-pulse signatures observed strongly violate the over-ocean spatial filter effect [8]. In future activities, a number of closely spaced Mode 3 passes will be analyzed to test this hypothesis. The resolution implied by Figure 23 appears to approximate that anticipated for the SEA SAT imaging radar. Figure 23 indicates that the backscatter angular response is dominated by

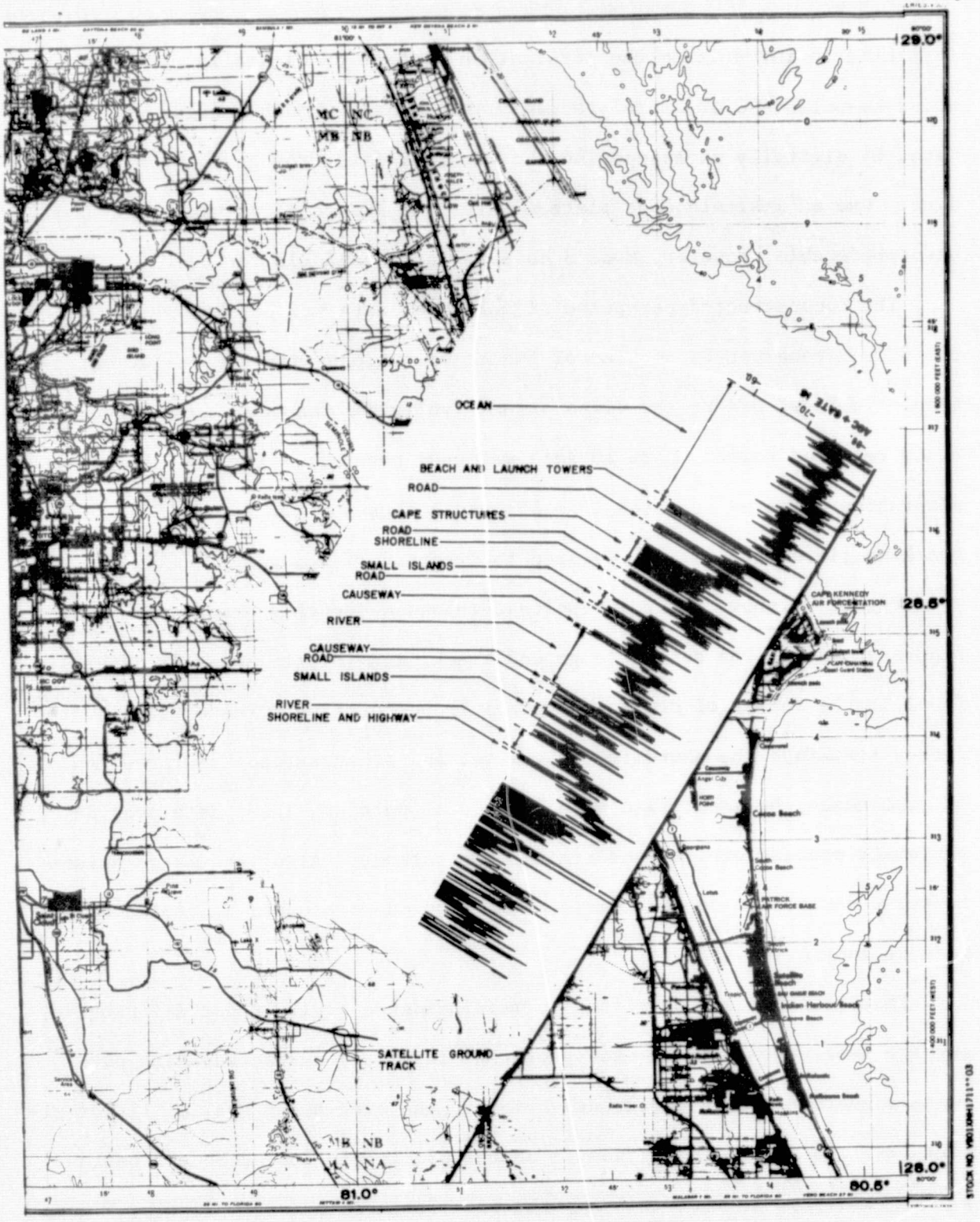

Figure 23. Comparison of map features and 100/second signal level data.

scene diffraction effects rather than spacecraft antenna resolution. Other sensor concepts such as use of synchronous detection and across track spatial diversity are suggested. These results have not yet been correlated with the observed resolution in the altimeter data.

5.0 DETAILED OVER-LAND RESULTS

This chapter begins with a discussion of the details for each of the satellite passes analyzed. Some of these passes are then re-examined from the standpoint of system performance characteristics and physical surface features extractable from the satellite data.

The four closely spaced passes across Central Florida initially studied were orbits 1164 (0630 hrs. on 7-1-75), 2216 (1500 hours on 9-9-75), 3268 (2400 hours on 11-26-75) and 4846 (1200 hours on 3-17-76).* All of these passes entered Florida at Cape Canaveral and exited near Fort Meyers, Florida; typical separation between these passes was 5 Km. All passes discussed in this report were in Intensive Mode operation; of the above four, only 4846 and 3268 corresponded to high data rate operation.

Figures 24-26 show the profiles produced by orbits 2216 and 1164. Orbit 2216 is a reasonably firm track with several brief loss-of-track conditions. Orbit 1164 ostensibly produced continuous data across Florida, however, since it is a low data-rate-pass threshold values are not available to ensure data quality throughout the pass.

Referring to Figure 26, from the midpoint of frame 101 to the first of

---

*Data from three of these passes was contained in Figure 1; pass 2216 was not shown in this figure.

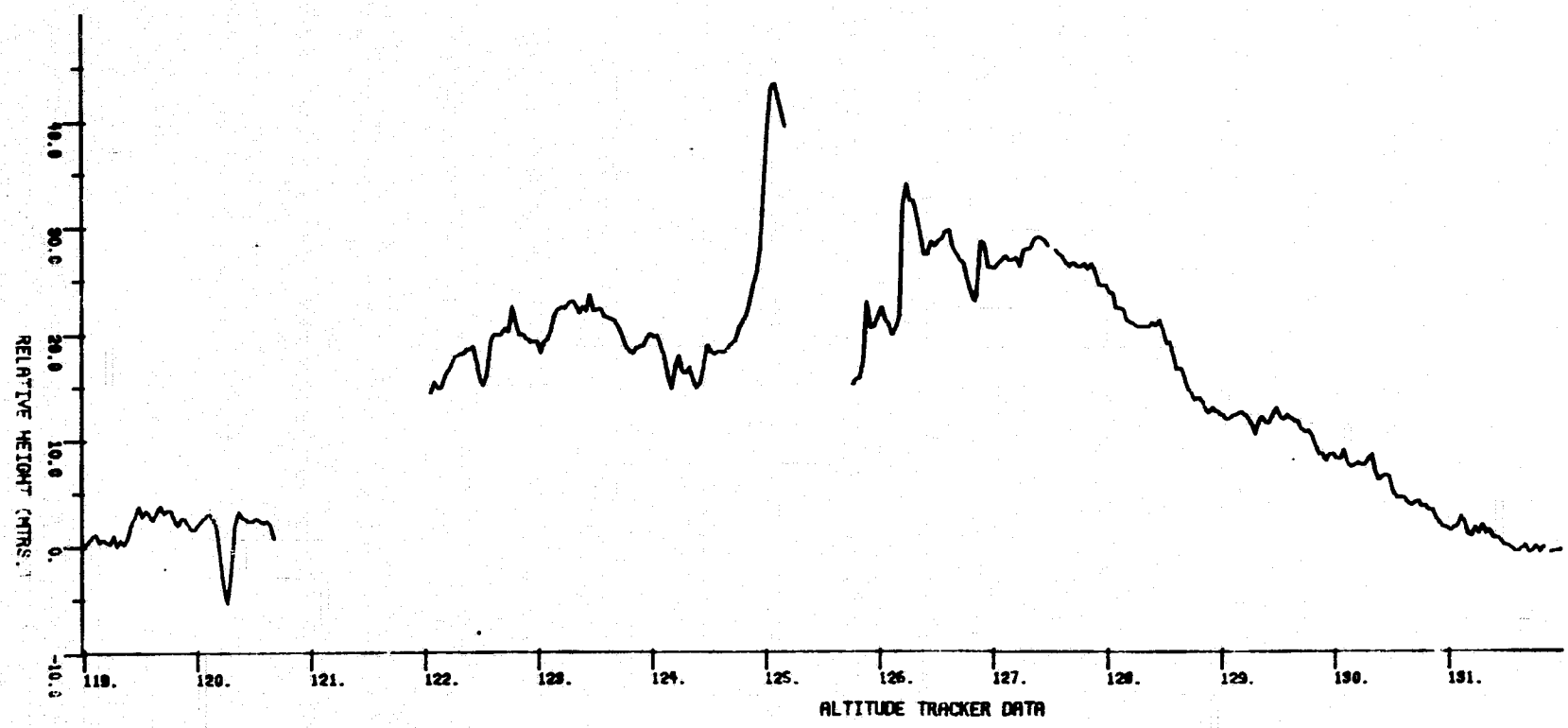

Figure 24. Altimeter profiles for Orbit 3268.

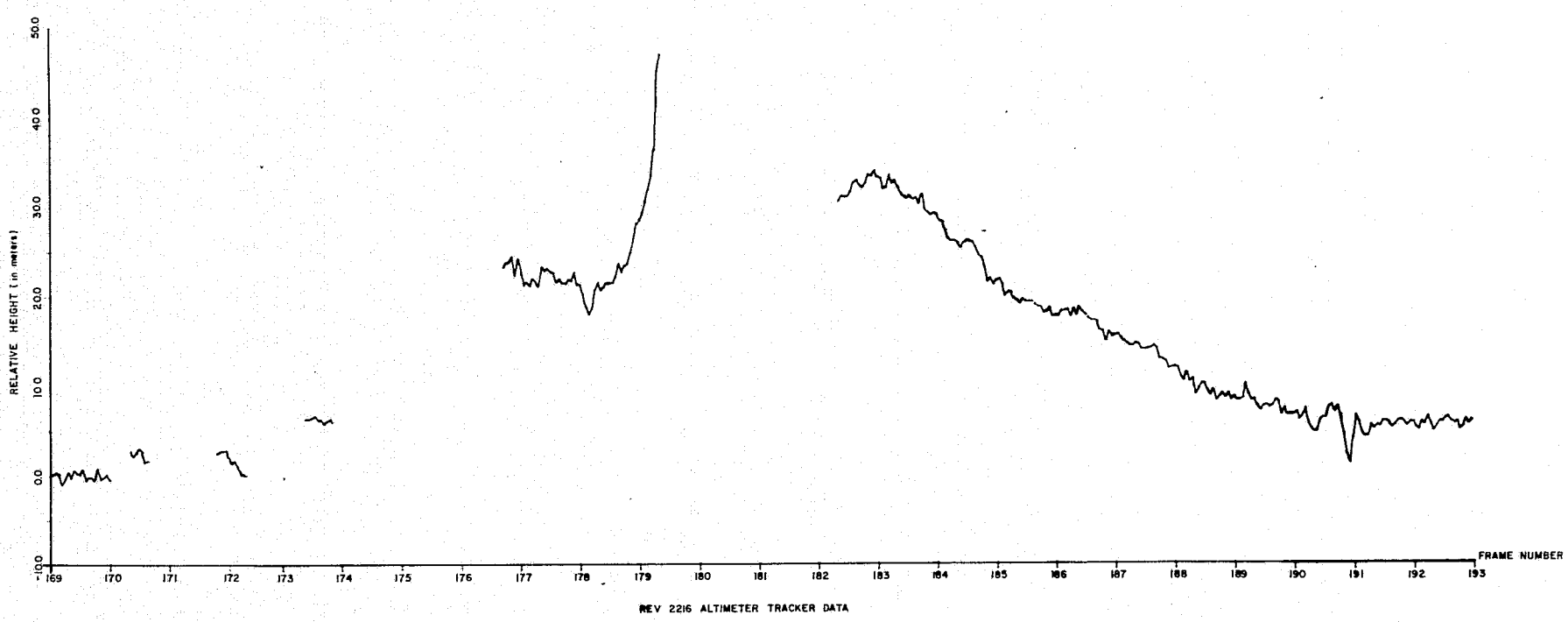

Figure 25. Altimeter profiles for Orbit 2216.

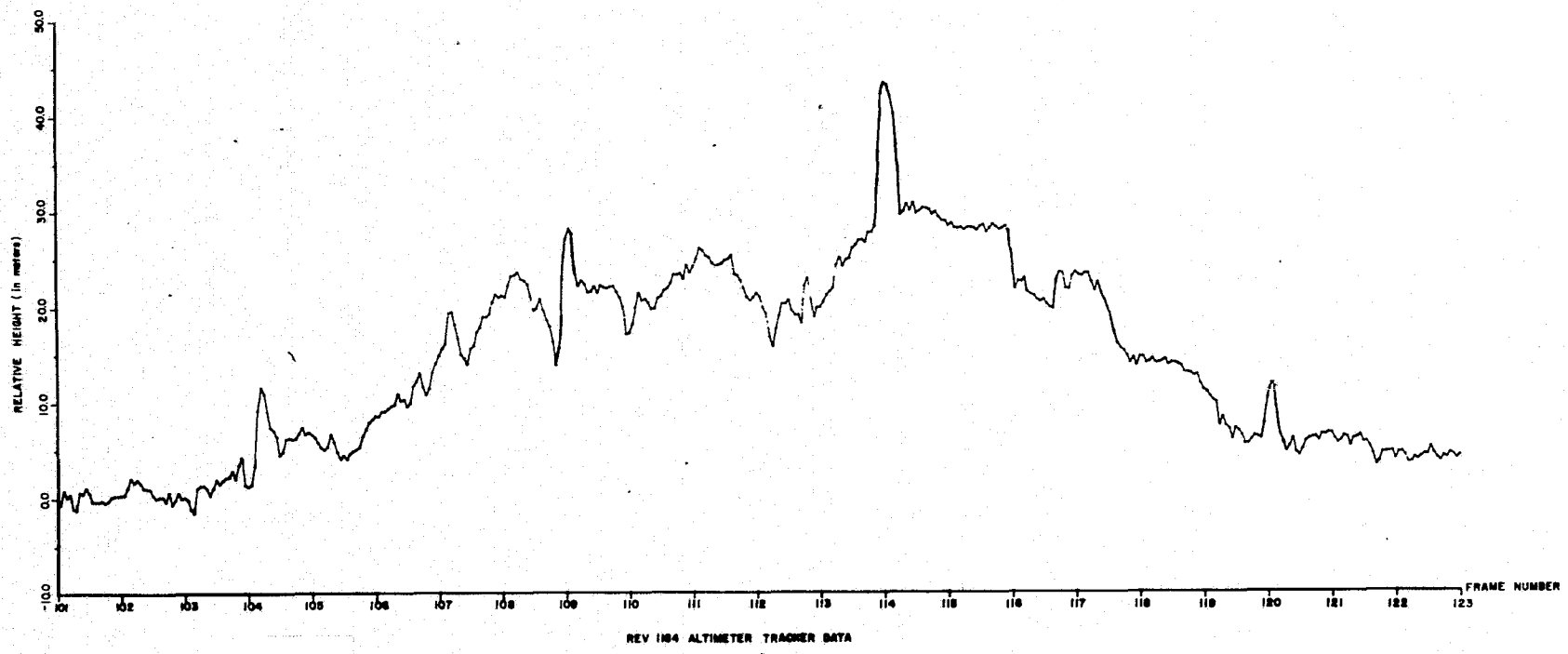

Figure 26. Altimeter profiles for Orbit 1164.

frame 102, there are sand flats off Cape Canaveral - the Cape land mass begins just after the start of frame 102 and is represented by the 2 meter or so rise in height at that point. The plot clearly shows the rise in height of the Florida Peninsula, with a relatively narrow peak height in the central Florida ridge visible at frame 114 of about 43 meters above sea level. This ground track goes off Florida in the Caloosahatchie River, between frames 119 and 121 - the increase in height at frame 120 is downtown Fort Meyers.

Deferring for the moment discussion of orbit 4846, Figures 27 and 28 show data for the south-north passes over Florida. These orbits were largely confined to the Everglades section, however, the intersection agreement with the above orbits is excellent. Data characteristics for orbit 4568 were discussed at length in section 1.4. Altimetric data for three other Central Florida passes have been studied; these are orbits 1491, 2017, and 3069 which are shown in Figures 29-31, respectively. Again, the intersection with orbit 2791 is in very good agreement. Note that each of these passes experiences loss-of-lock conditions in the vicinity of Orlando, Florida. This condition is thought to be due to the sharp changes in altitude associated with high-rise structures in the metropolitan area.

Orbit 4846, being a high data-rate pass, has been highly analyzed relative to other Florida data. The previously discussed Figures 4 and 5 consider data from this orbit. Figure 4 displayed the GEOS-3 on-board tracker profile data with annotated geographic features. Note that creeks and rivers tend to show up as local depressions, lakes as flat regions, and cities as irregular elevated regions. The visibility of water areas is attributable to the higher fresnel reflection coefficient. Figure 32 is a graph of altimeter tracker data and spatially averaged ground-truth values. It should be mentioned that, prior to these results, the radar altimeter was considered

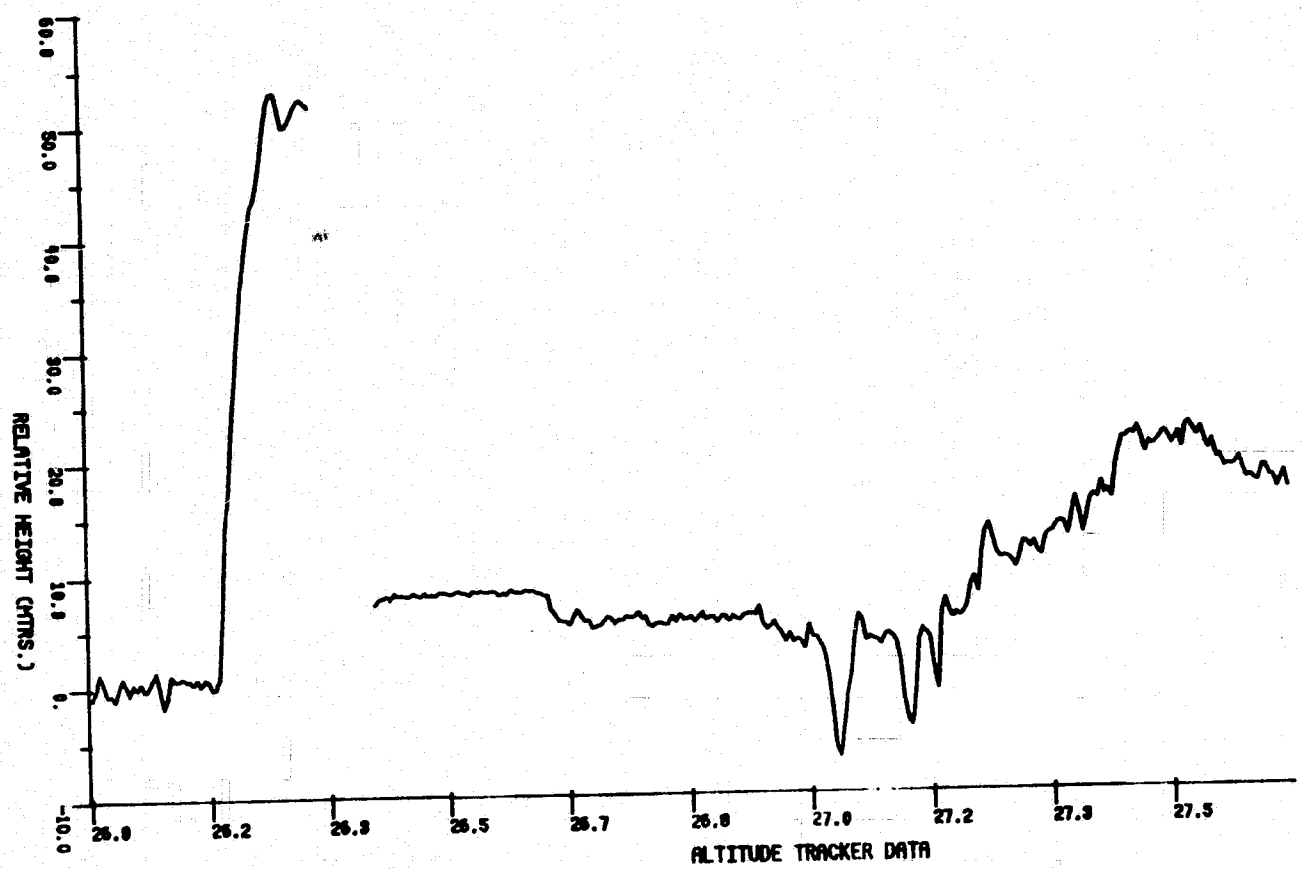

Figure 27. Altitude profile for Orbit 4568.

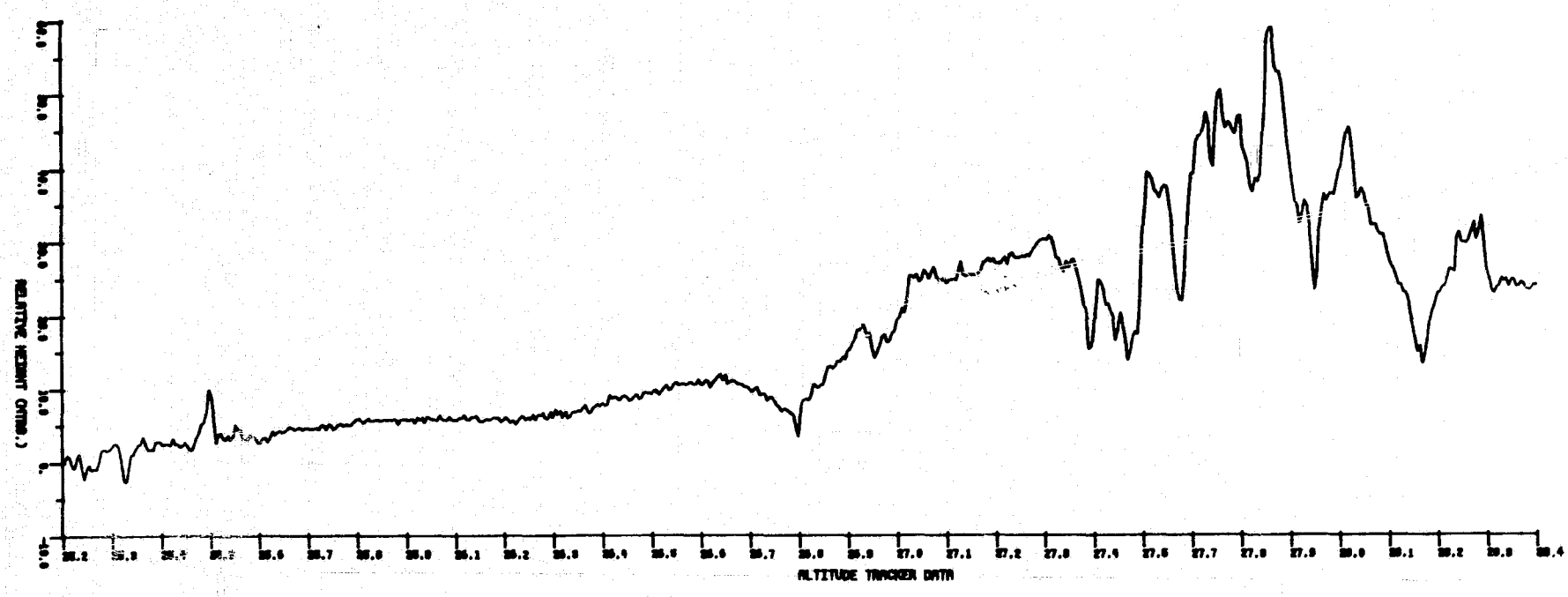

Figure 28. Altitude profile for Orbit 2791.

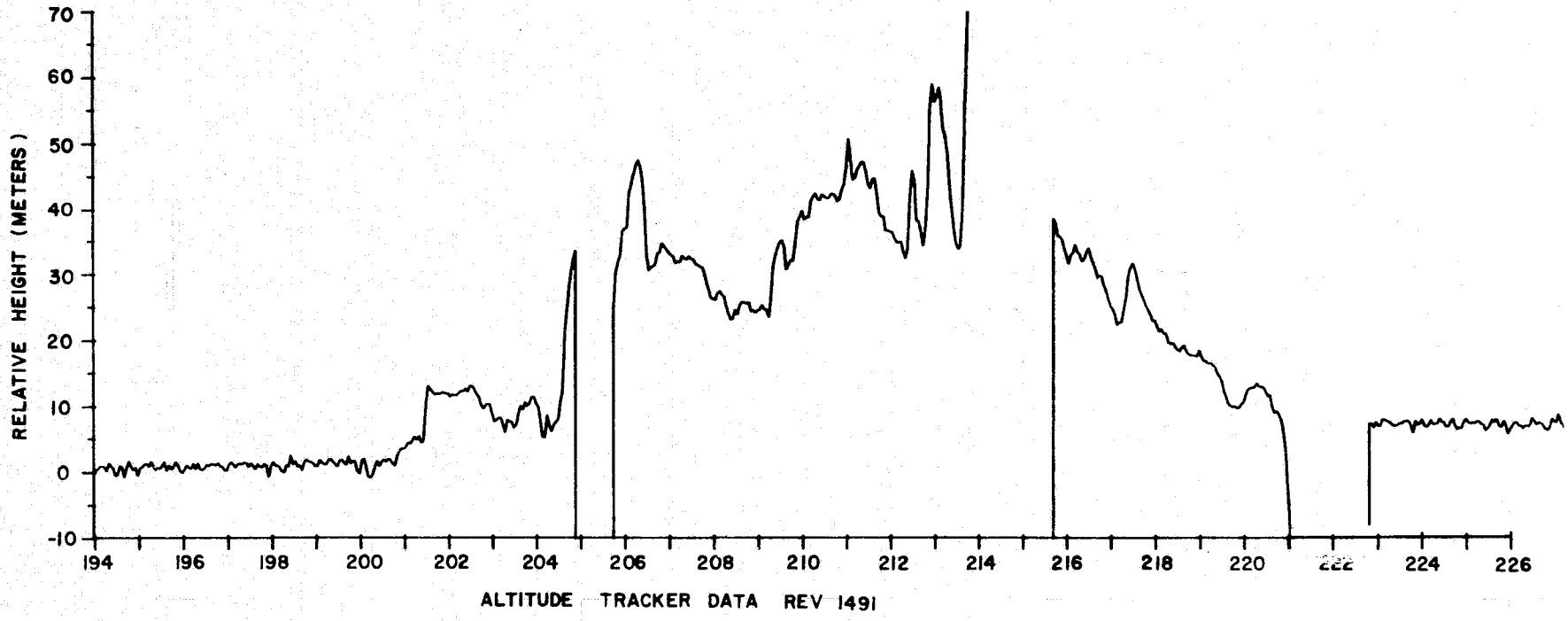

Figure 29. Altitude profile for Orbit 1491.

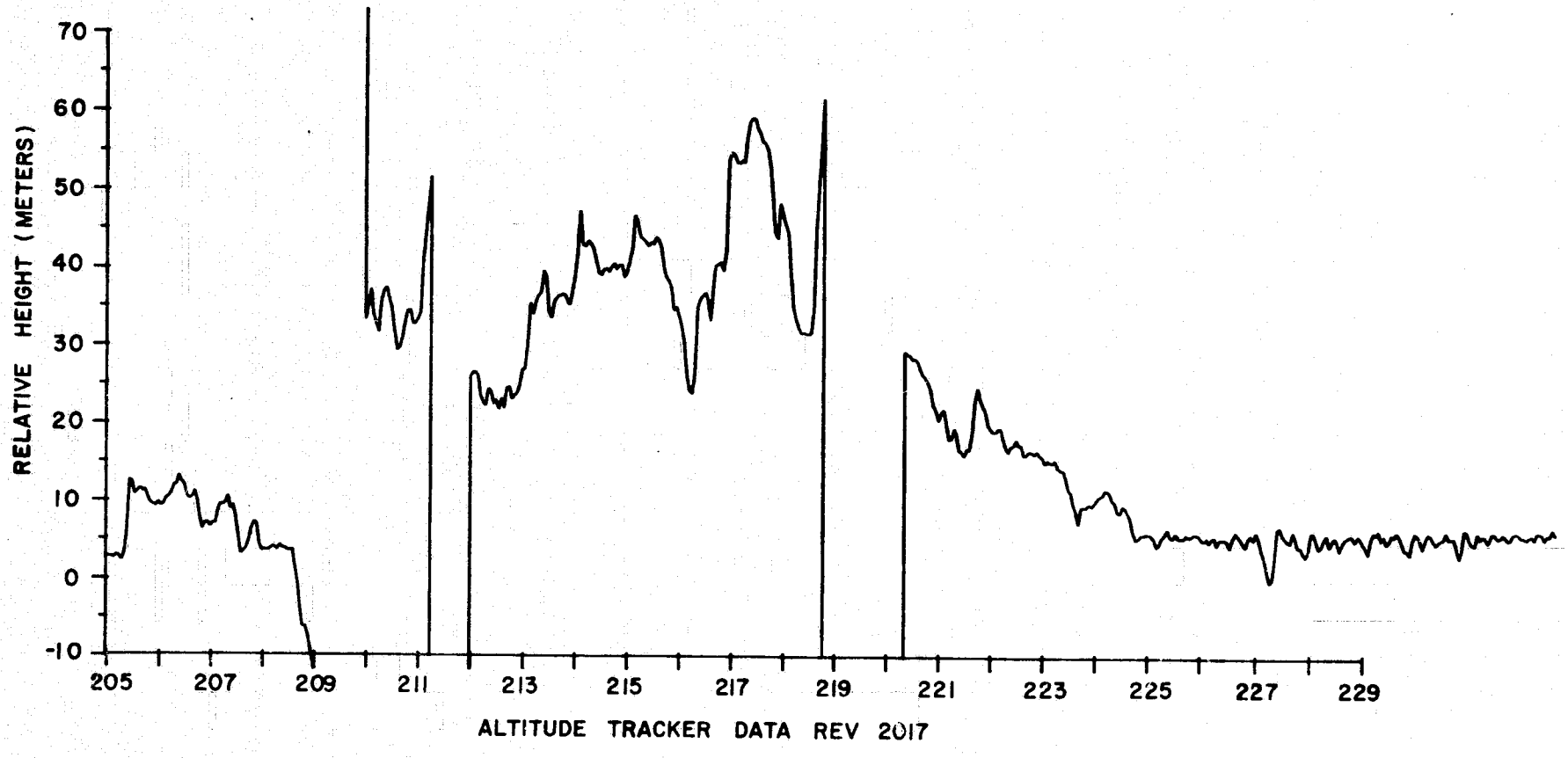

Figure 30. Altitude profile for Orbit 2017.

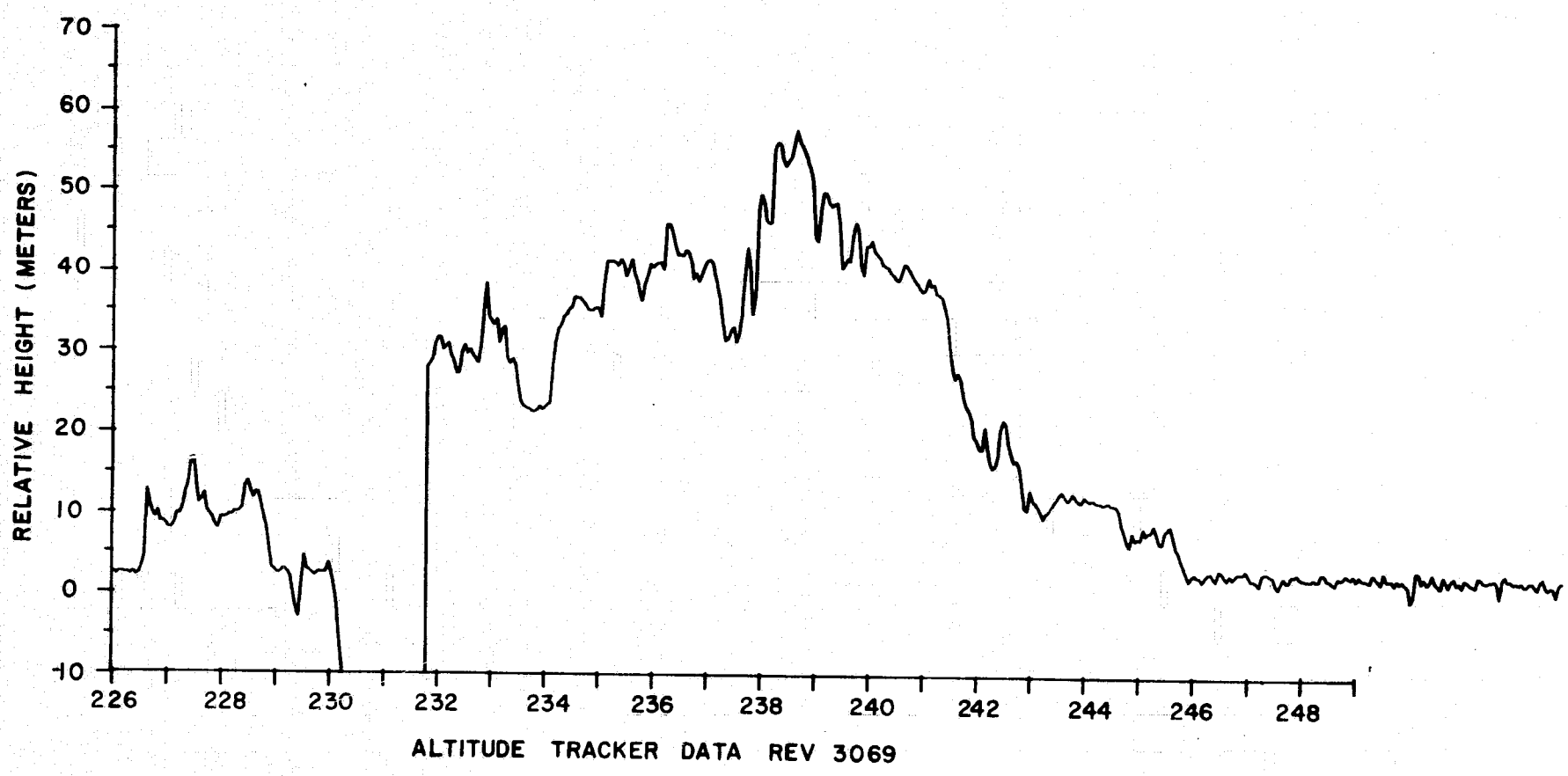

Figure 31. Altitude profile for Orbit 3069.

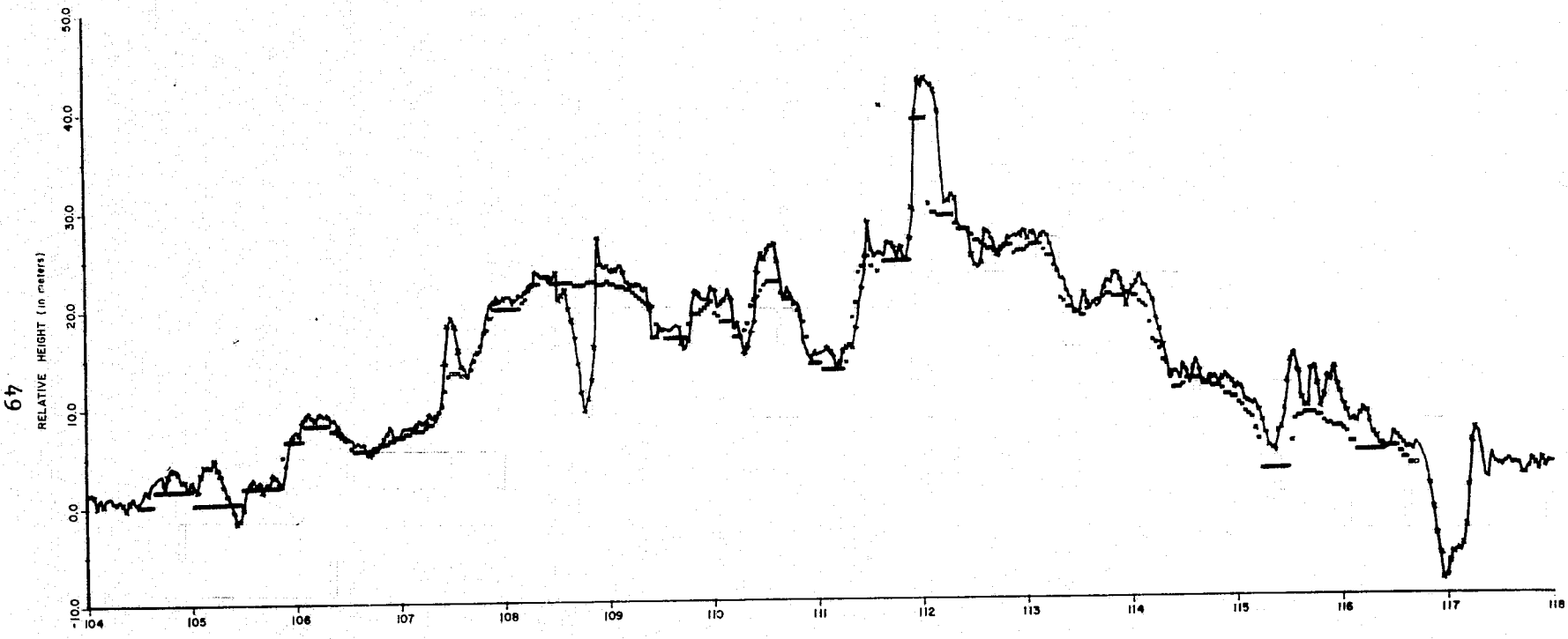

Figure 32. Rev 4846 Altimeter Tracker (Solid Line) and 3 km Diameter Ground-Truth (Symbols).

to "see" signals from a circular "spot-size" of "footprint" area equal to the spatial expanse of the 12.5 ns incident pulse length. According to this concept, the altimeter tracker should be following a surface representing the weighted average of the ground elevation. The term "weighted" is used since the contribution due to a given area depends on its relative radar reflectivity, its slope, and other factors.

Figure 33 reproduces three categories of ground-truth information; the upper trace shows the ~3 km spatial-average terrain data, the center graph shows the sub satellite or nadir values, and the lower graph depicts both the maximum and minimum ground truth values within the 3 km spot-size. Later paragraphs provide analytical measures of the correspondence between altimetric and ground truth data.

The previous paragraphs have alluded to the comparison of altimeter height and ground truth data. Use of waveform information available from high data rate passes provides the opportunity to construct other tracking strategies such as threshold or "first return" algorithms. Figure 34 reproduces one such concept; the solid line shows the on-board tracker data and the "x" symbols show threshold range-decisions. This threshold algorithm is structured to detect the closest point in the waveform at which the first reflected land feature occurs based on exceeding a pre-determined threshold value. A number of threshold values were attempted, based on quantization values (~7 m.v.) and the AGC action; a value of 10 m.v. was found to be the best compromise. This point, or timing event, is then used to compute a time offset relative to normal ocean tracking. This offset is then converted into a distance and the altitude data compensated accordingly. To compensate for thermal noise or "false alarms" the algorithm required two consecutive threshold crossings at the same point prior to recognition of a "threshold

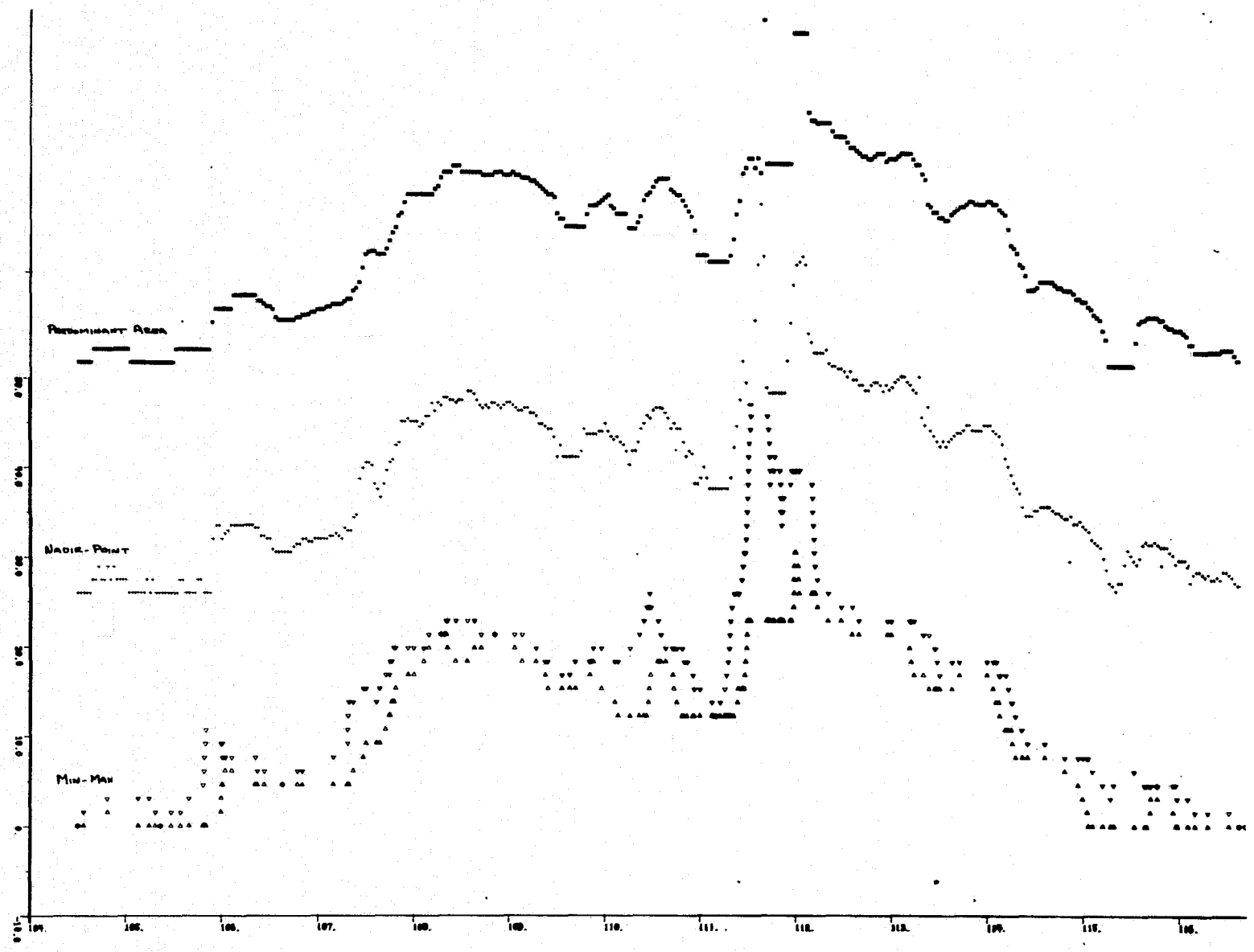

Figure 33. Comparison of Ground Truth methods for Rev 4846.

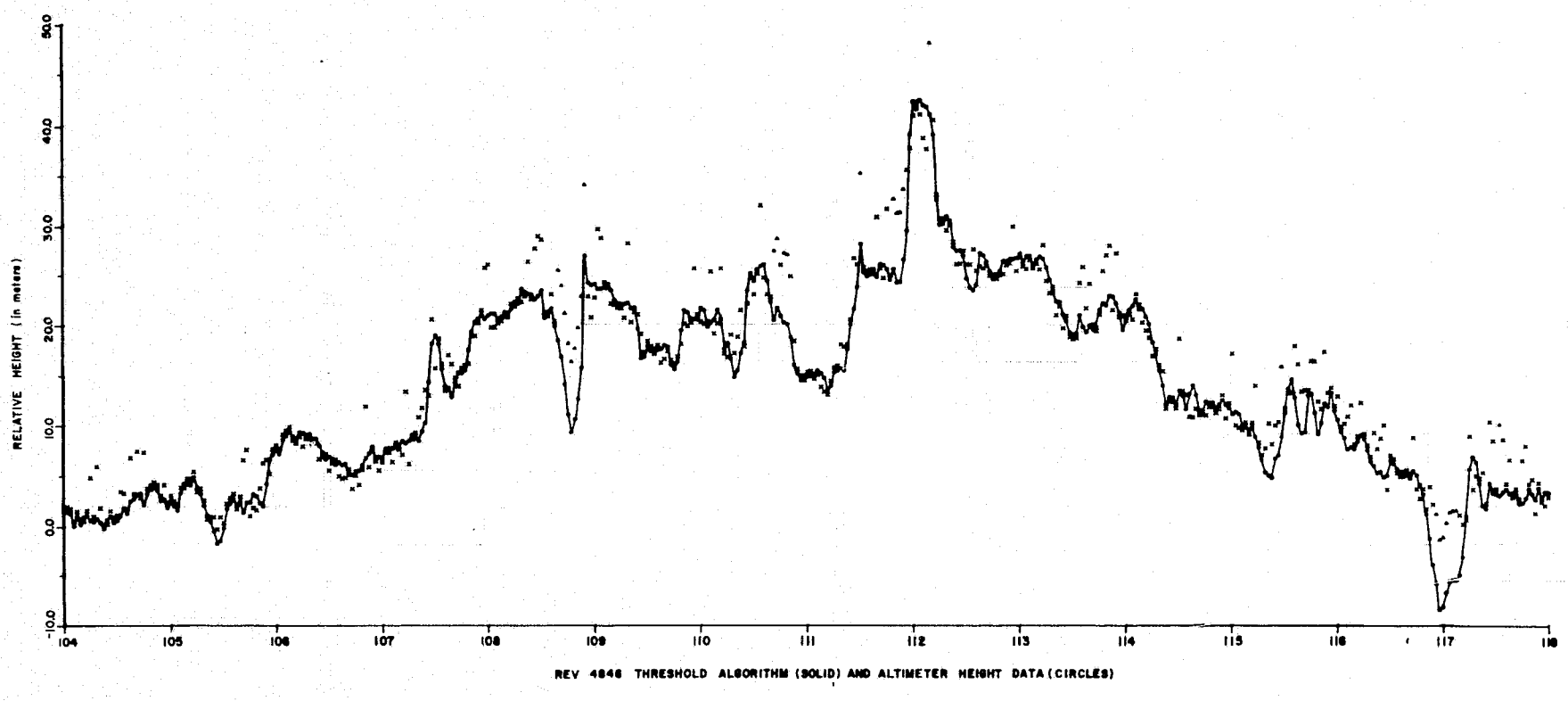

Figure 34. Comparison of threshold and tracker altitude profiles.

crossing". A Fortran algorithm was developed which accepts the per-frame 320 values and outputs either 32 or 180 threshold decisions per frame.

It should be noted that the 10 m.v. level is relative to normalization provided by the AGC system. If it were possible to disable the AGC system, a preferable method would be to set the threshold level relative to receiver-thermal noise.

Going back to the altimeter tracker-produced profile for orbit 4846, attempts were made to correct that height data so that it would correspond more closely to the profile along the nadir. The basic philosophy here was that returns from the nadir point would appear as the earliest returns, so that if a given return pulse waveform showed a signal level too large to be noise occurring in advance of the portion of the return signal being tracked, then that early rise would be declared the point of highest elevation and the altimeter tracker height measurement at that point would be corrected accordingly. Figure 34 shows the height data for 4846 as the altimeter produced it, and as it looked when corrected with the "threshold" algorithm. Figure 35 shows how this algorithm compares with the "along nadir" ground-truth data. The uncorrected altimeter data was shown compared to the "predominant height" ground truth data in Figure 32.

It can be seen from these that, except for anomalous tracking regions, the altimeter data (uncorrected) tends to fairly accurately reproduce (the RMS difference for this pass is less than ± 3 meters) the "predominant height" topographic data. The thresholding algorithm helps in estimating maximum heights within a footprint and, as a minimum, makes it possible to quickly identify places where anomalous tracking has occurred. It should be noted here that the reason that the corrections always produce greater heights than those the altimeter tracker "saw" is that the tracker tends to

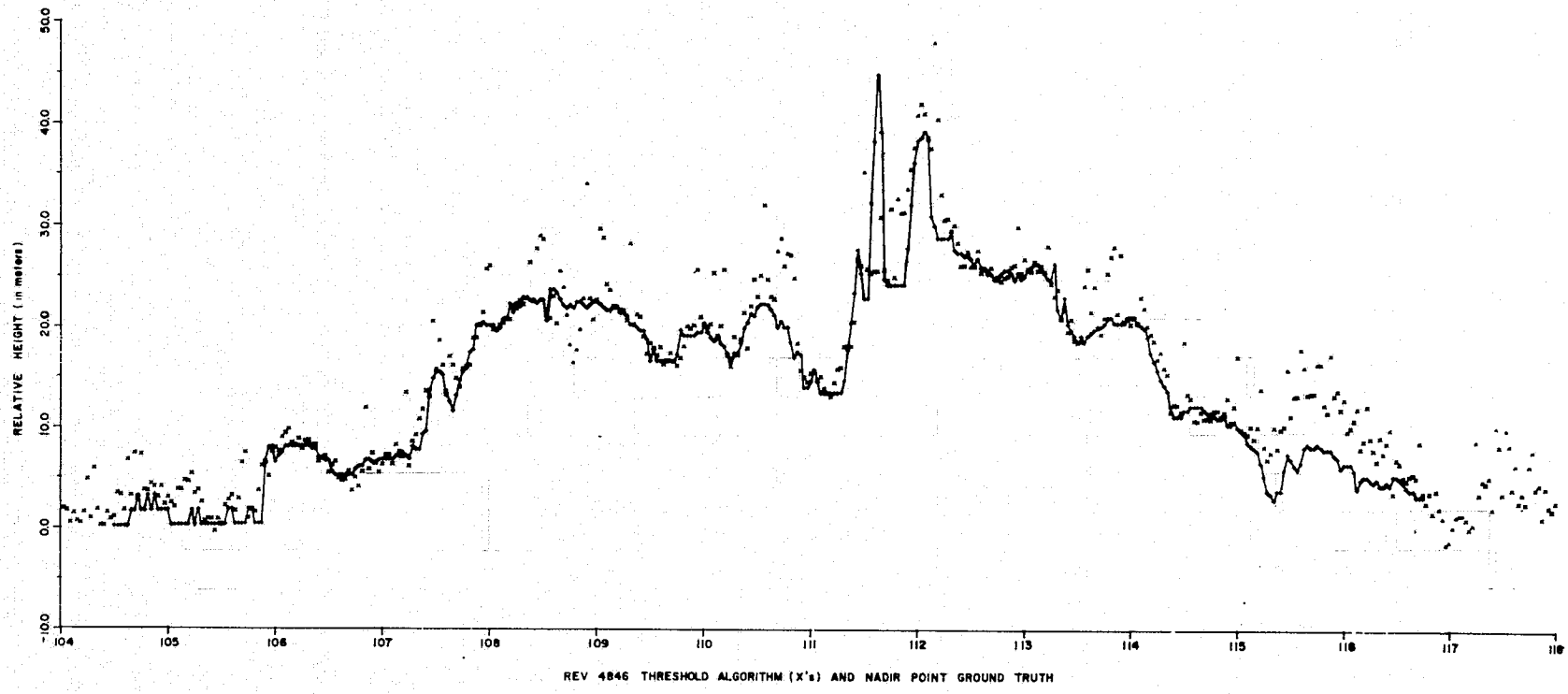

Figure 35. Comparison of threshold altitude values with ground truth data.

follow terrain surfaces due to its slow response time, while the algorithm picks up heights of returns from trees and man-made objects (buildings, etc.).

Referring back to Figure 32, the satellite measured surface profile is approximately midway between the map-derived upper and lower bounds, except for the period shown as frame 111 (one frame covers 3.2 seconds or a ground distance of ~21 km). Because of the apparent distortion in radar-sensed topography during this period, these values were selected for further study. Figure 36 shows the expanded data base pertaining to frame 111; in addition to map values and satellite data, this figure shows 50/second altitude data obtained from a digitally processed threshold tracker and average terrain values computed for 16 points along the ground track. The threshold algorithm used again requires a decision agreement between two neighboring per-pulse waveshapes and contains a threshold level equal to 10 percent of the average plateau value of the waveform. The average topographic points shown were obtained by averaging surface contour data over a 3.4 km diameter for a grid spacing of 0.1 km. Figure 6 shows the hardware tracker contained in the GEOS-3 system to be closely following the 16 mean-terrain values shown; the rms residual between these points is 3.5 meters. This result indicates that the radar altimeter is responding to an effective ground area which is quite close to a 3 km spot size. The threshold values shown which significantly depart from the average are thought to generally correspond to local, isolated targets such as man-made structures - note their increased occurrence as the ground track traverses the populous area near the right hand extreme of Figure 36 (this is within the city of Lake Placid, Florida). The threshold algorithm also indicates the possibility of profiling the "closest

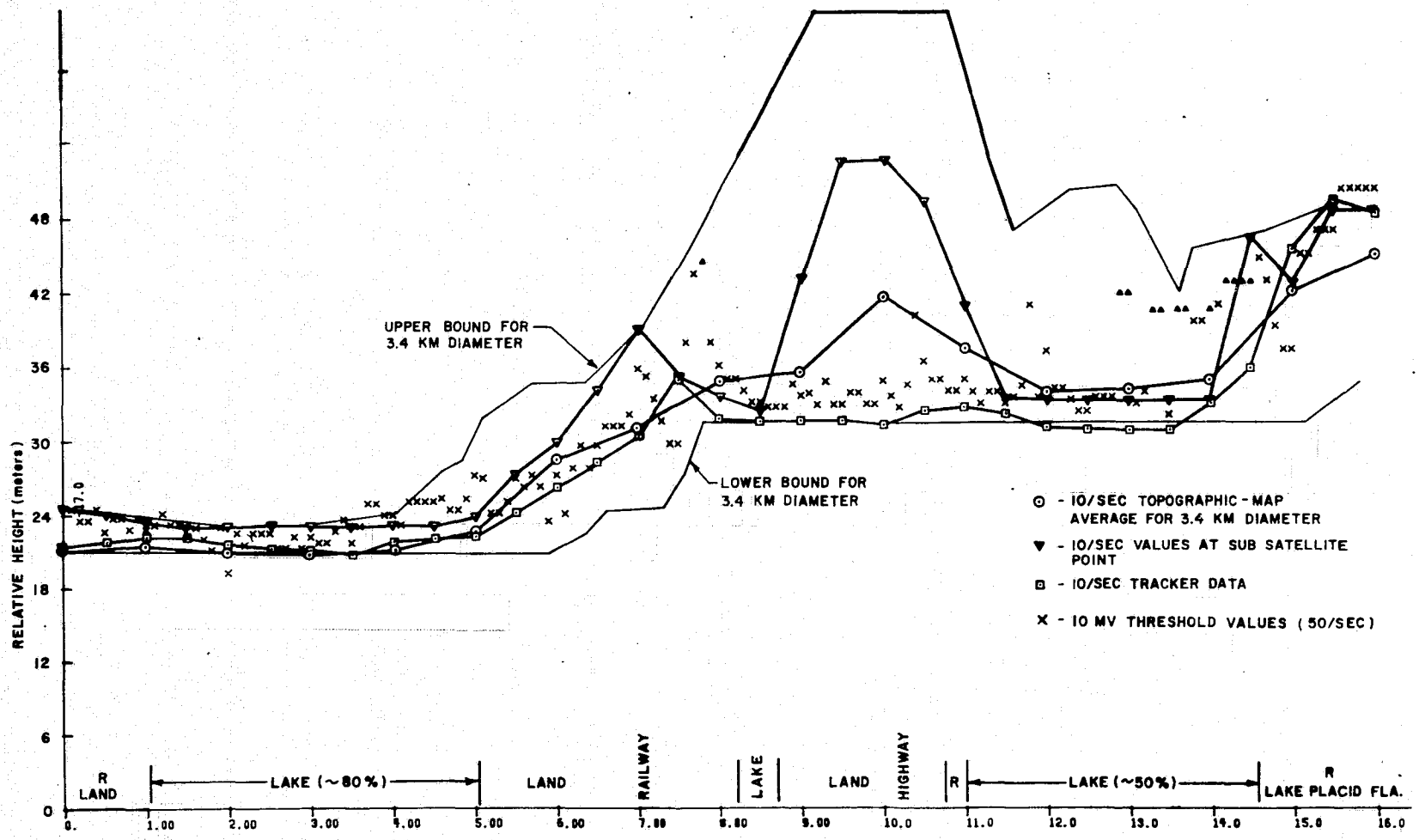

Figure 3.5. Details of GEOS-3 data for Frame 111.

Figure 36. Expanded view of Frame 111 of Orbit 4846.

return" or highest points, if additional sensitivity were available. (With the GEOS-3 system, the AGC cannot be disabled and large target areas will tend to suppress the return from small target areas.) Also note that the threshold values occasionally profile features which violate the spatial filter concept (e.g. response located at 7.8 on the horizontal axis of Figure 36). However, on a probabilistic basis these results indicate that the area-dependent scatter model is valid.

Figure 37 shows the land structure near index number 10 of Figure 36. This is a fairly complex area with a highway, lakes, and a dry-land range expanse of 75 ft. within a 3 km radius. This region is thought to present the roughest natural terrain of the entire orbit 4846 profile; as such it should show pulse-stretching in the waveform leading-edge. Figure 38 shows three waveforms; the rough terrain (Florida) waveform is for a ten-pulse average for the region shown in Figure 37, the smooth terrain (Florida) is for frame 110 of orbit 4846, and the South Carolina waveform is near the termination of orbit 4582. This South Carolina pass represents the roughest terrain category for which altimeter-track data is presently available (see Figures 2 and 3). These waveforms show the following: (1) The smooth terrain waveform is typical of the majority over-land waveshapes - later paragraphs will show similar results for a number of orbits, (2) the South Carolina data shows the expected stretched waveshape for an extended-rough target-area, and (3) the Florida rough terrain waveform appears to be the superposition of diffuse scatter and an isolated or point target situation. Considering the location of the GEOS-3 tracking gates, these waveforms argue strongly for threshold or contiguous gates in future systems.

Figures 39 and 40 show signal-fluctuation histograms for orbit 4846 during an over-ocean period and for several over-land frames. (Gate 10 was

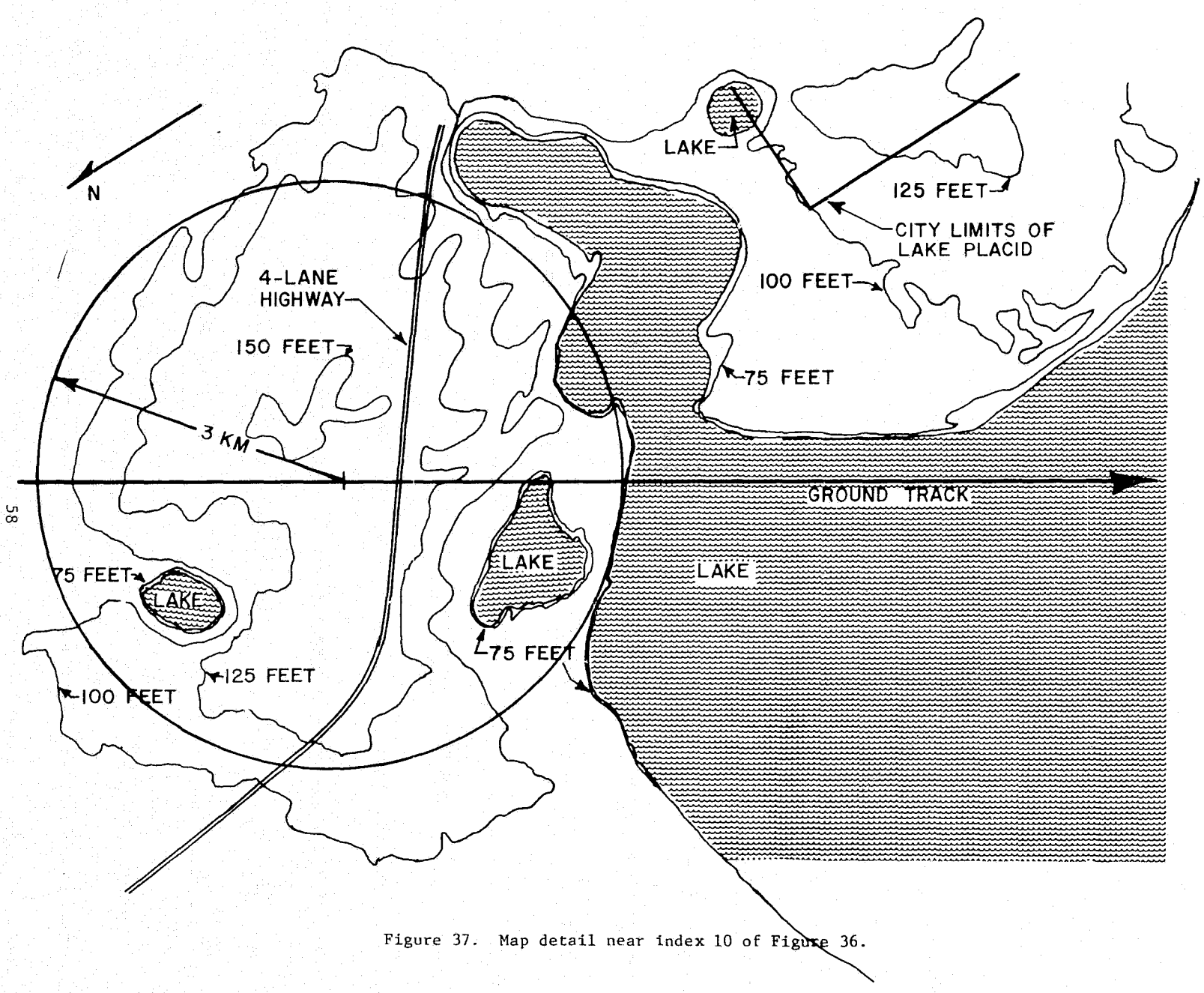

Figure 37. Map detail near index 10 of Figure 36.

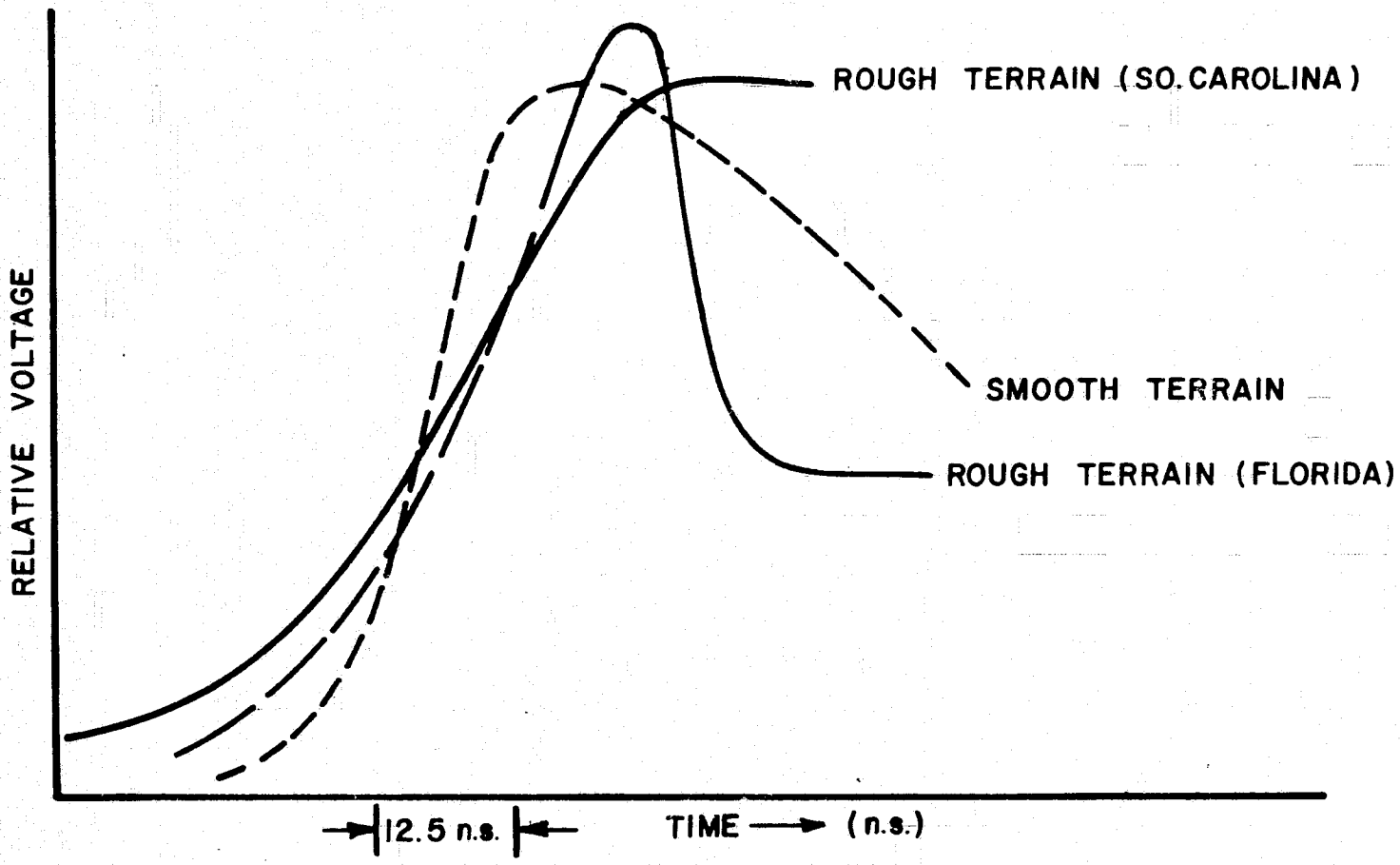

Figure 38. Waveform data for three terrain categories.

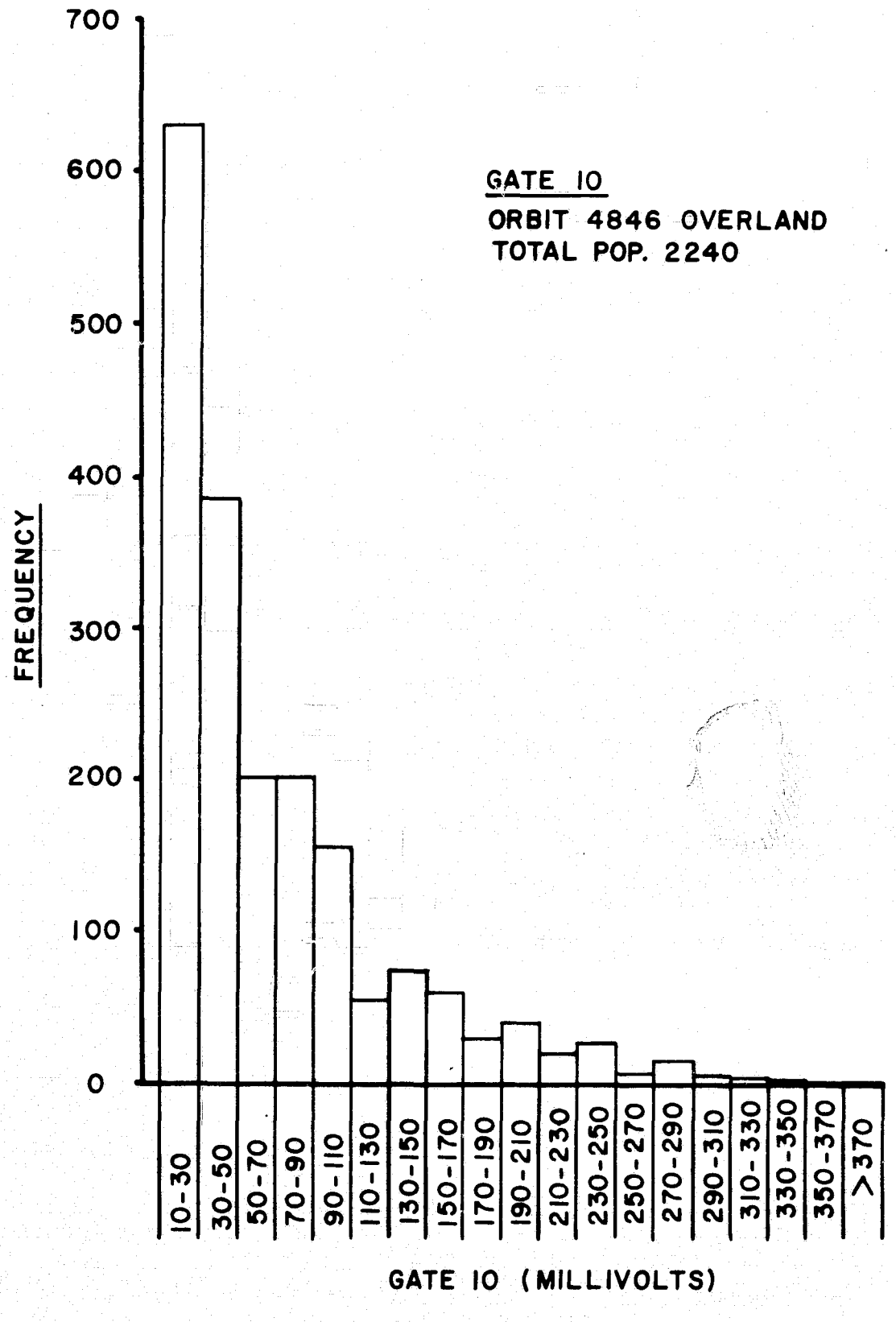

Figure 39. Histogram of the signal fluctuations over land.

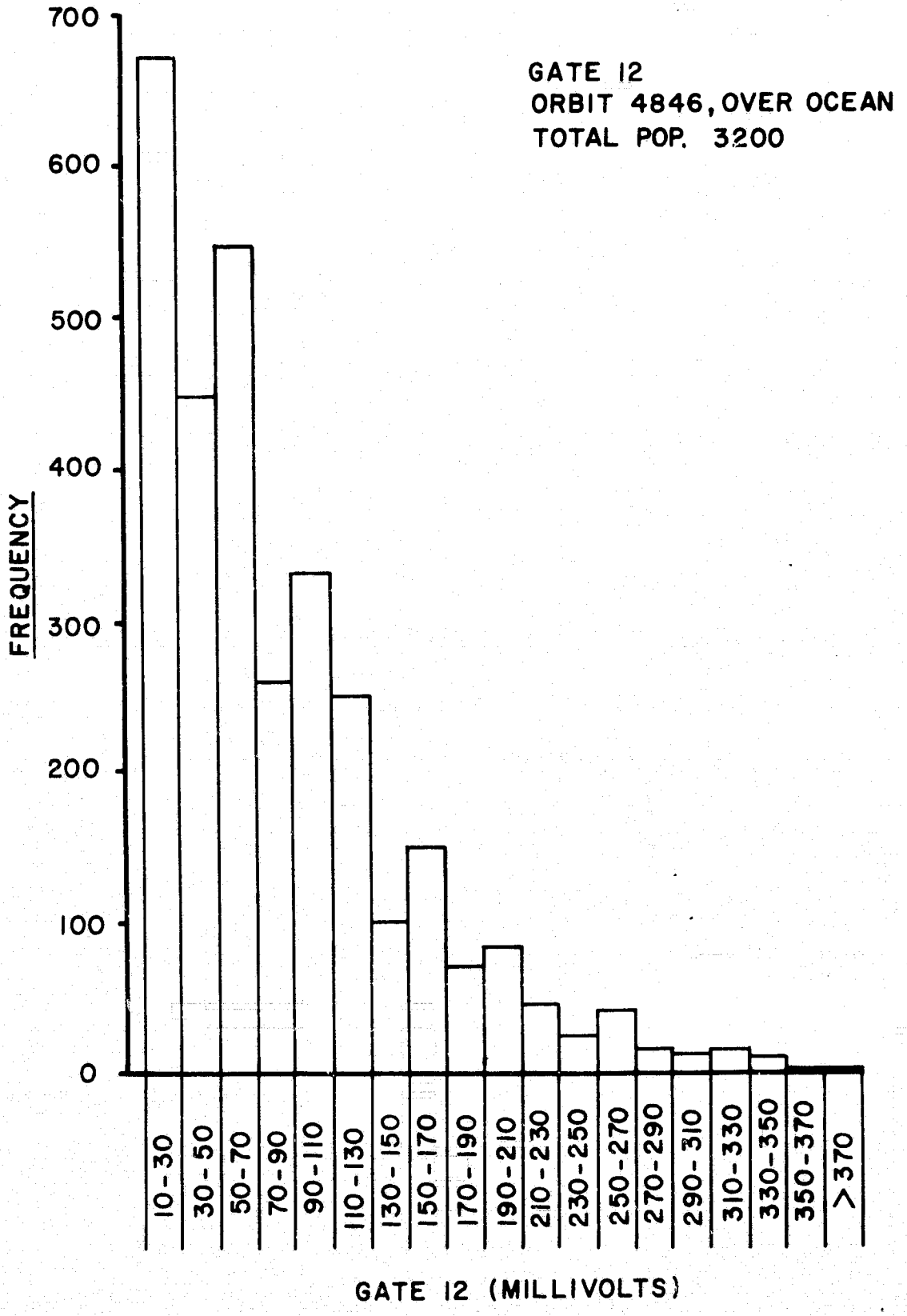

Figure 40. Histogram of the signal fluctuations over ocean.

used in the over-land case because of saturation effects present in gates 11-16.) These histograms show the ocean and land scattering mechanisms to be similar, for this terrain.

5.1 Analysis of Effective Spot-Size

Central to the subject of radar terrain profilometry, is the question of spatial resolution. For beamwidth-limited geometry and surfaces for which σ° angular effects are ignorable (such as over-ocean), to first order the spatial resolution is fixed by the antenna beamwidth. Over surfaces for which pulse-length limited operation is dominant, it is possible to define an effective spatial filter function with some rigor [8]. For backscattering regimes not clearly in either category it is possible to statistically define the spatial resolution. For this situation, the term "effective spot-size" has been widely used; although care must be exercised in use of such a concept since a high degree of surface homogeneity is implied.

This section describes the analyses of effective spot size carried out under this study, for areas consisting mainly of natural terrain. Two approaches were used: The first consisted of the arduous task of spatially averaging the surface-truth data over varying areas and then calculating the degree of correlation between the altimeter data and the surface truth data. The second approach comprised a filter analysis of the subsatellite ground truth data. The analytical methods and results are detailed below.

(1) In the first approach, the topographic data were gridded using cell dimension of ~0.1 km; average elevation data was then computed as a function of radius. That is, a 2-dimensional averaging was performed over circular ground intercepts. The data base extended over one I-Mode frame

(~ 3.2 sec.) and height versus diameter values were computed at 32 points within the frame. Diameters of 0, 0.5, 1.0, 2.0, 3.0, and 6.0 km were used. The degree of correlation between the altimeter data and the topographic-map averages for each diameter was then computed as follows: The cross-covariance C_{xy} was computed

$$C_{xy} = R_{xy} - m_x m_y$$

in which m is the mean and R is the zero-lag cross correlation R(0)

$$R_{xy}(k) = \frac{1}{N} \sum_{n=0}^{N-1} x(n)y(n-k)$$

with x(n) the altimeter data and y(n) the topographic data for a fixed diameter.

The cross-covariance (normalized by C_{xx}) resulting from these computations are shown in Figures 8 and 41. Figure 41 shows the covariance maximum to occur for a diameter of 2 km. One difficulty experienced in this analysis was that the Florida topographic data did not decorrelate rapidly with ground track displacement. Based on Figure 41, it is concluded that the altimeter is responding to an illuminated zone < 3 km for the Florida data. This comparatively small (relative to the system response) is attributed to σ° decay versus off-nadir angle.

(2) As a second approach to the spot-size question, the following

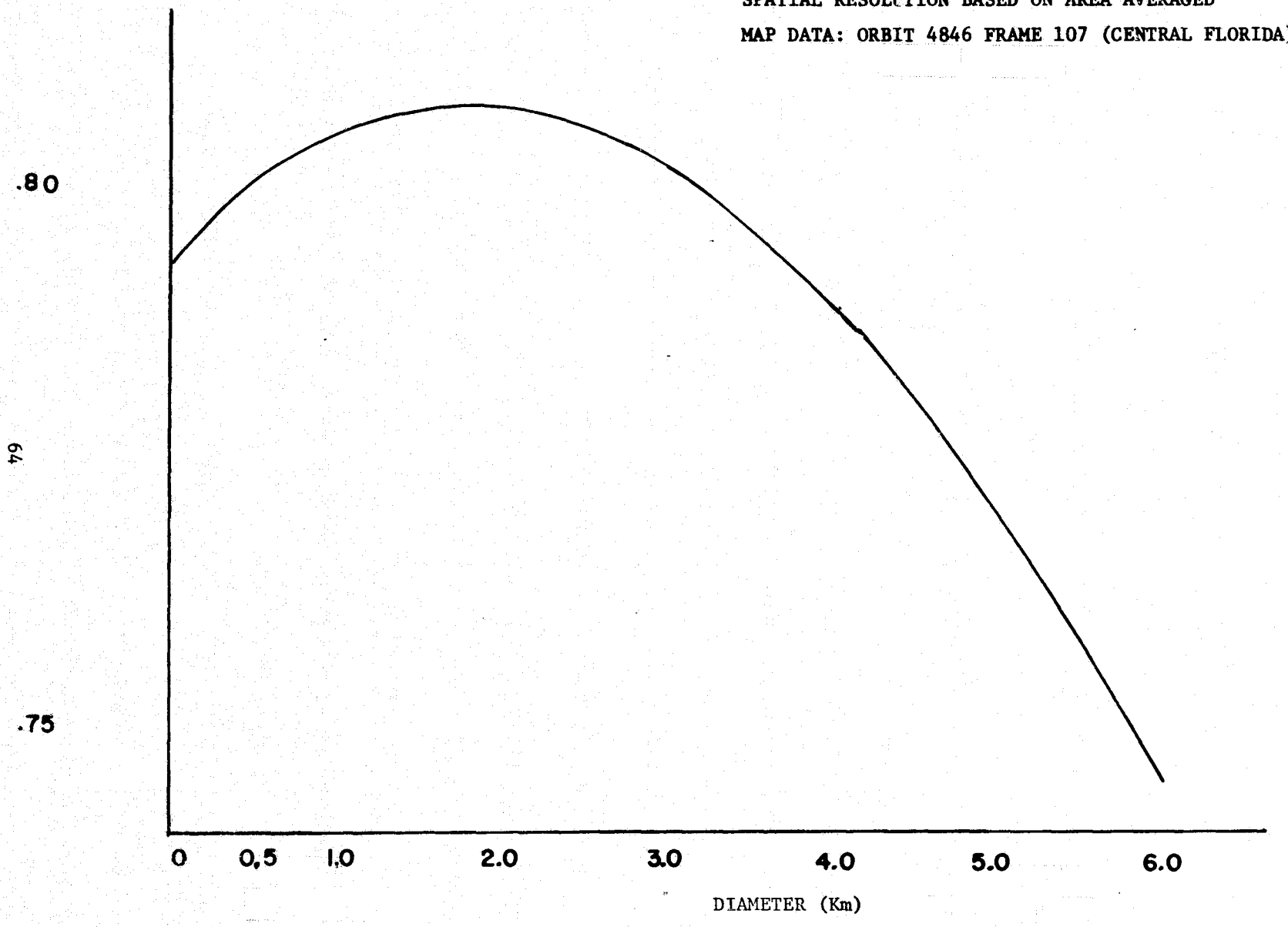

Figure 41. Degree of correlation between split-gate data and spatially averaged map data.

analysis was carried out. A dense set of topography values were read off the maps and linearly interpolated to 1 ft. height increments. Frame 107 of orbit 4846 was used in this case. These data, which represented densely spaced subsatellite values of terrain height, were digitally processed to yield power-spectral-density (PSD) and variance reduction formats. These data were then used to assess the effects of partitioning the rms roughness into two wavelength ranges; one range that represented the spatial filter effect for which roughness would be manifest in the waveform data, and a (long wavelength) case for which roughness should be mapped as altimetric height variations. The PSD was computed by performing a discrete-Fourier-Transform of the equally spaced height data followed by use of a rectangular window function of width 0.5 km [9]. The horizontal wavenumber scale of the PSD was then re-scaled as a frequency variable using an assumed ground track velocity of 6.5 km/sec. This scale will be used in a later discussion. The resulting PSD is shown in Figure 42. Note that presentation of the surface truth PSD in this format is, to within map resolution constraints, equivalue to the (time-series) spectrum that would obtain for a totally error free sensor. This computation shows variance of the Florida topographic data to largely reside in the frequency range

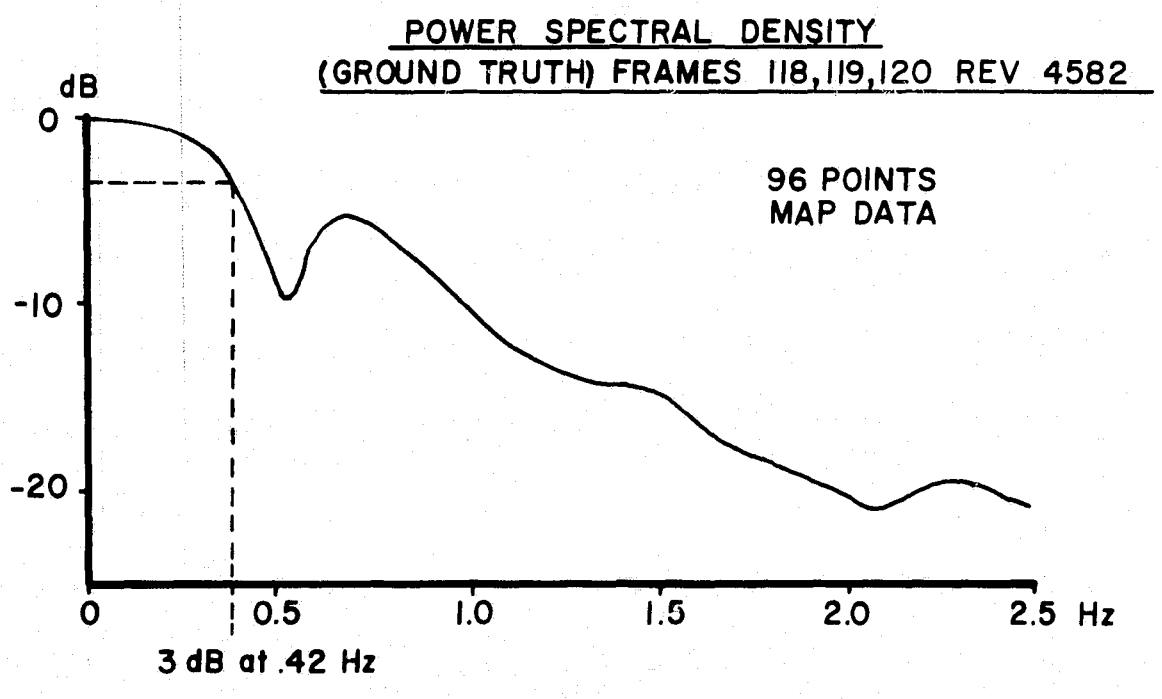

Figure 42. Power Spectral density computed based on map data for the idealized "exact" tracker.

below 1.0 Hz (or wavelength range above ~6 km). (The minimum wavelength for the data used in Figure 42 was .13 km; extrapolation to shorter wavelengths would yield results of questionable validity.) The variance, or area inside the PSD curve, was computed directly from the digitized, linearly-detrended data and found to be 3.9 meters^2. Mean-square slope was computed in a similar manner and found to be 2.1×10^{-4}. All of these statistics strongly suggest that the roughness characteristics of the Florida terrain are such that the altimeter was operating in a pulse-length limited mode (as qualitatively discussed in connection with Figure 2). Note that this variance translates into a comparable ocean roughness ($H_{1/3}$ value) of 7.8 meters ($4\sqrt{3.9}$). However, the major contributor to this process variance should appear in the altimeter rather than the waveform data. The following analysis was carried out to further elaborate this effect.

The above discussed subsatellite data was digitally filtered to approximate the behavior of an idealized altimeter with a variable spot size. The subsatellite height values were first filtered using a rectangular aperture function of width D; variance of the resulting process was then computed. These results are shown in Figure 43; this figure displays the per-cent variance reduction versus filter span. Waveform data for this time period was examined for roughness effects; the sample-size and

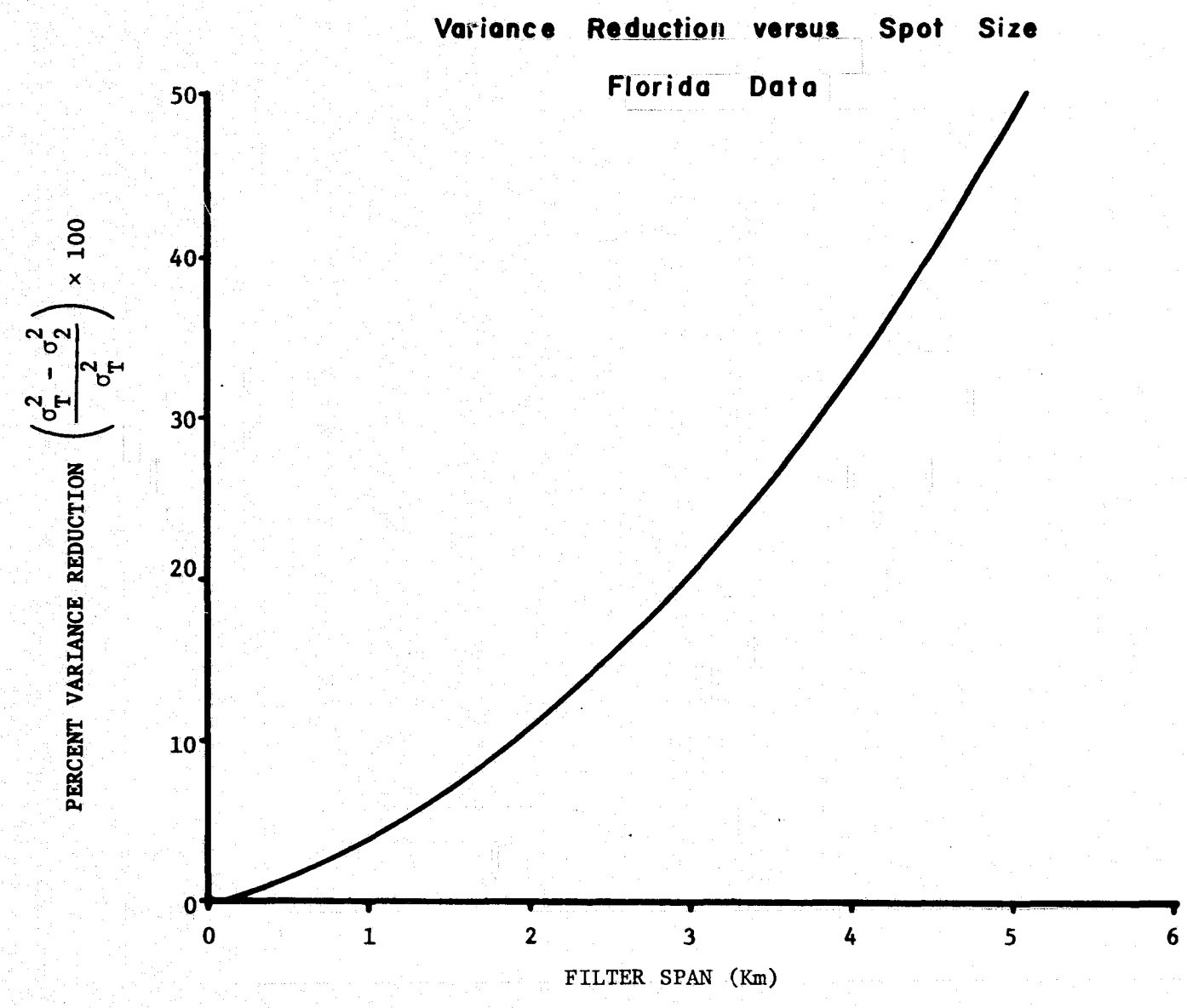

Figure 43. Variance reduction versus assumed spot size.

rise-time perturbation was such that the rms roughness was estimated to be < 0.8 m. with an 80% confidence factor. Assuming additive variances,

$$\sigma_T^2 = \sigma_1^2 + \sigma_2^2$$

where σ_T^2 = process variance

σ_1^2 = variance within spot-size

σ_2^2 = variance outside spot-size

the Figure 43 results may be used to provide the σ_1 estimates shown in Table I.

TABLE I

Spot Size Km	σ Waveform estimates rms roughness meters
1	.31
2	.79
3	.92
5.2	1.42
8.1	1.55

Examination of Table I shows the digitally filtered variance to correspond to a spot size of < 3 km. The waveform estimate variance (~ four times $H_{1/3}^2$) is in essential agreement with these computed values, which indicates that the waveform method of estimating local (or within

spot-size) roughness is a valid technique.

5.2 Split Gate Tracker Dynamics

Referring back to Figure 32, a comparison of the split gate tracker and map data shows a discrepancy in the location of the ridge in Central Florida (frame 112). The altimeter profiled ridge occurs ~0.25 sec. earlier than does the map data. The obvious possibilities for this difference are (1) the map data is in error, or (2) the split gate tracker contained a lag-type error while profiling this rather abrupt surface feature. The analyses given below and consideration of the threshold data argue that the latter effect is dominant and is largely a correctable error. Referring to the threshold data shown in Figure 35, the ridge is seen to be somewhat narrower in spatial extent than observed by the split gate tracker. The threshold data also shows a double peak to the ridge signature.

In order to investigate the split-gate tracker dynamics, the theoretical responses to step and ramp input signals were first computed based on the nominal tracker characteristics. Estimates of the tracker bandwidth for over-land operation were then obtained from orbit 4846 data and used to rescale the lag characteristics for the step and ramp input conditions.

Figure 44 shows the computed tracker response curves based on the convolution of the input signal with the system impulse response, as given in Figure 60 of [10] and discussed in [11]. This figure shows the assumed input signal as the dashed line immediately to the left of output or response curve (solid line). Note that the overshoot is ~20 per-cent for the step input and that the time lag is greatest for this input. As measured at the 50 per-cent point, the time-lag for the step response is 100 m.s. and for the ramp inputs shown varies from 80 to 50 m.s. This variability is to be

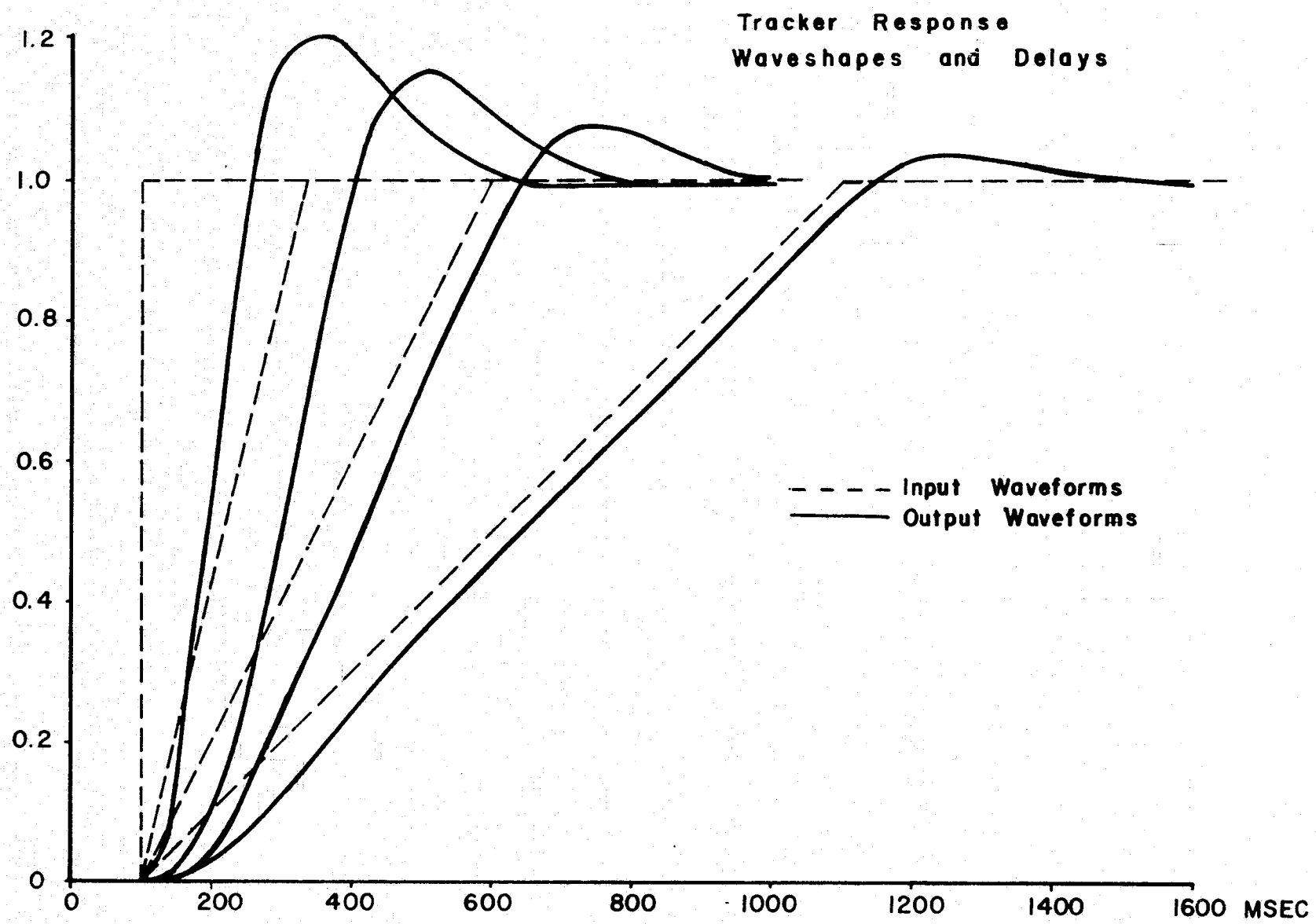

Figure 44. Computer tracker response to step and ramp inputs (tracker bandwidth ~ 5 Hz).

expected and is similar to the delay variability for monochromatic input signals previously reported [11] in connection with time-tagging considerations.

Power spectral densities were computed using two frames of the 10/sec. tracker data, for both the Florida (4846) and the South Carolina data (4582). Only two frames were used because surface homogeneity questions arose for larger data expanses. The Florida data, which is considered to be representative of comparatively smooth terrain regions, yielded a spectral bandwidth (at 3 dB) of ~1.6 Hz. The South Carolina, or moderate terrain, region showed a spectral bandwidth of ~1.0 Hz (Figure 45). These data suggest that the over-land mean-waveforms are modified such that the time-discriminator characteristics of the tracking loop are also altered;with a resultant change of ~4:1 in the loop bandwidth. There are two caveats to this discussion: The tracker may be operating in a non-linear range over part of these data, and surface spectral effects may be a sizeable effect in the computed spectra. The latter possibility was discussed in a previous section.

The time delay appropriate to this over-land data base may be estimated as follows: Using the previously discussed spot-size (~3 km) the .5 sec ramp period approximates the effect of spatially filtering an abrupt surface feature. For the nominal tracker bandwidth of 4 Hz, this ramp input results in a time lag of ~60 m.s. with a 4:1 change in effective tracker bandwidth, the time delay scales to ~240 m.s. This delay value is in general agreement with that shown in Figure 32.

5.3 Analysis of Tracker Bandwidth Over Land

The previous discussion contained an over land PSD result that warrants further consideration. If it is assumed that surface isotropy applies and

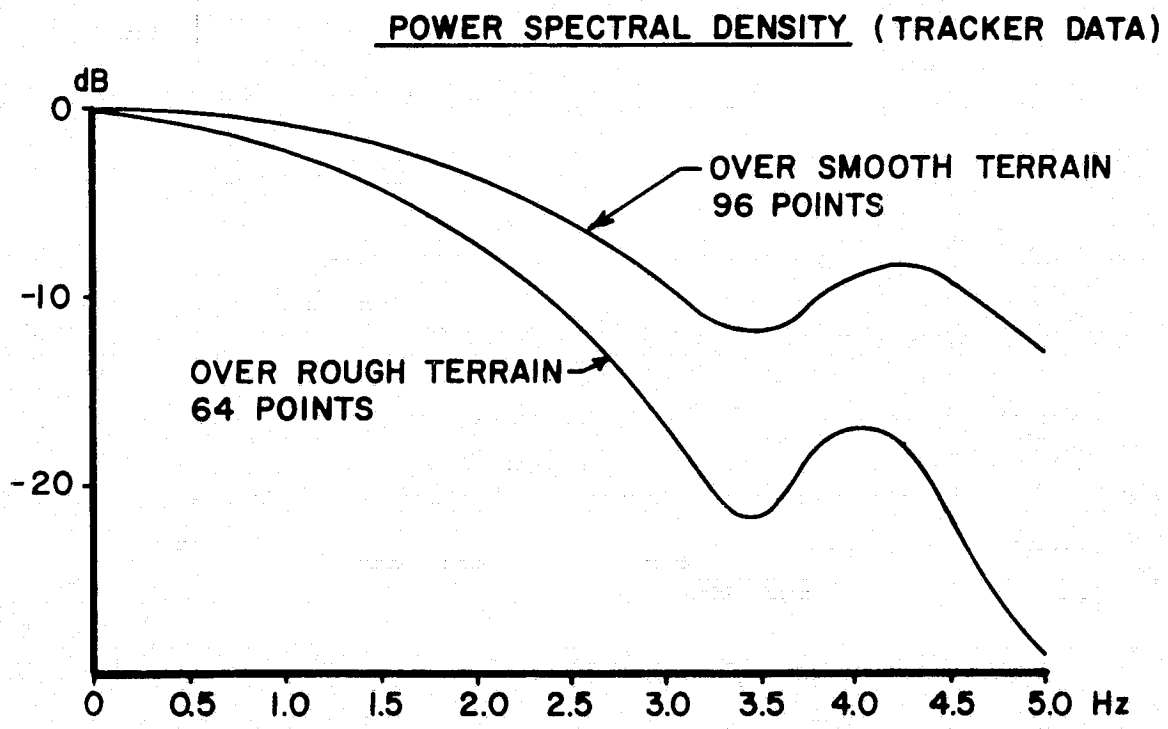

Figure 45. Power spectral density computed using 10/sec. tracker data.

Figure 46 represents a valid estimate of the input process, it should be possible to estimate the tracker bandwidth applicable to this terrain. Because of the tracking gate time-wise locations, the plateau decay noted in over-land waveforms, and the nature of the time-discriminator tracking loop [10], significant changes in tracker bandwidth would be expected in the over-land case.

Assuming the tracker to behave as essentially a linear-system, for an input or sensed PSD of $S_i(\cdot)$ and a tracker output PSD of $S_o(\cdot)$, the tracker transfer function $H(\cdot)$ should be in evidence as [9].

$$S_o(\cdot) = |H(\cdot)|^2 S_i(\cdot)$$

Computed values of the tracker-response PSD were shown in Figure 45 for two land cetegories, smooth (Florida) and moderately rough terrain (central South Carolina). In both cases surface homogeneity considerations limited the data base for these calculations to < 96 independent samples. This figure, when compared with Figure 42, shows the output bandwidth to exceed the input bandwidth. This implies that the tracker response function $H(\cdot)$ contains frequency domain overshoot, and is operating in a manner akin to a very small damping coefficient. Even so, the bandwidth is still considerably less than the over water case (~ 5 Hz). The 10/second altimeter data clearly shows this effect.

Before leaving the subject of surface statistics, it is of interest to examine these data in terms of correlation length. Figure 46 shows the computed autocorrelation functions for the geographic areas used in the PSD discussion. Note that the Florida data produces a correlation length (measured at the e^{-1} decay) of ~ 3.5 km. and the South Carolina data of ~ 0.7 km.

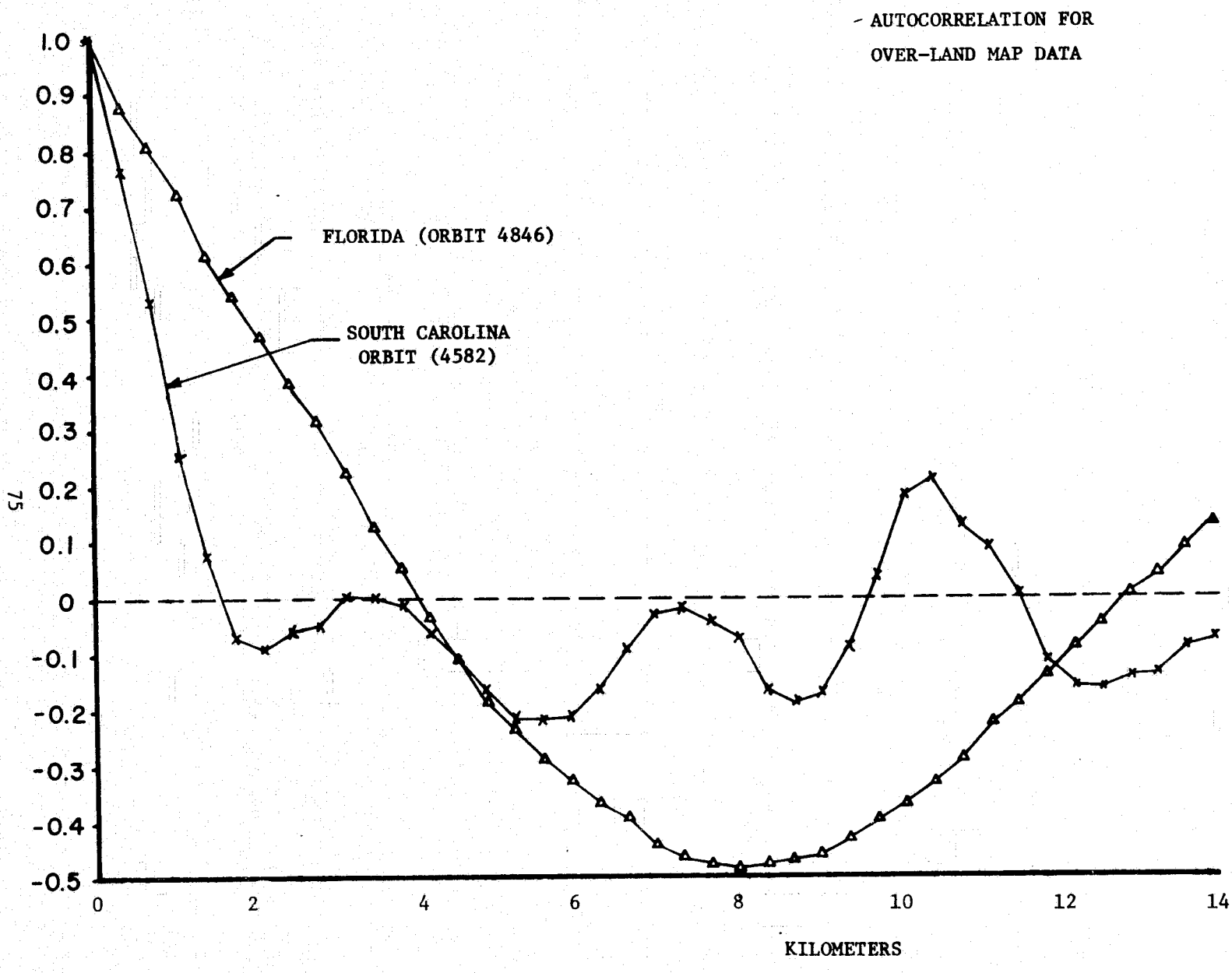

Figure 46. Surface-height autocorrelation function.

The South Carolina data indicates that there is considerable surface structure within the 3 km spot size. This result is also in evidence in the waveforms (c.f. Figure 38) and shows the system is operating in accordance with existing scattering models and the initial design objectives.

6.0 DETAILED BACKSCATTER RESULTS

Scattering coefficient, σ°, results are presented in this section which were measured during satellite passes over relatively smooth terrain regions. These data show backscatter for this terrain decreases dramatically with off-normal angle; a decrease of ~4 dB was observed at 0.25 degrees off-normal incidence. These measurements are considered to be unique in that a high degree of angular resolution and a comparatively large illuminated area are simultaneously available. Histograms of the per-pulse signal fluctuations show the signals to essentially behave as a Rayleigh fading target, similar to ocean scattering. The absolute σ° values obtained are typically in the neighborhood of 20 dB for land backscatter. A comparison of the angular dependence of over-land and over-ocean backscatter with σ° magnitude, infers a much lower Fresnel reflection coefficient for land backscatter. The over land (smooth terrain) results indicate that for pulse-length limited illumination, the effective illuminated zone will be dominated by the σ° angular dependence rather than pulse length, for system pulse lengths of $\geq$ 60 ns at typical satellite altitudes.

The GEOS-3 sensor operates at 13.9 GHz with pulse lengths of 12.5 and 200 ns and an antenna beamwidth of 2.25 degrees [10]. In the measurements reported here, the time-response of the 12.5 ns pulse is translated into an

angular dependency.* The area illuminated per pulse period is $\pi hc\tau$ where h is the satellite altitude, c the velocity and propagation and τ the pulse length [12]. For the 12.5 ns pulse length the area is $\sim 10\ km^2$. A similar measurement from Skylab, over the Bonneville Salt Flats has been reported [3]; these data showed the received waveshape to approximate the transmitted pulse similar to the results shown in Figure 12. Such behavior indicates specular scattering, however, the pulse-to-pulse variations imply scattering from more than one area.

The GEOS-3 system provides 16 samples of each received pulse with a sample spacing of 6.25 ns, and average values of the waveshape by a 20 ns AGC gate and a 200 ns gate. These averaging gates are displaced ~ 60 and 800 ns from the nadir return. The sampling functions are positioned by a split-gate altitude tracker [10].

Figure 10 gave results for a typical received waveform; the dashed section of the graph represents the relatively long period between the last two sampling events. The waveform data was derived as follows:

1. Pulse-by-pulse records and altitude tracker error signals were examined to determine data frames (320 pulses) which were free of altitude tracker disturbances. For example, two of the nine available data-frames over the Florida peninsula were rejected.
2. The remaining data was then corrected based on pre-launch calibration data. Additionally, gate values were compensated for saturation effects using the procedure

---

*All σ° values given in this report were derived based on "clean-signal" AGC calibrations. Use of the "clutter-signal" results in a reduction of σ° in the neighborhood of 3 dB.

given in [3]. Saturation effects are present in the over-land data because of the time separation between the early sampling events and the AGC gate (see Figure 47).

3. Corrections were then applied to compensate for antenna pattern and attitude angle. Antenna pattern corrections were on the order of 3.5 dB at the one-degree point. Attitude estimates were obtained during the over-ocean period just before land data acquisition; the largest off-nadir angle encountered was ~.6 degrees which required a correction of ~1 dB. The attitude angle estimation procedure is discussed in [13].

Figure 9 showed the over-land σ° versus angle which has been reduced thus far. Orbits 1164 and 4846 provided data over central Florida from Cape Kennedy to Ft. Myers; the ground tracks were displaced ~4 km from each other. Acceptable over-land data was available from orbit 2762 for the Virginia-Maryland Eastern Shore in the vicinity of Pocomoke City, MD; and for a brief period (2 Frames) near Ontario, Canada. Similar results have been obtained over Yucutan, however, a complete data-base is not yet available for this region. One pass over ice between Alaska and Siberia has been analyzed (orbit 348). This orbit traversed the seasonal ice layer, which appears to be smooth or new ice based on the altitude time-history. The over-ice σ° versus angle dependence was similar to the over-land results except that the one-degree value was at least 4 dB lower. The actual sampled value was near the quantization noise level and the observed value is considered to be an upper bound.

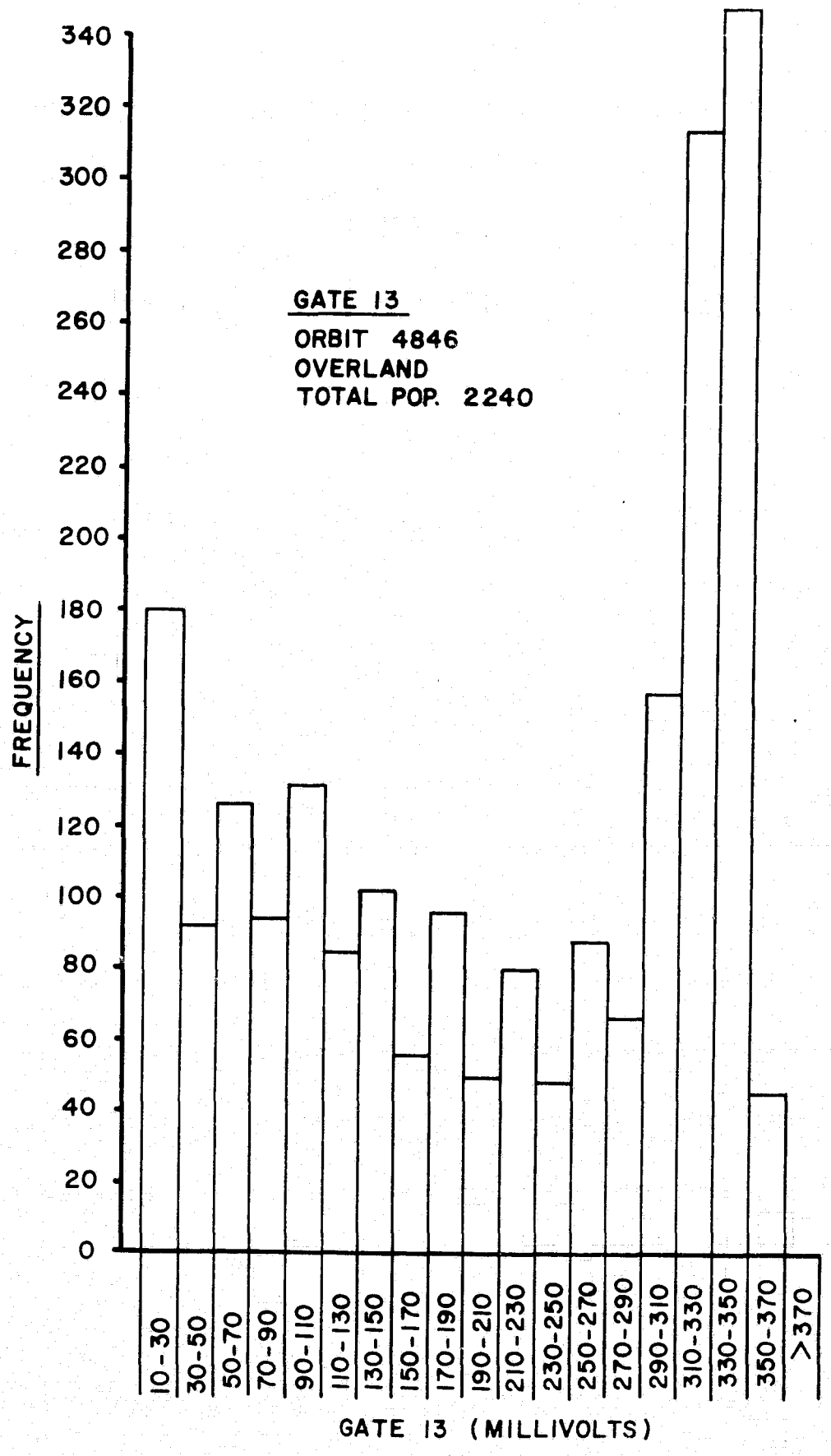

Figure 47. Over-land histogram showing saturation effect.

Figure 9 also shows σ° values for an over-ocean case. This is the greatest angular dependency observed for ocean backscatter thus far.

Figure 11 contained absolute σ° values for the geographic regions examined. The upper and lower bars show the maximum and minimum σ° values obtained from the 10/sec AGC data. The circles indicate the average (power) σ° value - not the average of the dB values. The abcissa shows the geographic region, data, and orbit number. All passes over the same region were separated by only a few km (1164-4846 by 4 km, 3268-4846 by 12 km, and 2236-2762 by 4 km). Note that the average σ° value over land is in the neighborhood of 20 dB, with the exception of data from orbit 4846. This pass shows a 7 - 9 dB change over the other Florida σ° data. Figure 11 also shows the over-ocean σ° values for these Florida passes, as a check on data quality. The significant wave heights, as estimated from waveform data, for orbits 1164, 3268, and 4846 are ~.5, 1.0, and 3 meters, respectively. These σ° and wave height values are in good agreement with ocean backscatter values observed for numerous passes. Surface moisture effects are suggested by the Florida data; as the data base expands, these parameters will also be cataloged and analyzed. The small scatter in the Ontario data is mainly due to the small sample size (2 frames); this small scatter is characterictic of the ocean data. Figures 39 and 40 showed histograms of the fluctuation characteristics for ocean and land backscatter. The two distributions are similar. Figure 47 shows a histogram of one of the sampling gates which has substantial saturation.

The previous discussions have shown that in general two parameters are available from a backscatter measurement; the absolute magnitude or σ° at nadir, and the change in σ° with angle. Using rough surface scatter theory as a guideline, the backscatter coefficient is given by [3]

$$\sigma^\circ = \frac{|R(0)|^2}{4S_m^2 \cos^4\theta} e^{-\frac{.25}{S_m^2}\tan^2\theta}$$

where R(0) is the Fresnel reflection coefficient

S_m is the mean-square slope, and

θ is the off-normal angle.

Defining the change in σ° over some angular expanse θ as $\Delta\sigma^\circ$

$$\Delta\sigma^\circ = \frac{\sigma^\circ(\theta)}{\sigma^\circ(0)} = \cos^4\theta \; e^{-\frac{.25}{S_m^2}\tan^2\theta} \simeq e^{-\frac{.25}{S_m^2}\theta^2}$$

or the mean square slope is

$$S_m^2 \simeq \frac{.25\theta^2}{-\ell n \Delta\sigma^\circ}$$

The on-nadir value of σ° is

$$\sigma_o = 10 \log|R(0)|^2 + 10 \log(4 S_m^2 \cos^4\theta)^{-1}$$

or

$$|R(0)|^2_{dB} = \sigma_o(dB) - 10 \log\left(\frac{-\ell n \Delta\sigma^\circ}{\theta^2}\right)$$

for small angles off nadir. Table II gives computed values based on the previously quoted experimental results.

TABLE II

Computed Surface Parameters

Target	Meas. σ° dB	$\Delta\sigma^\circ$ dB	s_m^2	$10 \log \frac{-\ell n \Delta\sigma^\circ}{\theta^2}$ dB	$\lvert R(0) \rvert^2$ dB
Ocean	~ 24	1	3.3×10^{-4}	28.1	-4.1
Land	~ 22	~ 10	3.3×10^{-5}	38.78	-16.8

The last entry in Table II shows the value of Fresnel reflection coefficient inferred by the measured value of σ°. The land value is in very good agreement with data given in [9]; over-ocean values have not yet been located, however, the result appears reasonable. Reference 9 also shows measured data which indicates an ~ 7 dB change in σ° after rainfall, the same magnitude noted in the Florida data. These preliminary findings indicate that surface moisture content and dielectric properties may well be obtainable from the GEOS-3 data; also, the Fresnel reflection coefficient is the parameter of interest rather than σ_o, per se.

REFERENCES

1. Kaula, W. M.: "The terrestrial environment: Solid earth and ocean physics," Rep. on a study at Williamstown, Mass., NASA CR-1579, August, 1969.

2. Vincint, S.; and Marsh, J. G.: "Global detailed gravimetric geoid," NASA Goddard Space Flight Center, Rep. X 592-73-266, September, 1973.

3. Brown, G. S. (Editor): "Skylab S-193 Altimeter Experiment Analyses and Results," NASA CR-2763, Applied Science Associates, Inc., Apex, N. C., February, 1977.

4. Meyer, D. P.: and Mayer, H. A.: Radar Target Detection, Academic Press, New York, 1973.

5. Huang, N. E.: "Gulf Stream Model," Final Report, NASA Contract NAS6-2307, Applied Science Associates, Inc., Apex, N. C., September, 1974.

6. Hofmeister, E. L.; et. al.: "Data Users Handbook and Design Error Analysis, GEOS-C Radar Altimeter," NASA Contract NAS6-2619 Rep., May, 1976.

7. Miller, L. S.: "GEOS-3 investigation, Third quarterly report on NAS6-2621," Applied Science Associates, Inc., Apex, N. C., January, 1976.

8. Miller, L. S.; Brown, G. S.; and Smith, A. G.: "Engineering studies related to the Skylab programs," Final Rep. (Task D), NASA Contract NAS6-2307, Applied Science Associates, Inc., Apex, N. C., February 1974.

9. Schwartz, M.; and Shaw, L.: Signal Processing, Discrete Spectral Analysis, Detection and Estimation, McGraw Hill, N. Y., 1975.

10. Hofmeister, E. L.: "Analysis and Measurement of the Performance of a Signal Tracking Loop for a Satellite Radar Altimeter When Excited by a Ramdom Process," Ph.D. Thesis, Syracuse University, Syracuse, New York, December, 1973.

11. Hayne, G. S.; Miller, L. S.; and Brown, G. S.: "Altimeter Waveform Software Design," Final Report (Task 3.1), NASA Contract NAS6-2520, Applied Science Associates, Inc., Apex, N. C., April, 1975.

12. McGoogan, J. T.; Miller, L. S.; Brown, G. S.; and Hayne, G. S.: "The S-193 radar altimeter experiment," Proc IEEE, Vol. 62, No. 6, June, 1974.

13. Brown, G. S.; and Curry, W. J.: "The Estimation of Pointing Angle and σ° from GEOS-3 Radar Altimeter Measurements," Final Report (Tasks 3.8 & 3.13), NASA Contract NAS6-2520, Applied Science Associates, Inc., Apex, N. C., August, 1976.

APPENDIX A

GEOIDAL ANOMALY CALCULATION

By Clayton B. Jackson

In this appendix, the relationship between altimetric (or true geometric) height measurements and orthometric height data (the usual map data format) is discussed. Given orthometric or spirit-level height data either geoid or gravity anomaly can be recovered through use of the altimeter measurement data. Assume that it is desired to measure unique gravitational changes from a known geoid reference.

In the system shown below H is the sea surface height of A_2 as measured from A, by leveling; H' is the altimeter height also referenced to sea surface height

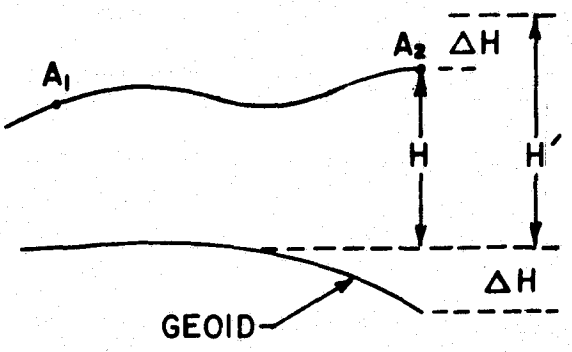

The difference between the H and H' is the error in the leveling height H due to a geoid change ΔH, i.e.

$$H + \Delta H = H' \qquad \text{or} \qquad \Delta H = H' - H$$

The gravitational change is described as follows:

$$\Delta\bar{g} = \Delta\bar{F} + \Delta\bar{C}$$

where

$\Delta\bar{F}$ = gravitational force change

$\Delta\bar{C}$ = centripetal force change

thus

$$\Delta\bar{g} = \bar{F}_R - \bar{F}_{R-\Delta H} + \bar{C}_R - \bar{C}_{R-\Delta H}$$

R = geoid radius .

The magnitude of $\Delta\bar{g}$ is

$$|\Delta g| = -6M\left[\frac{1}{R^2} - \frac{1}{(R-\Delta H)^2}\right] + \omega^2\left[R-(R-\Delta H)\right]\sin^2\phi$$

$$= -6M\left[\frac{1}{R^2} - \frac{1}{(R-\Delta H)^2}\right] + \omega^2\Delta H \sin^2\phi \quad .$$

Assume, for example that point A is located at Cape Canaveral and point B at Fort Meyers, Florida (orbit 4568). Using the above equation with

$$R_A = R_{\text{ref. geoid}} + \text{SSHITE at A latitude } \phi_A$$

$$R_B = R_{\text{ref. geoid}} + \text{SSHITE at B latitude } \phi \quad .$$

Then

$$|\Delta g| = -\frac{6M}{R_B}\left[\frac{R_B^2}{R_A^2} - \left(1 - \frac{\Delta H}{R_B}\right)^2\right] + \omega^2\Delta H \sin^2\phi_B$$

$$\simeq g_B\left[\frac{2\Delta H}{R_B}\right] + g_B\left[\frac{R_B^2}{R_A^2} - 1\right] + \omega^2 H\Delta \sin\phi_B$$

where

$g_B \frac{2\Delta H}{R_B}$ is the local gravitational anomaly at B

$g_B\left[\frac{R_B^2}{R_A^2} - 1\right]$ is the anomaly due to the earth's flattening.

Noting that ΔH is the sea surface height difference between points A and B; R_A and R_B can be determined using the reference geoid

$$R_{ref.} = G\left[1 - 3.3248\times10^{-3}\ \sin^2\phi - 2.801\times10^{-5}\ \sin^4\phi\right]$$

at the latitude ϕ. (This equation will be developed at the end of this appendix.) Finally g_B is calculated using $g_B^2 = -\frac{6M}{R_B}$.

In orbit 4568

$$\Delta H = 5 \text{ meters}$$

$$\phi_A = 28.50$$

$$\phi_B = 26.30$$

$$G = 6.67\times10^{-8}$$

$$M = 5.99\times10^{27} \text{ gm}$$

$$\omega^2 = 5.31\times10^{-9}$$

$$R_A = 6{,}373{,}307.5 \text{ m.}$$

$$R_B = 6{,}373{,}975.2 \text{ m.}$$

$$|\Delta g| \simeq -1.573 \text{ mgals} - 0.2053 \text{ gals}$$

The value - 1.573 mgals is the value of Δg at point B, due to a local mass anomaly.

Development of last equation:

The equation for a spheroid with semi major axis a_ℓ and eccentricity ℓ^2 is [1]

$$r \simeq a_\ell\left(1 - \frac{\ell^2}{2}\sin^2\beta + \frac{\ell^4}{2}\sin^2\beta - \frac{5}{}\ \ell^4\ \sin^4\beta\right)$$

where β is the Latitude in degrees.

Since the GEOS-3 reference spheroid has

$$a_\ell = 6{,}378{,}145 \text{ meters}$$

and the polar flattening α is related to ℓ through

$$\ell^2 = 2\alpha - \alpha^2$$

for

$$\alpha = 3.3528 \times 10^{-3}$$

$$\ell^2 = 6.69441 \times 10^{-3} \quad .$$

The distance from a point on the spheroid and the center is

$$r = 6{,}378{,}145 \left[1 - \frac{6.6944 \times 10^{-3}}{2} \sin^2\beta + \frac{(6.69441 \times 10^{-3})^2}{2} \sin^2\beta \right.$$

$$\left. - \frac{5}{8} (6.69441 \quad 10^{-3})^2 \sin^4\beta \right]$$

$$= 6{,}378{,}145 \left[1 - 3.3248 \times 10^{-3} \sin^2\beta - 2.801 \times 10^{-5} \sin^4\beta \right] \text{ meters}$$

REFERENCE

1. Zakatov, P. S.: "A Course in Higher Geodesy", Israel Program For Scientific Translations LTD, Equ. 5.17, pp. 16, Jerusalem, 1962.

APPENDIX B

WIENER FILTER DETAILS

This appendix gives details on the Wiener filter used in this report. Referring to equation numbers from [3] the GEOS-3 coefficient may be found as follows: Using the equation just below (10) for a = .16002, S_o = 71.66 and β_n = 6.5 gives

$$h_c(t) = \left(1 + \frac{1.17697|t|}{\sqrt{\sigma_h}}\right) \exp - \frac{1.17697|t|}{\sqrt{\sigma_h}}$$

where t is in seconds and σ_h in meters. For the GEOS-3 altitude rate of 32 values per 3.277 seconds (or 9.7656 values per second) the discrete time equation is

$$h(KT) = \left(1 + \frac{.1205}{\sqrt{\sigma_h}} K\right) \exp - \frac{.1205}{\sqrt{\sigma_h}} KT$$

in which K is the altitude number (i.e. $\pm$ 1,2,3...N). These weights should be reflected about K = 0, and normalized to preserve d-c value of the process. Attached is a sample listing (σ_h = .6m) and graph of the convolution weights for the altitude data. These weights estimate the midpoint value over 81 input values.

The above coefficients are for a geodetic region similar to the Puerto Rican trench. Figures 20 and 21 showed several power spectral densities on a comparative basis. Figure B-1 shows the filter weighting coefficients for the continuous case. Table B-1 lists GEOS-3 data-rate coefficients.

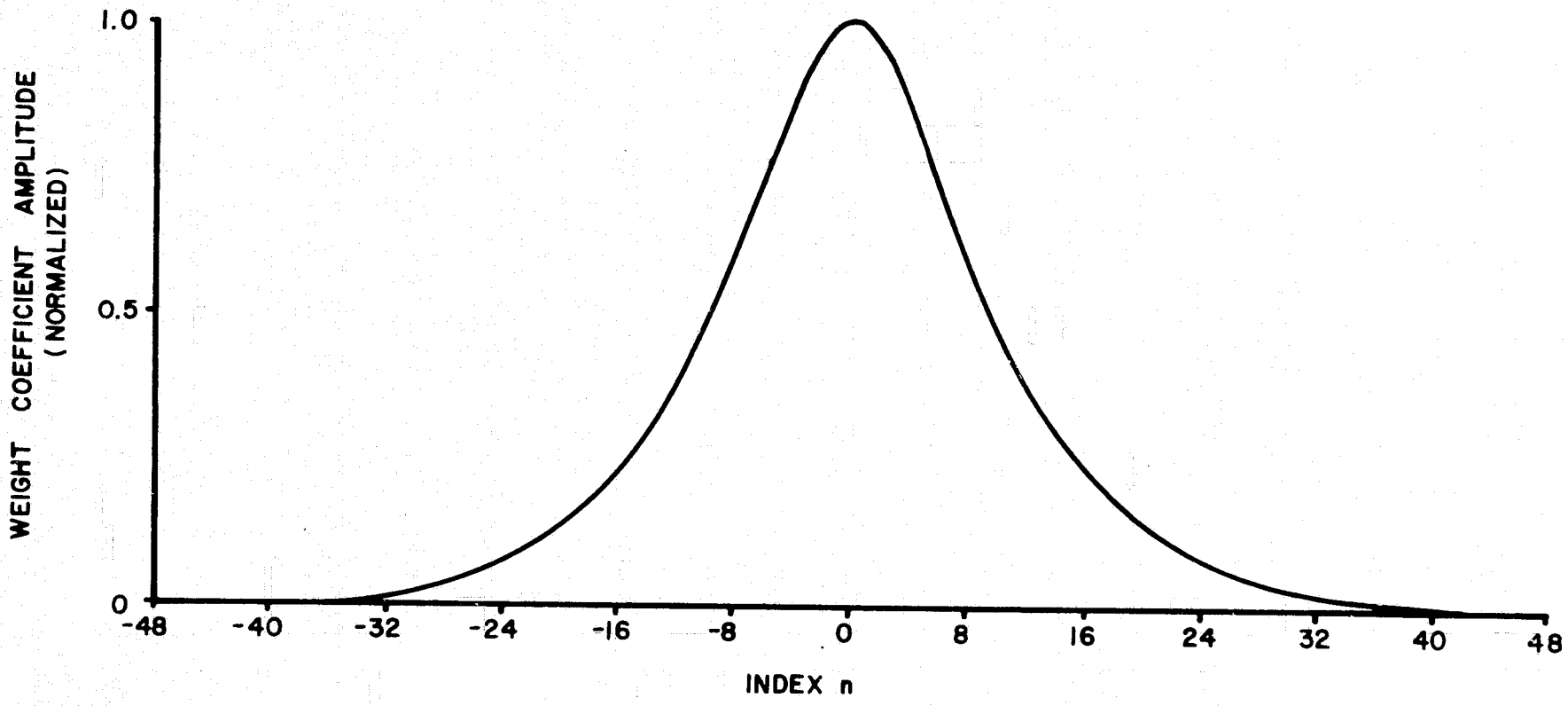
WEIGHT COEFFICIENT AMPLITUDE
(NORMALIZED)
1.0
0.5
0
-48
-40
-32
-24
-16
-8
0
8
16
24
32
40
48
INDEX n

Figure B-1

TABLE B-1

GEOS-3 Wiener filter weights for ~10/sec altitude data and rms tracking jitter = 60 cm.

We(00)	0.0006	We(41)	0.0388
We(01)	0.0006	We(42)	0.0377
We(02)	0.0007	We(43)	0.0361
We(03)	0.0008	We(44)	0.0342
We(04)	0.0010	We(45)	0.0320
We(05)	0.0011	We(46)	0.0298
We(06)	0.0012	We(47)	0.0276
We(07)	0.0014	We(48)	0.0254
We(08)	0.0016	We(49)	0.0232
We(09)	0.0018	We(50)	0.0211
We(10)	0.0021	We(51)	0.0192
We(11)	0.0024	We(52)	0.0174
We(12)	0.0027	We(53)	0.0157
We(13)	0.0031	We(54)	0.0141
We(14)	0.0035	We(55)	0.0127
We(15)	0.0039	We(56)	0.0113
We(16)	0.0044	We(57)	0.0101
We(17)	0.0050	We(58)	0.0090
We(18)	0.0057	We(59)	0.0081
We(19)	0.0064	We(60)	0.0072
We(20)	0.0072	We(61)	0.0064
We(21)	0.0081	We(62)	0.0057
We(22)	0.0090	We(63)	0.0050
We(23)	0.0101	We(64)	0.0044
We(24)	0.0113	We(65)	0.0039
We(25)	0.0127	We(66)	0.0035
We(26)	0.0141	We(67)	0.0031
We(27)	0.0157	We(68)	0.0027
We(28)	0.0174	We(69)	0.0024
We(29)	0.0192	We(70)	0.0021
We(30)	0.0211	We(71)	0.0018
We(31)	0.0232	We(72)	0.0016
We(32)	0.0254	We(73)	0.0014
We(33)	0.0276	We(74)	0.0012
We(34)	0.0298	We(75)	0.0011
We(35)	0.0320	We(76)	0.0010
We(36)	0.0342	We(77)	0.0008
We(37)	0.0361	We(78)	0.0007
We(38)	0.0377	We(79)	0.0006
We(39)	0.0388	We(80)	0.0006
We(40)	0.0393		